CFD Analysis of Air Flow Interactions in Vehicle Platoons

A thesis submitted in fulfilment of the requirements for the degree of
Master of Engineering

Gokul Krishnan Rajamani
B.Eng.

School of Aerospace, Mechanical and Manufacturing Engineering
RMIT University
August 2006

Declaration

I certify that except where due acknowledgement has been made, the work is that of the author alone; the work has not been submitted previously, in whole or in part, to qualify for any other academic award; the content of this thesis is the result of work which has been carried out since the official commencement date of the approved research program; and, any editorial work, paid or unpaid, carried out by a third part is acknowledged.

Gokul Krishnan Rajamani
Date:

Acknowledgements

Sincere thanks to Associate Professor Simon Watkins for his time and support dedicated during my entire research program. Sincere thanks to Professor Jiyuan Tu for his guidance and support on CFD throughout this research program.

Thanks to Gioacchino Vino for his initial support on experimental analysis and comments on CFD validation. Thanks to Mr. Zhao Feng Tian for his comments on CFD analysis.

Sincere thanks to Professor Bill Applebee, of Victorian Partnership for Advanced Computing (VPAC) for funding this e-research program.

Mr. Satya Prasad Mavuri is thanked for his valuable guidance in both the experimental and computational analysis during these two years of research work.

Sincere thanks to Mr. Riccardo M. Pagliarella for rendering all of his support in performing experimental analysis for the current research study.

Thanks to Jennifer Morgan for her time on proof reading the thesis. Thanks to Mr. Gill Atkins for his support in model manufacturing at the workshop.

Special thanks to my parents for their continuous encouragement and support throughout my life.

Abstract

The increasing use of Intelligent Transport System (ITS) can enable very close vehicle spacings which generally results in a net drag reduction for the resulting convoys. The majority of vehicle development has, to date, been for vehicles in isolation, thus the study of interaction effects is becoming increasingly important.

The main objective of this research is to investigate the use of Computational Fluid Dynamics (CFD) for understanding convoy aerodynamics and to further the understanding of airflow interaction between vehicles via CFD.

In this study, time-averaged characteristics of a simplified, generic passenger vehicle, called the Ahmed car model, after Ahmed et.al (1984) is investigated computationally using the available commercial CFD code, Fluent version 6.1.22. Three different platoon combinations were analysed for the current study which includes a two, three and six model platoons for various rear end configurations of the Ahmed model geometry.

Experiments were conducted in RMIT University Industrial Wind Tunnel for analysing the effects of drafting on drag coefficients using two different scales of Ahmed car models. This is an extension to the previous study performed on two 100% scales of Ahmed models (Vino and Watkins, 2004) and the results for both the current and previous experiments were compared using CFD. The CFD proved to be a useful technique since its results compared reasonably well for both the current and the previous experiments on drafting, using Ahmed models of identical (30˚) rear slant configurations. However, near critical rear slant angles (~30˚) for isolated vehicles some discrepancies were noted.

The reasonable validation of experimental results enabled the study to be extended further computationally using CFD, to analyse the effects of inter-vehicle spacing on a platoon of 3 and 6 models for various rear end configurations (between

0˚ and 40˚), in an attempt to provide useful information on vehicle-wake interaction for the Future Generation Intelligent Transport System (FGITS).

Critical gaps were identified via CFD for the case of a two, three and six model platoons and the simulations clearly exposed the reasons for these critical gaps. At extremely close proximity, the models experienced more pressure recovery at their rear vertical base, which reduced the drag coefficient. Surprisingly, at some of the close vehicle spacings, the drag coefficients reached values that were higher than that of a vehicle in isolation. This was found due to the high momentum flow impingement to the fore body of the model and was similar to results found in physical experiments.

Thus the current CFD analysis revealed that rear slant angle of the model and the inter-vehicle spacing greatly influences the wake structures and ultimately the vehicles aerodynamic drag coefficients in platoons.

Even though the current CFD model (Realizable k-ε turbulence model) predicted the basic flow structures such as the C-pillar vortices from the rear slant and 2D horse shoe vortices in the model's vertical rear base, the separation bubble on the rear slant that supplies energy to the strong C-pillar vortices was not replicated accurately, which is evidenced from the flow structure analysis. Hence it is recommended for further work, that the study should be extended using the Reynold's stress models or the Large Eddy Simulation (LES) turbulence models for flow structure observation and analysing vortex interactions between the models.

TABLE OF CONTENTS

LIST OF FIGURES

LIST OF TABLES

Nomenclature

The following are the list of symbols that are commonly used in this thesis report.

ρ Density

t Time

T Sample period

u, v, w Mean local components of velocity

V Free stream velocity

A Frontal area

C_D Coefficient of Drag

C_P Static Pressure Coefficient

L Model length

x Distance between leading and trailing models

Re Reynolds number

S_m Mass added to the continuous phase from the dispersed second phase

p Static pressure

Γ Stress tensor

$\vec{F}$ Gravitational body force and external body forces

μ Molecular viscosity

μ_t Turbulent (or eddy) viscosity

I Unit tensor

k turbulence kinetic energy

ε Dissipation rate

G_b Generation of turbulence kinetic energy due to buoyancy

G_k Generation of turbulence kinetic energy due to the mean velocity gradients

$C_{1\varepsilon}$, $C_{2\varepsilon}$, & $C_{3\varepsilon}$ Constants

C_μ Constant

$\sigma_{k,}$ Turbulent Prandtl numbers for k

σ_ε Turbulent Prandtl numbers for ε

S_k & S_ε User-defined source terms

$\overline{u^2}$ Normal stress

$\overline{\Omega_{ij}}$ Mean rate-of-rotation

ω_k Angular velocity

A_0 & A_s Model constants

ϕ Primary variable

α Under-relaxation factor

α Rear slant angle of Ahmed body

$\nabla\phi$ Gradient in the upstream cell

$\Delta\vec{s}$ Displacement vector from the upstream cell centroid to the face centroid

$\tilde{\phi}_f$ Face value

1 Introduction

1.1 Research Background

The aerodynamic characteristics of passenger cars have been a fruitful area of research for several decades, and continue to this day. However, it is well appreciated that there remains much to learn in this area, and that further research is required to understand the complex aerodynamic interactions between vehicles.

As the human population continues to grow in number, the need for more practical and efficient methods of transportation becomes more vital. In the past, simply constructing more roads and highways to cope with the growing number of vehicles has solved this problem. Obviously this trend cannot continue indefinitely, so a method that is currently being considered by several organizations, one of which is the California Partners for Advanced Transit and Highways (PATH) group, is the Automated Highway System (AHS) (Hall, 1997).

The primary aim of the Future Generation Intelligent Transport System (FGITS) (Pagliarella, 2005) is to increase the highway throughput, which is accomplished by platooning vehicles with reduced inter-vehicle spacing. The aerodynamic efficiencies of the individual vehicles are thus expected to improve since their drag coefficients are expected to reduce with close vehicle spacing. Thus, the overall fuel efficiencies of the vehicles in platoon are expected to improve with reduced emission levels and added safety. In the Automated Highway System (AHS), road vehicles driving on highways would assume convoy arrangements, thus experiencing the drag benefits of being closely coupled at high speeds. Vehicles would be equipped with Intelligent Transport Systems (ITS) such as distance sensors, Adaptive Braking System (ABS), Global Positioning Systems (GPS) and other ITS systems which would enable the vehicles to travel ‘safely’ close together (e.g. less than one car length), closely resembling a convoy of train carriages. However, before such type systems can be considered for implementation, a detailed understanding of how these vehicles would behave (i.e. aerodynamically) when in close proximity to

one another is required. As such, PATH has conducted significant aerodynamic research associated with various forms of vehicle-to-vehicle interference, which will be discussed in later sections.

The overall aim of the current research is to investigate the effects of a more representative flow environment on the body forces and flow fields of passenger cars in convoys using CFD with experimental validation.

1.2 Passenger Vehicle Aerodynamics

1.2.1 Overview

For much of the 20th century, vehicle requirements such as aesthetics and feasibility constrained vehicle aerodynamicists in their aims of reducing the drag of passenger vehicles. It was not until the 1973 when a group of oil exporting countries significantly increased the price of crude oil, and at the same time cutting production, which put greater emphasis on the reduction in drag. Road vehicle aerodynamic design became extremely important to motor companies as designing cars with lower drag and therefore lower fuel consumption became a vital selling point. As a result of this new aerodynamic era in the motor industry, it soon became apparent that other advantages such as improved stability and performance could be obtained through aerodynamic development, Hucho (1998).

Modern passenger vehicles are generally laid out according to the front engine three-box layout, which, on its own has a great influence on the resulting external shape. Barnard (1998) underlines the undesirable flow features that occur with this shape. Firstly, the flow may separate at the top of the radiator grill and reattach at some point on the engine cover. At the lowest part of the windscreen the flow may undergo separation again and reattach some way up the wind screen. It can again separate at the top of the wind screen and reattach some way downstream of the roof leading edge. A final separation occurs at the end of the roofline and may reattach to

the boot lid depending on factors such as backlight angle and boot length. If reattachment occurs, separation will also occur at the rear of the boot lid.

As shown in figure 1, many separation and reattachment points exist on the vehicle body, indicating a high drag configuration. It is now clear why aerodynamics plays such a large role in the design of modern automobiles, as it is extremely important that the adverse effects of these drag-inducing geometric factors are avoided or at least reduced.

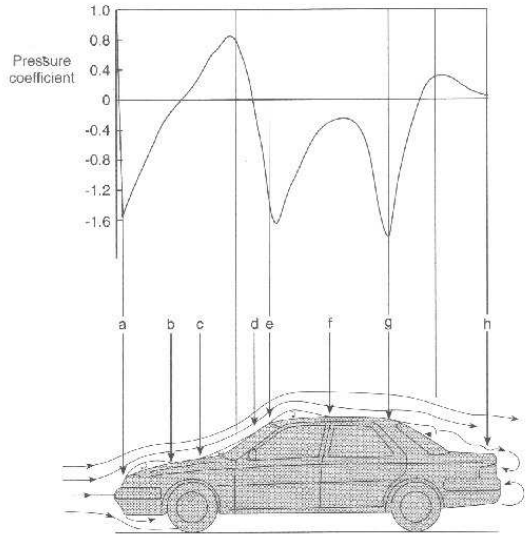

Figure 1. *Flow features of a notchback passenger vehicle, after Barnard (1998)*

1.2.2 Sources of Drag

Drag is the primary aerodynamic dictator of performance parameters such as straight-line speed and fuel economy, with the magnitude of influence increasing with vehicle speed. The aerodynamic drag of a body increases with the square of the speed ($F_D = ½ \rho V^2 A$). Hucho (1998) states that the aerodynamic drag of medium-sized cars typically accounts for about 75-80% of the total resistance to motion at 100 Km/h and therefore contributes a significant percentage on the vehicles fuel economy.

1.2.2.1 Surface Friction Drag

On the surface of a road vehicle the air is stationary, but a shear stress is exerted in a process that is commonly referred to as surface friction drag. A detailed

description on the physical mechanisms associated with surface friction drag was provided by Schlicting (1960). He observed the roof of the car, since the flow structure resembles more similar to that when observed over a flat plate. From his experiments, he found that the relative velocity of air particles increased significantly as a function of distance from the surface and finally reached its free stream velocity (Boundary layer theory). He concluded that in-spite of a thin boundary layer past the roof of a car; significant shearing velocity existed in the boundary layer.

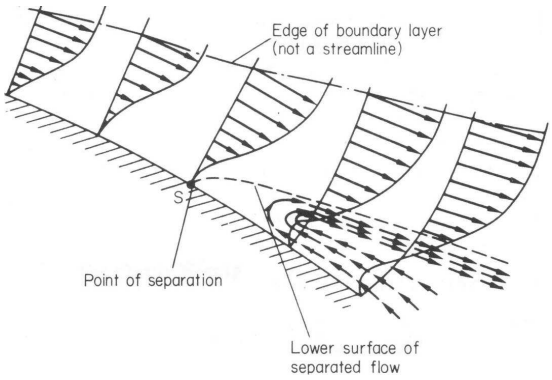

Figure 2. *Boundary layer development and separation, after Houghton and Carpenter (1993)*

It is well known that in a boundary layer, there are three different phases, the laminar region, the transition region and the turbulent region. As known, in the laminar region, the thickness of the boundary layer is small and increases gradually from zero at the start to a significant thickness till it reaches the transition region. In the transition region the mixing of particles further increases the thickness of the boundary layer. Thus the transition region gets transferred to a turbulent boundary layer where the shear stresses are higher and the thickness grows at a higher rate. These shear stresses, which are produced on the surfaces by the relative velocity between the air and the vehicle in the boundary layer, are considered to be the major source for surface friction drag.

1.2.2.2 Pressure Drag

In general passenger vehicles are characterized by attached flow in the front and the mid sections. When the flow reaches the rear ends or backlights of a vehicle,

they separate leading to the formation of large dead water region called the wake region. This separation results in poor pressure recovery results (i.e. pressure difference between the front and the rear ends of a vehicle), which inturn exerts a net force opposite to the direction of motion, called the pressure drag (Hucho, 1998). This pressure drag is the major source of drag coefficient for passenger car geometries. Thus one of the aims of aerodynamic development of a road vehicle is to reduce the drag coefficients of vehicles by improving its pressure recovery at wake which in turn can be achieved by reducing the vehicle's wake region (Hucho, 1998).

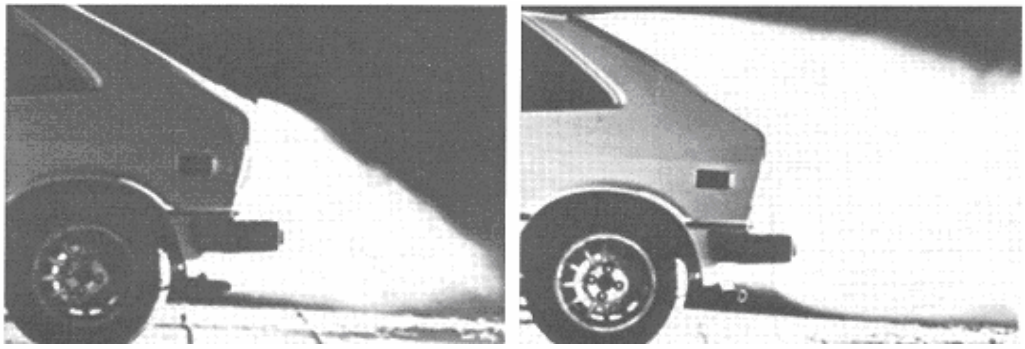

Figure 3. *Wake profiles of fastback and squareback vehicles, after W.H.Hucho (1998)*

The pressure drag is distinct to the shape of the vehicle. The figure 3 shows a typical separated wake region of a passenger vehicle. Two different wake structures are observed for both the models. For, the model on the right hand side of figure 3, a large wake region is observed as the separation is introduced artificially by a deflector vane at the end of the roof line. For, the model on the left hand side of figure 3, the absence of the deflector vane has lead to the formation of C-pillar vortices. These C-pillar vortices, created a down wash which pulled the air over the slanted surface and delayed the separation till the vertical base; thus reducing the size of the wake region. It is also important to note that a smaller wake does not always result in lower drag, in particular for complex three dimensional flows such as wakes of passenger cars. This is due to the third main drag mechanism called the vortex induced drag. Similar studies were carried on by Sims-Williams (2001) using Ahmed car model of 30˚ rear slant, to observe its criticality which is discussed later in this chapter.

1.2.2.3 Vortex-Induced Drag

As seen before, passenger vehicles are considered as bluff bodies (Hucho, 1998) because of their nature of generating high levels of pressure drag. The separation that occurs at the blunt rear ends of a passenger vehicle is often accompanied by a set of longitudinal steam-wise vortices, called the C-pillar vortices. These vortices are highly three dimensional in nature and are rich in kinetic energy. They create down wash by pulling the surrounding air to the model's rear slant (as seen in the previous section) there by reducing the size of the model's wake region. The strength to these vortices is mainly supplied by the flow separating from the sides of the vehicle's rear slant. Therefore, the rear slant angle of a vehicle plays a vital part in determining the strength of these C-pillar vortices. Additionally, the source of drag that is created by these vortices is also known as the lift-induced drag.

The influences of rear slant angle on the strength of the C-pillar vortices are discussed in the later sections of this chapter.

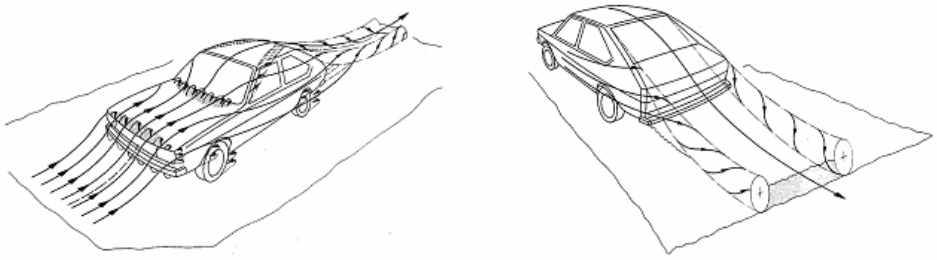

Figure 4. *Vortex Generation around passenger car, after W.H.Hucho (1998)*

1.3 Flow Structures Around Passenger Vehicles

The use of basic vehicle shapes has proved to be extremely useful for predicting the fundamental flow physics associated with complex vehicle geometries and this phenomenon was investigated by Le Good and Garry (2004). Of all the basic shapes of models that were investigated before, one of the popular model was the Ahmed car model; after, Ahmed et.al. (1984). The Ahmed model had a rounded front end, sufficiently long mid section or the body to reduce the front end effects on the

wake flow structures. The rear end of the Ahmed model can be varied by changing its rear slant angle (α) between 0˚ and 40˚, which can generate sufficiently strong C-pillar vortices when the rear slant angle is at 30˚.

1.3.1 Time-Averaged Flows

The influence of rear slant angles on drag coefficients was initially studied by Morel (1978). Morel found from his studies, that the rear slant angle of a simplified passenger vehicle significantly influences the drag coefficients of the vehicle. He observed from his experiments (using a simplified model with variable rear end geometry) that, when the rear slant angle was increased from 0˚ to 60˚, it was accompanied with a corresponding increase of drag coefficients. Beyond 60˚ the model experienced a significant increase of drag coefficients which almost doubled the previous value. Also, after this critical angle, the drag coefficients reduced sharply and approached drag values of 0˚ rear slant configurations.

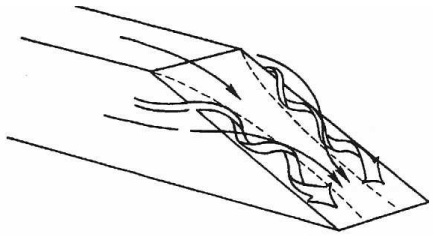

Figure 5. *Proposed 'C'-pillar flow pattern, after Morel (1978)*

This phenomenon, when analysed in detail revealed the presence of two distinct flow regimes. The first corresponding to slant angles that are lower than the critical angle, which can be compared to models with small or no slanted rear ends, since the wake is dominated by a large closed separation region behind the base. The later flow regime, was a combination of the first and a set of highly 3-dimensional steam-wise vortices (see figure 5) from the separations along the slant sides.

After Morel (1978), Ahmed et.al. (1984) continued to investigate the influences of rear slant angle on drag coefficients of bluff bodies. In his experiments, he used a simplified vehicle shape more similar to that used by Morel (1978), with

minor geometrical changes. Ahmed et.al. used several techniques to understand the time averaged aerodynamic properties of fast back vehicle geometry.

From their experiments, the force and surface pressure measurements revealed the percentage of pressure drag for the front, body (middle section) and the rear part of the model. It was that the front part contributed the least amount of pressure drag, while the rear slant contributed the highest amount of pressure drag. They found that the variation of rear slant angle between 0˚ and 40˚ showed considerable variation in drag coefficients. The effects of rear slant angles on drag coefficients after, Ahmed et.al (1984) are shown in figure 6.

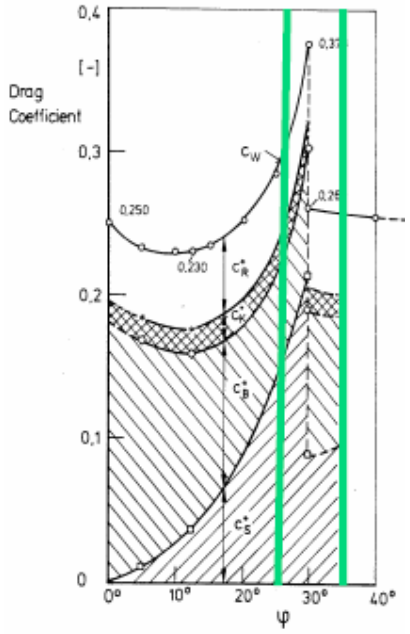

Figure 6. *Characteristic drag coefficients for the Ahmed body for various slant angles, after Ahmed et.al (1984)*

From figure 6, it can be seen that the drag value reached a maximum when the rear slant angle was 30˚. Also, it was observed that as the base slant was varied slightly (i.e. beyond 30˚) the drag coefficients dropped significantly and remained steady thereafter. Hence, flow visualization studies were performed by Ahmed et.al in order to analyse these influences of rear slant angle on drag coefficient (see figure 8).

It was observed that for base slant of ≤ 30˚, the shear layers that begin from the rear slant rolled up into strong three dimensional C-pillar vortices. Also, these

shear layers after separating at the leading edge of the rear slant, reattached at the lower end of the rear slant, before reaching the base. Thus, the flow created a separation bubble between the separation and reattachment point on the rear slant surface. The flow on reaching the bottom edge of the rear slant gets separated from the top and bottom edges into two separate recirculatory flow regions A and B, one above the other and in opposing directions, called the quasi static two dimensional vortices as shown in figure 7.

Ahmed et.al. (1984) proposed the time-averaged flow structures, based on the surface flow patterns shown in figure 7. It was found that the longitudinal C-pillar vortices and the upper two dimensional vortex A was highly influenced by the rear slant angle; the lower vortex B depends on the under body flow and the ground clearance of the model.

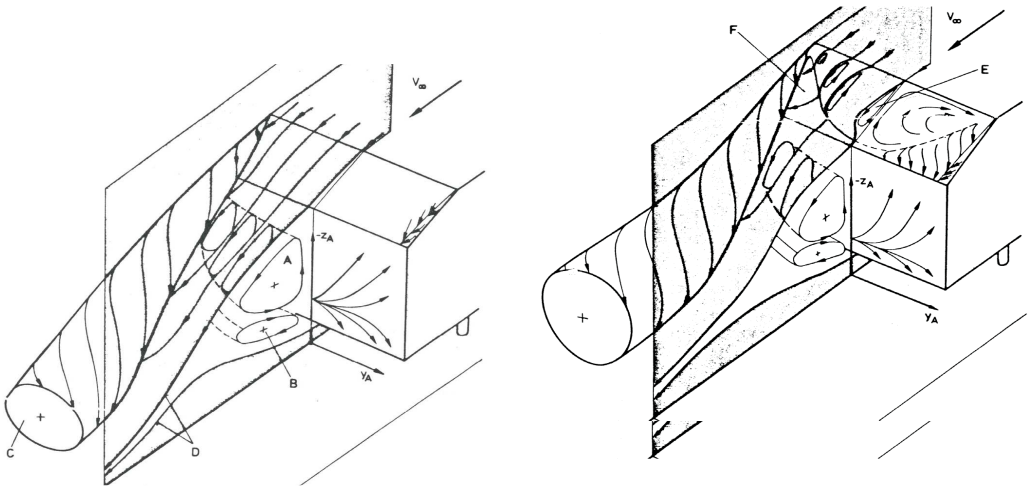

Figure 7. *High Drag and Low drag regimes for 30˚ Slant fast back proposed by Ahmed et.al. (1984)*

At 30˚ rear slant angle, the separation bubble E was observed to reach its maximum size, thus forming the horseshoe vortex on the slanted surface. This in turn increased the strength of the C-pilar vortices and promoted the flow to reattach before separating at the base into two quasi-static two dimensional vortices. Additionally, the separation bubble which was a region of flow reversals reduced the pressure on the base slant and ultimately increased the pressure drag of the model.

Based on the skin friction patterns performed for 12.5˚, 25˚ and 30˚ configuration of Ahmed model after Ahmed et.al. (1984), it can be seen (see figure 8) that, the flow separation at the leading edge of the slanted surface exists even for angles lower than 30˚. The patterns clearly exhibit the presence of C-pillar vortices and the horse shoe vortex on the slant surface. For rear slant angles greater than 30˚, the flow that separated at the roof backlight junction would no longer reattach at the base of the backlight (i.e. flow region E) and functions as part of flow region B (see figure 7). Thus, the separation bubble on the rear slant is broken and the C-pillar vortices lose their strength because of insufficient supply of flow from the sides of the model, therefore resulted in improved pressure recovery and reduced the drag coefficients.

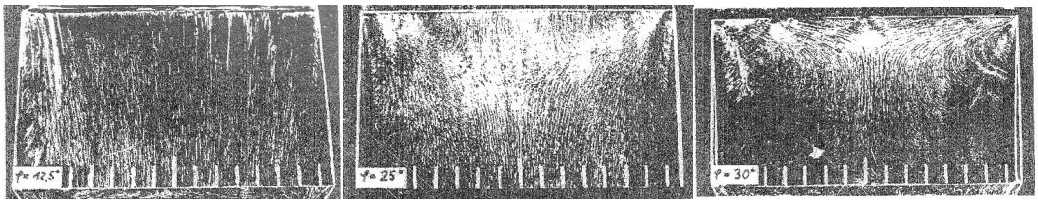

Figure 8. *Skin friction patterns for different rear slant angles, after Ahmed et.al. (1984)*

It was conjectured that the change in flow structure is analogous to the vortex breakdown phenomenon observed over delta wings; in that the slant angle becomes so large that the stream wise vortices become unstable, eventually breaking down. As a result, the downwash generated by these vortices is no longer present, and so the central separated region is not drawn as strongly onto the slanted surface.

Finally, Ahmed et.al.(1984) also showed that the fully separated low drag flow state could also exist on (or slightly below) 30˚ by placing a vertical splitter plate in the middle of the wake region, indicating a strong sensitivity to small flow disturbances. Similar experiments were carried out by Sims-Williams (2001) which are discussed in the later sections of this chapter.

Lienheart et.al. (1999) performed experiments on the precritical and post critical rear slant angles of Ahmed models with 25˚ and 35˚ respectively (see figure 9). He conducted experiments in the LSTM low speed wind tunnel and

used a 2-component Laser Doppler Anemometer (LDA) on a traversing system to measure the velocity deficit in the wake.

Hot wire measurements on the velocity profiles were made. From the flow visualization techniques, he observed the presence of strong three-dimensional flow patterns. The skin friction visualizations revealed the presence of flow reversal for the 25˚ rear slant and direct separation for the 35˚ rear slant configuration. This was again verified with velocity vector plots along the symmetry plane for both the rear slant configurations. They clearly indicated the presence of a small separation bubble on the rear slant and the reattachment of flow before separating at the base leading to the formation a large wake, for the 25˚ rear slant configuration. For the 35˚ rear slant configuration, due to the detached flow from the slant, the development of a single large recirculation region was observed. Thus the results of Lienheart et.al. (1999) compared extremely well with the previous work after, Ahmed et.al. (1984) and thus the criticality of the 30˚ rear slant was observed.

Figure 9. *Pre and Post Critical cases of Ahmed model, after Lienheart et.al. (1999)*

The two counter-rotating vortices were clearly observed with peaks in Turbulent Kinetic Energy (TKE) occurring in the centres of these vortices. These vortices were responsible for maintaining attached flow at the slant upto a rear slant angle of approximately 30˚ after which it breaks down and the flow separates without getting attached to the slant surface (as observed in the 35˚ configuration).

Sims-Williams (2001) conducted similar studies on the time averaged and unsteady flow structure associated with the critical rear slant angle configuration of

(α=30˚) the Ahmed model geometry. The 30˚ rear slant configuration was mainly selected to demonstrate the criticality involved with the 30˚ configuration. Sims-Williams (2001) was able to show that the flow could be manually switched between high and low drag flow structures by using a flat plate to guide the flow onto the slant surface or to force it to separate (see figure 10). The experiments were performed at high (>5.9x10^5) and low Reynolds number (4.7x10^5). It was observed from the flow visualization techniques that at high Reynolds number the low drag flow structure could be observed only for a small time period after which the flow returned to the high drag state. Also, when analysed for lower Reynolds number, the low drag flow structures were observed for a sufficiently longer duration of time. Sims-Williams found from his experiments through wake traverses that, in the time averaged form the results agreed with those obtained by Ahmed et.al. (1984).

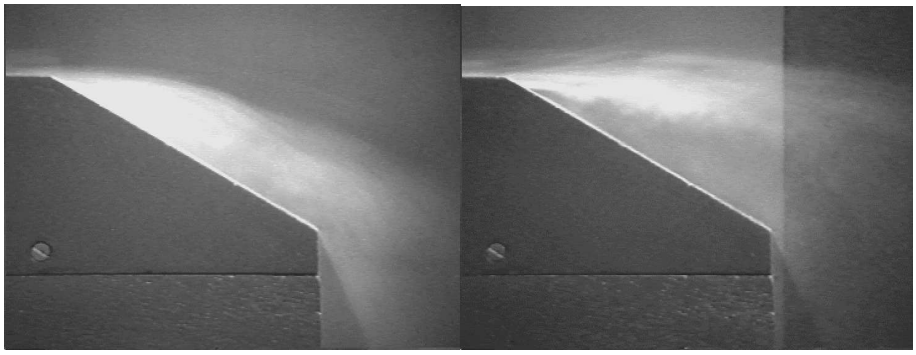

Figure 10. *Flow structures on the rear slant for low drag and high drag configurations, after Sims-Williams (2001)*

Spohn and Gillieron (2002) conducted experiments to analyse the flow structures in the wake of a 25˚ rear slant configuration of Ahmed model in low speed water tunnels. They analysed the flow separations associated in the front and the rear part of the model, along with the separations on the body and also the generation of vortical structures in the near wake region of the model. From their experiments, the flow separations on the roof of front part revealed the existence of separation lines, ending laterally into two foci on either side as the origin for the two counter rotating vortices as shown in figure 11(a)Spohn and Gillieron (2002) .

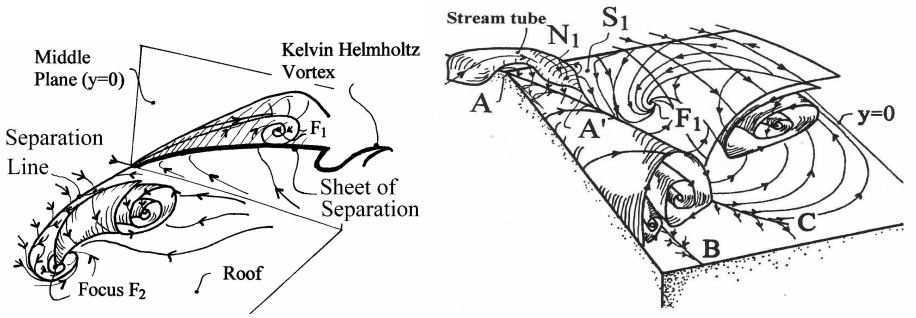

Figure 11 (a) & (b). *Flow separations at front and rear part of Ahmed model geometry, after Spohn and Gillieron (2002)*

The flow observation on the rear part revealed that the near wake region was influenced by a pair of counter rotating C-pillar vortices that encloses a separation bubble on the slant surface as shown in figure. From the figure 11 (b), after Spohn and Gillieron (2002) the position of these vortices implied the existence of the attachment line. Thus, line AB depicts the formation of C-pillar vortices and A'C represents the attachment of the main vortex. Also, their visualizations enabled to explain the skin friction patterns obtained, after Ahmed et.al. (1984), especially the flow reversal in the separation bubble region and the existence of two radiating foci located near the top corner of the rear slant surface.

Vino et.al. (2004) examined the critical rear slant angle (30˚) of Ahmed model geometry experimentally, to study the time averaged and time dependant nature of the wake flows at critical rear slant angle. His time averaged results showed excellent agreement with Sims-Williams (2001) and Ahmed et.al. (1984), as the surface skin clearly indicated the formation of C-pillar vortices, which was observed identically by both of the previous authors.

From the velocity vector plots, Vino et.al. (2004) observed the presence of two counter rotating, two dimensional vortices behind the base. He observed that towards the upper portion of the separated region, experienced significant levels of down wash at angles clearly larger than the backlight angle. Also, he found that the upper recirculation zone is fed by the fluid separating from the slanted edge. Thus, the flow over the slanted edge was found, not reattaching at the slant before separating at the base, which was contrary to the flow topology of Ahmed et.al. (1984). The revised

flow topology behind the 30˚ rear slant of Ahmed model, after Vino et.al. (2004) is shown in figure 12.

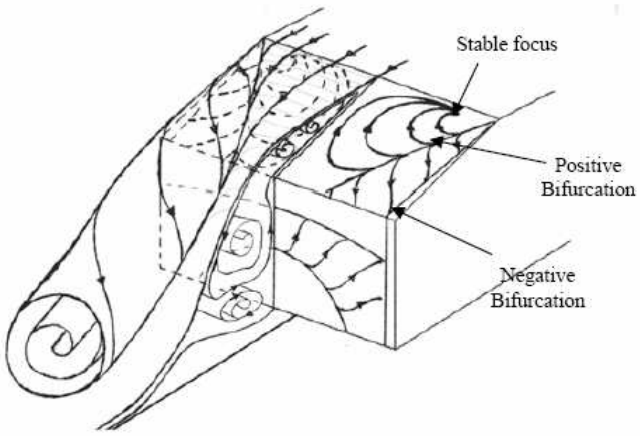

Figure 12. *Proposed flow structure on the critical rear slant angle of the Ahmed model, after Vino et.al (2004)*

Thus the closed horse shoe vortex proposed by Ahmed et.al. (1984) was observed to be partially opened and getting mixed with the upper recirculation bubble on the vertical base, by Vino et.al. (2004).

Nouzwa et.al. (1990) conducted experiments on notch back vehicle model, to analyse the flow characteristics in its wake region. They found that the rear deck lid complicated the flow behaviour and in-turn the wake region, since three important geometric parameters were required to be investigated. They are the height of the truck deck, the roof end position and the angle of the rear window.

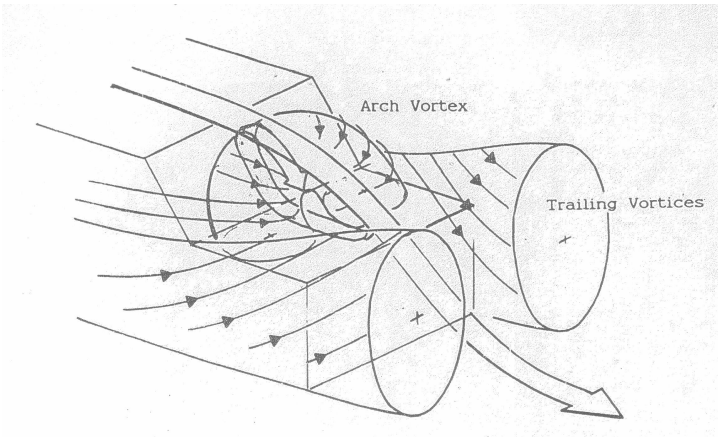

Figure 13. *Flow pattern for notchbacks, after Nouzawa et.al. (1990)*

From their experiments they observed that the drag coefficient was highest when the rear window angle was 25˚. This configuration was termed as the "Quasi critical geometry" and was recommended to be avoided for low drag applications. They plotted pressure contours, velocity vectors and vorticity contours for their notch back vehicle configuration. The pressure contour revealed the presence of longitudinal trailing vortices and vortices behind the window, since low pressures were recorded in those regions. The velocity vectors and vorticity contours indicated the separation of flow from the rear window aiding the formation of trailing vortices. Also, a region of reversed flow behind the trunk was observed to be influenced by the flow on the rear window. Thus, a clockwise vortex region was observed behind the trunk deck and the counter-clockwise vortex region behind the rear window which is shown in figure 13.

Nouzawa et.al. (1990) observed a distinct flow feature that is absent in the case of fast back configuration (see figure 13). They found a distinct, arch type vortex on the rear window and the deck lid. This particular vortex, which was observed in the quasi critical state, operates to be the main source for the increase of drag coefficients.

1.3.2 Unsteady Flows

Most of the previous studies in analysing the wake characteristics have been performed as time-averaged experiments. This gave an impression that flows are always steady, which is quite contrary to the real case scenario since vehicles exhibit highly unsteady flow characteristics, especially the shedding of vortices from the C-pillars.

Vino et.al. (2004) investigated the time-dependant characteristics in the wake of an Ahmed model of 30˚ rear slant angle. Pressure taps were attached to the rear slant and base of the model, which in turn were connected to the DPMS (Direct Pressure Measurement System). The DPMS was used to record the pressure fluctuations within the wake of the model.

From their experiments, based on the surface pressure data on the rear slant and the vertical rear base, a single dominant shedding frequency, which corresponds to a Strouhal number between 0.36 and 0.39, was observed. This also indicated the presence of high energies associated with the shedding. The surface pressure results on the rear slant and the rear vertical base clearly represented the two recirculatory bubbles that were observed in the time averaged experiments. Additionally, these bubbles were found to be analogous to longitudinal vortex in a von Karman vortex sheet, shedding alternately at a Strouhal number of about 0.39.

Sims-Williams (2001) analysed the unsteady behaviour in the wake of the Ahmed model geometry. From his experiments, he found that high levels of unsteadiness existed in the wake, with the highest levels located around the periphery of the C-pillar vortices. Also, it was found that these regions of high unsteadiness were associated with a distinct shedding frequency, giving a Strouhal number of about 0.35 (based on a characteristic length equal to the square-root of the frontal area).

Nouzawa et.al. (1992) extended their previous time-averaged investigations on notch back model to a time-dependant experimental study. From their experiments they found that for the critical slant or the apparent angle of 25˚, the arch type vortex that was produced on the rear window and the deck lid, exhibited significant unsteady characteristics. This was measured using hot-wire and pressure measurement systems. The measurements clearly indicated that the arch type vortex sheds from the model in an alternate manner with a shedding frequency ranging between 20 and 30 Hz. This inturn was correlated to the fluctuating drag coefficients exhibited by the model and it was concluded that the arch type vortex influences a significant part on the model's aerodynamic properties and particularly the drag coefficients.

1.4 Effects of Inter-Vehicle Spacing on Vehicle Aerodynamics

The performance, handling and safety of a road vehicle are determined to a great extent by the flow characteristics around the vehicle. The external flow

determines the forces and moments in six degrees of freedom which inturn contributes to the vehicle's overall performance. The interference between road-vehicles imposes additional forces particularly side forces and yawing moments on vehicles. The effects of inter-vehicle spacing or drafting on vehicle's aerodynamic coefficients were analysed by A. F. Abdel Azim (1994) and observed drastic gust loads from his experiments, when driven in close proximity to others (either stationary or movable). Recently, Vino and Watkins (2004) studied the effects of drafting using generic car model and found that in addition to the spacing effects; the vortex interaction between models played a significant role in determining the drag coefficients of the vehicle.

1.4.1 Platoon or Convoy Driving

An increase in traffic density leads to the formation of platooning of vehicles, one behind the other. Under such conditions considerable favourable interference can occur between vehicles, with a distinct turbulent wake following each vehicle. Thus, the reduced dynamic pressure in the wake of the first vehicle influences the drag coefficient of the vehicle behind (trailing vehicle). Consequently, considerable improvements in aerodynamic drag can be achieved even when the distance between the vehicles is relatively great which is observed by Bernard R (1996), A. F. Abdel Azim(1994) and Vino and Watkins (2004).

The effect of aerodynamic interaction between commercial vehicles was studied by Gotz (1983). From his study he found that when a convoy of commercial vehicles are driven at speeds of 80 km/h with an inter-vehicle spacing of 40 m, a reduction in drag force of 20% would be obtained for the second vehicle and around 30% for the third and every additional vehicle in the platoon.

1.4.1.1 Previous studies on inter-vehicle spacing

Realistic flow interaction experiments between two cars were performed by Abdel Azim and Abdel Gawad (2000). They analysed a number of cases on a single model, convoy, cars moving side by side and an overtaking phenomenon. They used two 1/60 scaled models of Mercedes Benz C 280 for their experiments on analysing

the effects of drafting and Reynold's number on the flow structures in the gap region between the lead and the trailing car. In their experiments the models were subjected to two different Reynolds numbers (for Re ≈ 6000 and Re ≈ 11,000). However it should be noted that these are extremely low Reynolds numbers.

From the convoy case, they observed the existence of three main flow modes between the lead and trailing cars, depending on speed and spacing, in the area between the leading and following cars: a wake impingement, steady vortex wake, and a low-pressure cavity.

They observed from their experiments that when the longitudinal spacing was one car length at a Reynolds of 6000 based on model length, the separating shear layers from the leading car form intermittent vortices, impinged on the trailing car. Further as the Reynolds number was increased through to about 11000, the separating shear layers from the leading car reattached on the body of the trailing car and created a low-pressure cavity as the smoke disappears between the two cars, which can be seen from figure 14.

At half a car length, the separating shear layer from the leading car rolled up into a steady vortex at a Reynolds number of about 6000. As the Reynolds number was increased to about 11000, as appeared in the previous cases the steady vortex was found to disappear leading to the regeneration of low-pressure cavity between the vehicles.

Finally, at a longitudinal spacing of a third of a car length, the steady vortex reappeared although only at highest Reynolds number of about 11000.

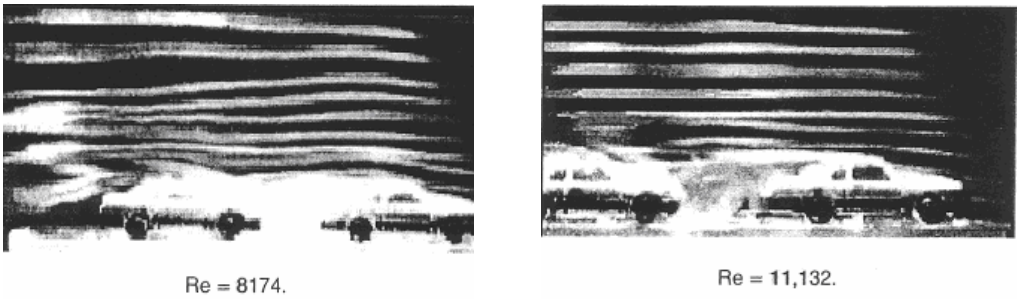

Figure 14. *Flow visualization of two car convoy with longitudinal spacing x = 1/3Lc, after Abdel Azim and Abdel Gawad (2000)*

From their experiments they found that at close proximities (i.e. at close inter-vehicle spacing) the trailing model experiences considerable drag savings. It was also found that the low-pressure cavity mode produces the largest reduction, since the front part of the trailing model is entirely immersed into the low pressure cavity region.

Tsuei and Savas (2001) investigated the transient aerodynamic effects in a four-vehicle platoon during passing maneuvers and in-line oscillations. They used a vehicle model which was moved longitudinally parallel to a four-car platoon to simulate passing manoeuvres, as shown in figure 15. From their experiments they found that each vehicle model in the platoon experienced a repulsive side force, when the overtaking/passing vehicle model moved in the neighbourhood of their (platoon member) rear half; the side force direction was found to become reversed and turn into an attractive side force when the overtaking vehicle was moved in the neighbour hood of their front half. They also found that the drag force experienced by each platoon member increased when the overtaking/ passing vehicle was in close proximity. Additionally, similar trends were observed from their investigations on a platoon overtaking a vehicle.

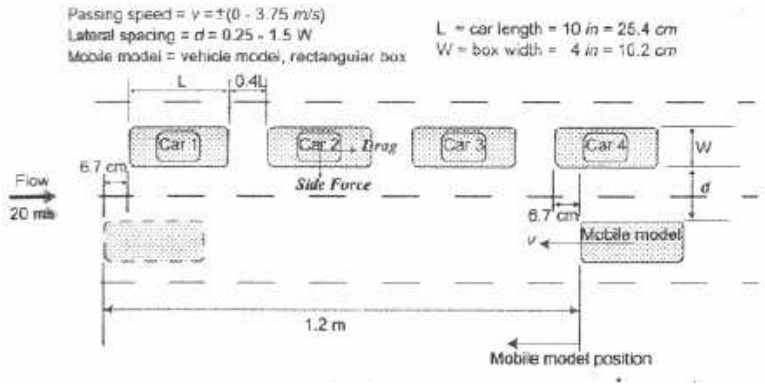

Figure 15. *Platoon configuration and mobile model, after Tsuei and Savas (2001)*

In the case of a four-car platoon, the drag variations experienced by the vehicles adjacent to the oscillating vehicle were discussed using a cavity model. They found that when the oscillating or moving vehicle model moved towards its upstream member in the platoon, the drag coefficient of the moving model and the downstream model increased, while the upstream model was found to experience minimal drag

coefficients. These effects on drag coefficients were found to be directly opposite when the oscillating vehicle model moved in the reverse direction i.e. away from its front neighbour. Tsuei and Savas (2001) also investigated the effects of relative velocity between platoon members and the passing vehicle. They found that smaller relative velocities amplify the forces experienced by the platoon members by as much as 70% for drag and 60% for side force.

Zabat et.al. (1994), studied experimentally the effects of inter-vehicle spacing on drag coefficients of vehicles using typical mini-van geometries. From their experiments, they found that significant drag savings were experienced by both the lead and the trailing model at close proximity, with the lead model benefiting greater and the trailing model benefits are evenly distributed trend over the spacing. They observed that at close proximity (as emphasized in figure 16) between the region $0 < x/L < 0.35$ (Where x is the spacing, L is the length of the model used), the trailing model's drag coefficients were larger than the drag coefficients of the lead model. Between the specified regions, the trailing model's drag coefficient was observed to reach a maximum of 76% and a minimum of 69%, which was more than the isolated model's drag coefficient.

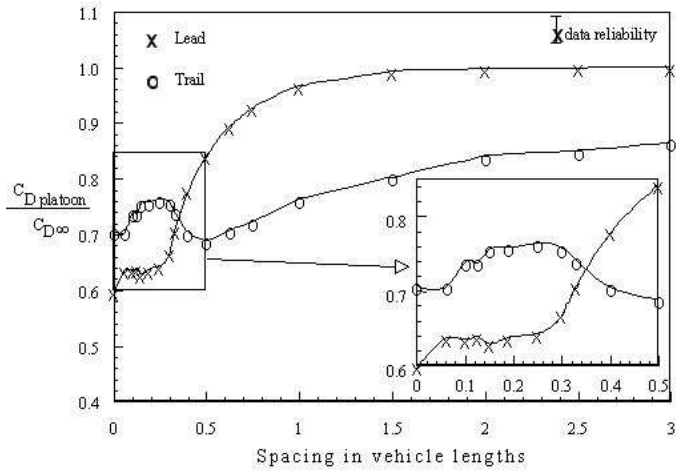

Figure 16. *Drag variation of two mini-vans at close longitudinal spacing, after Zabat et.al. (1994)*

Finally Watkins and Vino (2004) conducted experiments to understand the effects of inter-vehicle spacing using two Ahmed car models. Significant drag increases were found for the rear Ahmed body at close spacings. They also observed

that significant drag penalties can be experienced by both the models at close inter-vehicle spacing. The following figure 17 shows the fluctuations of drag coefficient for both the models at close spacing.

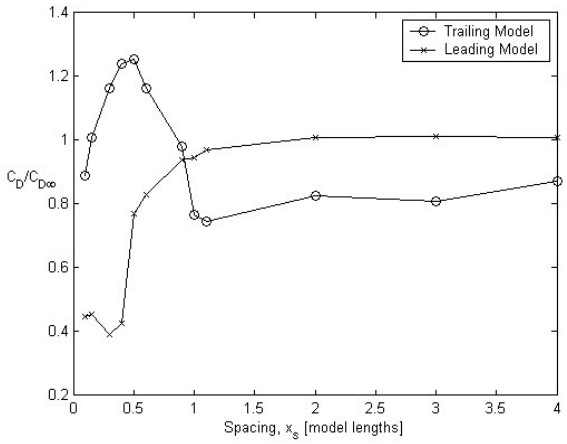

Figure 17. *Effects of inter-vehicle spacing on drag coefficients after Watkins and Vino (2004)*

They concluded that vortex interaction is the primary source for the increase of drag coefficients for the rear model at close spacing and suggested that more understanding is required to analyse their effects in detail.

1.5 Future Generation Intelligent Transport System (FGITS)

Future Generation Intelligent Transportation Systems (FGITS) encompass a broad range of wireless and wire line communications-based information and electronics technologies. When integrated into the transportation system's infrastructure, and in vehicles themselves, these technologies relieve congestion, improve safety and enhance productivity. The vehicles in FGITS are equipped with devices like collision avoidance systems, collision notification systems and driver assistance systems like Adaptive Cruise Control (ACC) systems. Additionally, information on the topography like weather, road conditions (Traffic or accident) are provided to the user by these systems. The communication based transport systems with which vehicles are expected to travel in Automated Highway System (AHS) are

shown in figure 18. All these infrastructures could be better utilized on major arterials to satisfy a range of objectives spanning minimized collision avoidance, lessened driver fatigue, increased traffic throughput, lower emissions, and even reduced fleet energy consumption.

Figure 18. *FGITS and vehicle platooning (Courtesy, PATH 1997)*

Reduced energy consumption is particularly popular amongst road vehicle aerodynamicists. Drag coefficient contributes more than 70% of the overall fuel consumed by a vehicle (W.H. Hucho, 1998). When attempts are made to reduce the drag coefficient considerable energy can be saved. One way of attaining this reduction in drag coefficient is by forming a string of vehicles similar to the railway carriage arrangement. This is can be achieved by reducing the inter-vehicle spacing between vehicles, which saves considerable drag coefficients for all the vehicles (Zabat et.al., 1995). Additionally it leads to the formation of a platoon, which is "the organisation of closely spaced groups of vehicles" and enables to increase the highway throughput (Horowitz, 1996).

Much of this research concerns use of models of existing practical forms: conversely, modern road vehicles are represented by a variety of basic geometric configurations, each with corresponding basic wake effects; these are in turn further compounded by very complex surface details that whilst yielding parasitic drag effects might change the nature of the wake (and the subsequent scope for drag reduction via platooning markedly). The use of basic vehicle shapes has proved to be extremely useful for predicting the fundamental flow physics associated with complex vehicle geometries and this phenomenon was investigated by Le Good and Garry (2004).

"Much control systems research and engineering efforts are directed to the formulation of such "control laws" that define how FGITS vehicles and their surrounding infrastructure interact. It is the control law that will ultimately define vehicle spacing for a set of system conditions; traffic speed, throughput considerations and various safety factors (e.g. collision avoidance) are all pertinent contributors to control law definition. In much research to this end – albeit at a preliminary stage – aerodynamic concerns do not presently feature in control law design" after Pagliarella et.al. (2005). Therefore the existing research (particularly given safety concerns) cites vehicle spacing far greater than those researched in the aerodynamic domain.

1.6 CFD for Aerodynamics Study

1.6.1 Introduction

The traditional predictive tools used in the industry to evaluate aerodynamic performance of automobiles are wind tunnel tests and road tests (W.H Hucho 1998). Wind tunnels are expensive to build and operate. They require a large amount of area for accommodating all components even though the test section might be only a small portion of it. Wind tunnels in automotive industries are often big enough to test their full sized vehicles. In spite of the possibility of testing real full- size vehicles, the finite size of the test section, complexities of operating moving ground rigs, and inadequacy of testing under side wind conditions, etc., impose limitations on simulating realistic flow conditions. On the other hand scaled models of vehicles are used for flow replication of full sized vehicles. These models may not possess the realistic characteristics of a complete vehicle, for example these models may not have engine cooling systems, cabin ventilation systems. In addition wall boundary layer and model support interference effects, model & wake blockage effects, effects of flow-intrusive probes, etc., would be present while testing these scaled models and measures has to be taken to overcome these difficulties before they are subjected to tests (W.H Hucho 1998).

Road tests are more realistic i.e. testing vehicles in a more realistic environment. The difficulties associated with ever changing wind conditions often make these results open to debate. Great care is needed to make these results meaningful and conclusive (W.H. Hucho, 1998).

In order to meet the consumer's demand and to reduce cost and time-to-market, automobile manufacturers have to develop more economical, safer and more comfortable vehicles at an increasingly rapid pace. Traditional wind tunnel testing and road testing techniques takes long development cycle times. In order to overcome these difficulties and to stay in the competitive market automotive manufacturers started concentrating on computational techniques to simulate wind tunnel tests called Computational Fluid Dynamics (CFD). CFD and model scale tests are used increasingly in car development with full-size wind tunnels used for validation and refinement or global simulation of the entire flow field rather than for extensive parameter studies as in the current industrial practice (W.H. Hucho, 1998).

CFD simulations are well suited to analyse a wide range of shape options. These simulations are most useful in predicting trends of how shape changes will affect flow field features of vehicles. Sometimes a CFD simulation permits the investigation of simulations that cannot be realistically duplicated in a wind tunnel. For example most tunnel test sections are designed for development on single vehicles thus studying several vehicles in a platoon is difficult. The aerodynamics of two or more vehicles at very close proximities in passing or overtaking mode, poses a difficult problem for wind tunnel tests. Positioning (aligning) the model at extremely close proximities is a problem before performing a wind tunnel test. Hence the current study on the effects of platooning on vehicle's aerodynamics is performed using CFD where models with different rear slant angles are positioned at different inter-vehicle spacing to study their corresponding aerodynamic effects.

The commercial suppliers of general-purpose CFD packages have led the developments in software that has enabled such applications to become commonplace. These tools are now used extensively throughout the automotive and aeronautical industries by various departments not only to study external aerodynamics but also to study engine cooling systems, cabin ventilation, etc. It is

only in the largest companies that any significant development of CFD software continues, usually where customized coding can offer advantages in efficiency or accuracy for a particular, usually narrow application, such as wing design.

1.6.2 Previous Studies using CFD on Ahmed models

Gillieron and Chometon (1999) used the Ahmed car models of 25˚ and 35˚ rear slant angle configurations for analysing the turbulent flow structures. A numerical scheme was used to validate the experiments that were carried out on using Ahmed model in a wind tunnel. The model was surrounded by 15000 triangular elements constructed using version 7.2 of ANSA software. Volume meshing was obtained using version 3.0 of the Fluent Tgrid 3D software. Across all geometrical configurations, the model had a total of around 300,000 prism and tetrahedral volume cells. Computations were performed using version 4.2 of Fluent software and the turbulence model used was k-ε turbulence model with a logarithmic law on the wall.

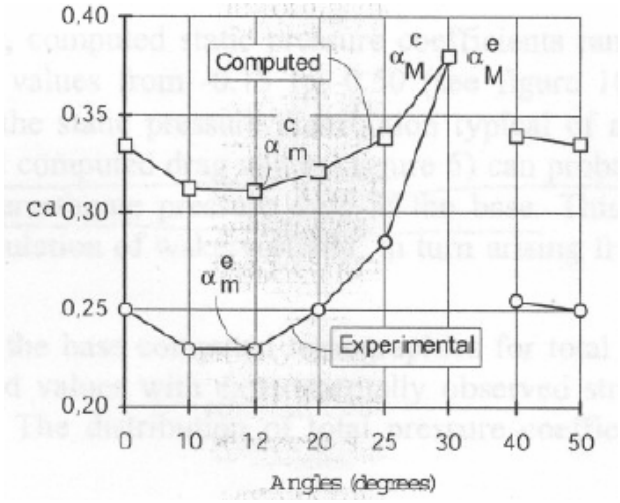

Figure 19. *Computed and experimental drag coefficients for various rear slants of Ahmed model after Gillieron and Chometon (1999)*

The ground effect that causes the vortex systems to develop into two counter rotating horse shoe vortices near the base of the Ahmed model were replicated. The computed results obtained on the Ahmed model were found to be in agreement with the experimental results obtained from the wind tunnel. In particular, the computations had successfully reproduced changes in vortex wake flows and aerodynamic drag coefficients. It was concluded that the over predicted computed

drag values in figure 19 were because of the code's tendency to overestimate base pressure drop. The results also revealed that CFD simulations are promising techniques for investigating phenomena in automotive aerodynamics.

David Sims-Williams et.al (2002) analysed the unsteady wake of the Ahmed model with 25˚ rear slant angle both experimentally and computationally. An unsteady reconstruction technique was used to visualize the unsteady wake flows. The computational simulations were performed using Exa Power FLOW and the CFD results were found to be in close comparison with the experimental results. It was found that the vortex shedding type from the bottom of the model's base, on the wake centreline and the two dimensional behaviour near the centreline produces symmetric oscillation in strength and thereby determines the position of rear 'C' pillar vortices. This phenomenon was observed both experimentally and computationally and it was concluded that the oscillation corresponds to a Strouhal number of approximately 0.5 based on free stream velocity and the square root of the model frontal area.

SiniŠa Krajnović and Lars Davidson (2004) also performed LES on 25˚ rear slant Ahmed models at a Reynolds number of $Re = 2 \times 10^5$ which resulted in the flow around rear part of the simplified car similar to one in the experiments at higher Reynolds number ($Re = 7.68 \times 10^5$). Their results indicated that for the existing geometry the external vehicle flows at high Reynolds number becomes insensitive to Reynolds number. It was found that the geometry rather than the viscosity dictates the character of the flow and the positions of flow separations. Also it was observed that while using lower Reynolds number the near wall energy carrying coherent structures can be resolved and the flow could be predicted more accurately. This observation raised hope that flow around real cars could be simulated with LES at reduced Reynolds numbers.

C. Hinterberger et.al (2004) conducted experiments on 25˚ rear slant Ahmed models and concluded that the results obtained through Large Eddy Simulation (LES) are promising. The comparisons with the experiments showed well captured flow structures.

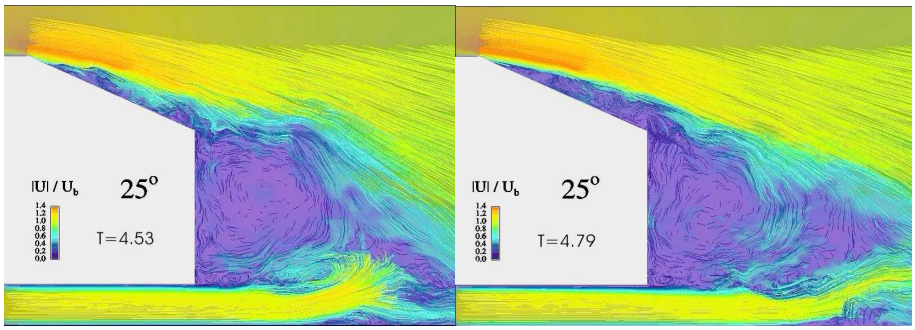

Figure 20. *Instantaneous streamwise velocity fields in the symmetry plane, after C. Hinterberger et.al. (2004)*

R.K. Strachan et.al. (2004) compared Laser Doppler Anemometry (LDA) data to a CFD solution run on Fluent 6.0 employing k-ε RNG turbulence model for a transverse plane one model length down stream of an Ahmed reference model. The CFD model predicted the counter-rotating vortices at this point in the flow very well. However there was a discrepancy in the position of the vortices between experimental and computational data. This discrepancy was thought in part to be caused by an alignment error in the model during testing. The CFD model was also compared to a previous study employing a Detached Eddy Simulation (DES) turbulence model in the near wake of the Ahmed body. The correlation between the two models proved to be good, as the different ground simulations employed could account for most differences between them. Force measurements were also taken from the current experiment and these as well as CFD force values were compared against a previous study. It was concluded that computational drag force predictions fluctuated within 3%. In addition comparison of the CFD model with Ahmed's original experiment showed small discrepancies between the predicted drag coefficients over each part of the model.

Francis T. Makowski and Sung-Eun Kim (2000) worked on the numerical prediction of the aerodynamics around cars using Reynolds Averaged Navier Stokes equations and unstructured mesh. From their research they concluded that the unstructured hybrid mesh with a solution adaptive mesh refinement capability was of great benefit to predict external aerodynamic flows around ground vehicles. In particular the meshing strategy of using tetrahedral elements in combination with prismatic near–wall elements was a viable approach for significant reduction of meshing time; also its flexibility was useful in dealing with complicated geometry and

its ability to resolve widely-varying scales in the flow. Reynolds Averaged Navier Stokes Equation (RANS) simulation in combination with second moment turbulent closure and wall functions represents a cost effective strategy for modelling turbulent flows past ground vehicles like the strong streamline curvature, cross flow, three dimensional flow separation, vortex generation and flow reversals.

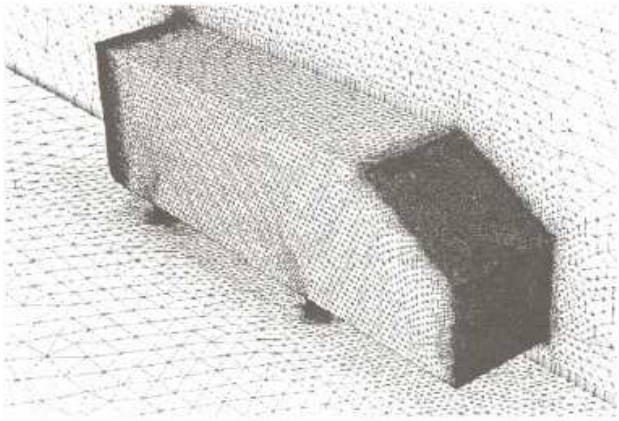

Figure 21. *Surface mesh of Ahmed model with 30˚ rear slant angle, after Francis T. Makowski and Sung-Eun Kim (2000)*

They conducted experiments on Ahmed car model with critical rear slant angle of 30˚, shown in figure 21 and the simulations were performed for two different turbulence models; the Standard k-ε model and the Reynolds Stress Model (RSM). They concluded that the Standard k-ε model over predicts the effective viscosity in regions where the turbulence is anisotropic and the RSM was able to demonstrate all the salient flow features observed in the experiments.

Kapadia and Roy (2003) performed the wake flow simulation of Ahmed reference model with 25˚ rear slant using DES as a turbulence model. Further, results are obtained using RANS model for same time -steps and were compared with DES results at a particular time-step. Their comparison showed the ability of DES in capturing unsteady structure of the flow with minor flow details was better than RANS. Drag coefficient was calculated in both simulations and compared with the established results. Their comparison found similarity between DES results and

experimental work by Ahmed et al 1984 and similarity between RANS results and numerical results of Gillieron and Chometon (1999).

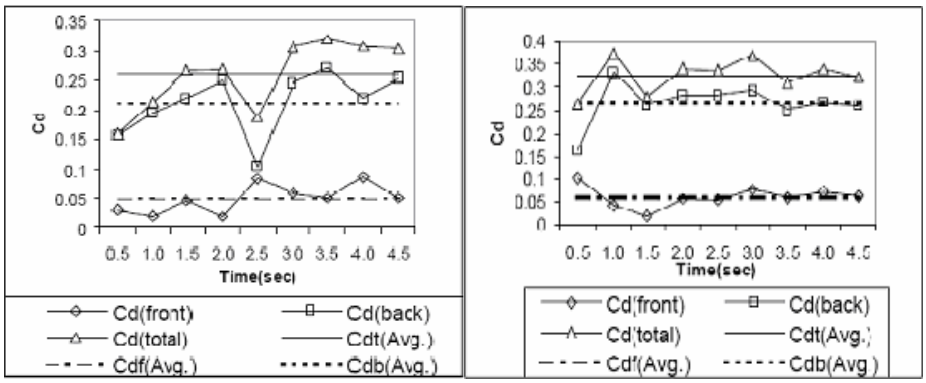

Figure 22. *Time-study of CD (DES) Figure (a) and Time -Study of CD (RANS) Figure (b) after Sagar Kapadia et.al. 2003*

1.6.3 Conclusion from EFD and CFD on Ahmed body

All of the previous CFD studies have been conducted on isolated Ahmed models for various rear slant angles using RANS or other turbulence models and only one of the studies in EFD has been performed on spacing two Ahmed models, after Vino and Watkins (2004). The current study aims to study the aerodynamic effects on a platoon of vehicles using Ahmed models for various rear slant angles to simulate a variety of vehicle geometries and spacings.

The main reasons that have led to study the effects of platooning on vehicle's aerodynamics using Computational Fluid Dynamics (CFD) are explained below.

To simulate platooning or realistic traffic topology experimentally several scaled vehicles ("scaled" since it is not feasible to have a number of full scale vehicles inside the test section) are required to be positioned one behind the other. Irrespective of the tunnel test section type, this poses problems of scale, since wind tunnel sections are designed for vehicles in isolation. The scaling should be done depending upon the number of models required to be mounted on the tunnel section which in-turn depends on the size of the test section. In fixed ground tunnels, floor (or ground board)

boundary layer growth is such that the downstream vehicles are unduly influenced by the floor boundary layer.

To study the effects of platooning on the aerodynamic properties of vehicles, a simplified geometry model with the ability to reproduce a range of car-type is desirable and as the most popular to date is the Ahmed car model, is used for the current study.

1.6.3.1 Scope

The wind tunnel at RMIT has a test section of 9m long 3m wide and 2m high. Having many models inside the tunnel and varying the spacing between models from 0.25L to 4L is not feasible [L is the model length of an Ahmed car model which is 1.044 m]. Hence CFD can overcome these circumstances of space constraint.

The test domains in CFD can be constructed depending on the requirement and there are no general limits on domain size as hundreds of models can be mounted in the test domain. In spite of CFD's edge over conventional wind tunnels in space and cost effectiveness the wind tunnels tests cannot be ignored. They are the conventional methods of testing models and their predictions of force coefficients are generally very accurate and often are used to validate CFD results. Hence for the current study on platooning, in order to validate the computational turbulence model, selected tests are performed in the wind tunnel for a platoon of 2 to 3 models and inter-vehicle spacing of up to 3 body lengths in the case of 3 model platoon, or 4 body lengths in the case of 2 model platoon are used. This enabled to select the appropriate turbulent scheme for the remaining tests. Once these results are validated, the study is extended computationally up to 7 models. This was to quantify how many models are needed to simulate an infinitely long platoon.

The number of test combinations to simulate realistic traffic is infinite (for example a sedan followed by a hatch or a coupe followed by a van). The setting up time for removing and mounting the models in wind tunnel is usually significant and it can be performed more easily using computational methods. As it was found (see

later) that six models were sufficient to simulate an infinite platoon, the effect of rear slant angle (between 0˚ – 40˚) was investigated for this number of simulated vehicles.

Detailed flow visualizations were obtained in CFD in order to understand the aerodynamic force behaviour.

1.7 Research Objectives

To broaden the current published knowledge of the aerodynamic behaviour of road cars in representative flow environments, the main objectives of this research are as follows.

a. Determining the effects of aerodynamic forces and flow structures over isolated 2D and 3D Ahmed car model and also determining the effects of drafting on drag coefficients for the same.
b. Preliminary validation of CFD for selected 3D cases by using the experimental results of Vino and Watkins (2004) for two 100% scale Ahmed models with 30˚ rear slant angle.
c. Determining the effects of inter-vehicle spacing on drag coefficient using two different scales of Ahmed models of 30˚ rear slant configuration.
d. Determining the effects of inter-vehicle spacing and rear slant angles on drag coefficient using Ahmed car models for multiple model platoons.

2. Computational Fluid Dynamics (CFD) Analysis

2.1 Introduction

Computational Fluid Dynamics (CFD) is one of the most powerful and useful tools for predicting the external flow behaviour over ground vehicles. The emergence of CFD has made the use of wind tunnels only during the initial stages of a vehicle design (aerodynamic) program and once these initial experimental results are validated by the CFD code, the further extensions of work can be performed computationally. Thus the time involved for model making, mounting and testing at each and every stage can be neglected through these computational methods. Any design modification required can be performed with the available CAD softwares and can be analysed again with the available CFD tool. Thus repeating this cycle enables to reach an optimized design with less running cost.

The current study on the effects of inter-vehicle spacing and the influence of rear end geometries of vehicle on their aerodynamic coefficients when traveling in platoons are analyzed using CFD. The study is divided into four different phases, initially the models to be analyzed (The Ahmed car models) are solid modeled using a solid modeling package (for the current study Solid Works 2004) and are saved as *.IGS files. These models are then imported to GAMBIT where test domains are created around them. The domain along with the model(s) is meshed and respective boundary conditions are assigned and saved as *.msh file. As a final stage these mesh files are exported to Fluent to perform the CFD analysis and predict the aerodynamic behaviour of the models.

The process is repeated for various rear end geometries and for various inter-vehicle spacing. Thus, the current chapter deals with the grid generation using the available commercial software GAMBIT followed by CFD analysis using the available commercial CFD tool, FLUENT 6.1.22.

2.2 Selection of Grids

FLUENT can use grids that comprises triangular or quadrilateral cells (or a combination of the two) in 2D, and tetrahedral, hexahedral, pyramid, or wedge cells (or a combination of these) in 3D. The choice of which mesh type to use will depend on the application. When choosing the mesh type, the following issues should be considered,

- Setup time
- Computational expense
- Numerical diffusion (Post processing)

To clarify the trade-offs inherent in the selection of mesh type, these issues are discussed further

2.2.1 Size Functions

A size function allows controlling the size of mesh intervals for edges and meshing elements for faces or volumes. Size functions are similar to boundary layers in that they control the mesh characteristics in the proximity of the entities to which they are attached. They differ from boundary layers with respect to the manner in which they are defined and the manner in which they control the mesh. Whereas boundary layers prescribe specific mesh patterns and the sizes of mesh elements within those patterns, size functions control the following properties:

- Maximum mesh-element edge lengths (fixed-type size function)
- Angles between normals for adjacent mesh elements (curvature-type size function)
- Number of mesh elements employed in the gaps between two geometric entities (proximity-type size function)

The “Create Size Function” command creates a size function and attaches it to a specified entity. A size function allows controlling the size of the mesh in regions surrounding a specified entity. Specifically, they can be used to limit the mesh-interval size on any edge or the mesh-element size on any face or volume.

An example of the effect of size functions on the current study is shown in the figure 23 (a) & (b) below,

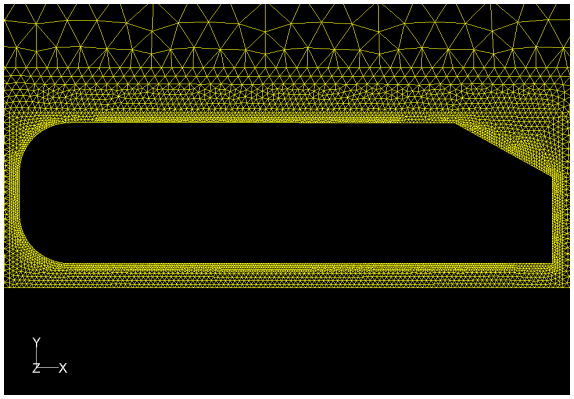

(a) Fine cells surrounding the model

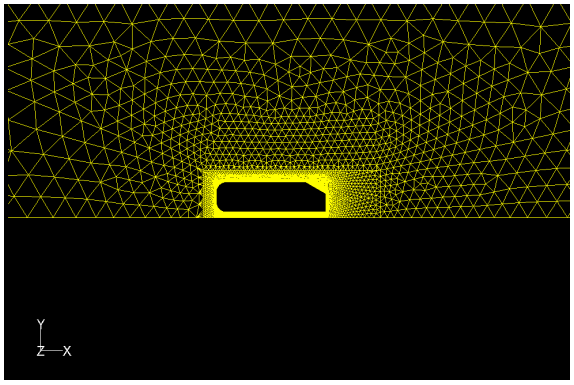

(b) Larger cell size away from the model

Figure 23 (a) & (b). *Grid generation using size functions*

In this example, a size function has been attached to the volume and defined with respect to the faces of the Ahmed model. When the volume is meshed using tetrahedral elements, the size function restricts the size of the element edges in proximity to the source faces. As a result, the tetrahedral elements in the region surrounding the source faces are small in comparison to those used to mesh the volume as a whole, and the mesh-element edge length increases with distance from the source face.

2.2.4.1 Size-Function Specifications

To create a size function, the following specifications must be defined:

- Type
- Entities
- Parameters

The type specification determines the algorithm used by the size function to control the mesh-element edge size. The entities specification determines the geometric entities that are used as the source and attachment entities for the size function. The size function parameters define the exact characteristics of the size function.

2.3 Grid Generation using GAMBIT

This section presents the use of mesh generator, GAMBIT, to develop 2D and 3D mesh for Ahmed car models. GAMBIT is a single, integrated pre-processor for CFD analysis. It has ACIS solid modeling capabilities, which enable the user to import CAD solid model files directly. It has the capability of reading IGES CAD format, which has only the information of the vertices and surfaces. GAMBIT enables the user to cleanup and modifies the geometry for grid generation purposes. This software can generate mesh for FLUENT solvers. It enables the user to generate a grid in structured and unstructured hexahedral, tetrahedral, pyramid, and prisms and assign boundary zones to the grid.

Different CFD problems require different mesh types, and GAMBIT gives user all the options needed for these applications. Meshing toolkit in GAMBIT lets user decompose geometries for structured hex meshing or perform automated hex meshing with control over clustering. Triangular surface meshes and tetrahedral volume meshes can be created within a single environment, along with pyramids and prisms for hybrid meshing.

2.3.1 Two Dimensional (2D) Model Meshing

2.3.1.1 Isolated Model

The Ahmed model is analyzed in isolation for its various rear end geometries (rear slant angles) is shown below in figure 24.

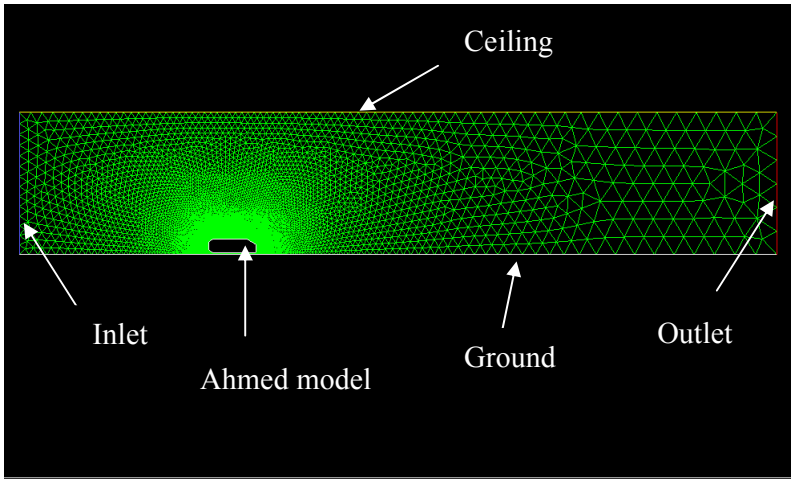

Figure 24. *Domain arrangement for 2D analysis of an isolated Ahmed model*

The figure 24 shows the 2D domain for an Isolated Ahmed model, which contains an inlet, outlet, ground and a ceiling. The flow area is meshed in different grid species in order to get more accurate simulation results and less computational time using the size functions option.

As shown in figure 25 (a), the Ahmed car model is surrounded by a very fine grid, since this area is extremely important for recording flow structures. Boundary layers are created along the walls of the Ahmed model to accurately simulate the flow separations from its rear slant and the two dimensional vortex formations at the model's base. The triangular grid, shown in figure 25, is applied to the entire domain. The locations of the inlet and outlet are placed far enough so that the flow is fully developed before it reaches the model and also the wake flow can be recorded completely once the flow leaves the model. The ground (Floor) is positioned 0.05m from the bottom of the model as a standard ground clearance for all the tests.

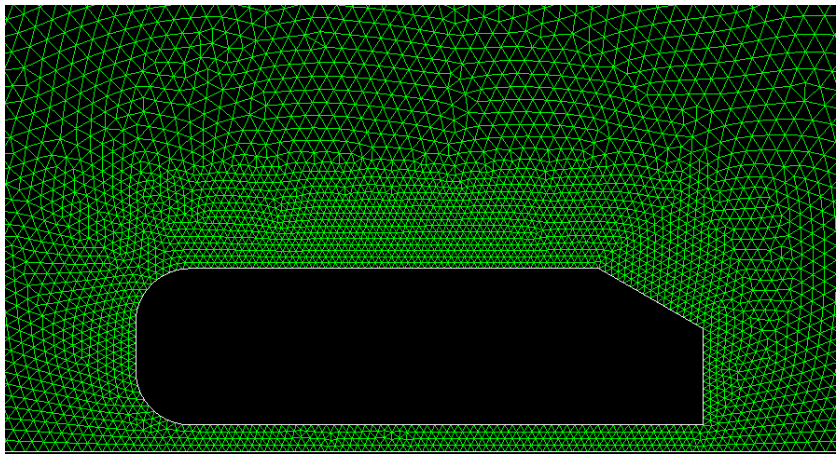

(a)

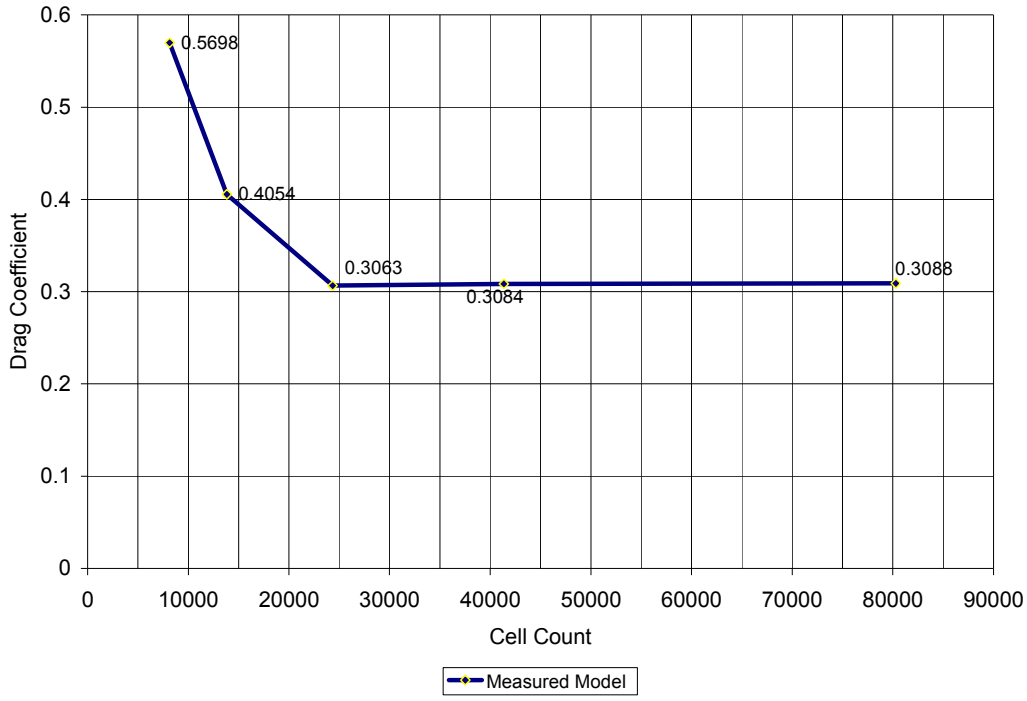

(b)

Figure 25 (a). *Mesh generation using size functions around the Ahmed model* **(b).** *Grid independency test for Ahmed model with 30˚ rear slant angle*

Grid refinement tests indicate that a grid size of approximately 25,000 cells provide sufficient accuracy and resolution to be adopted as the standard for all future working grids when models are analyzed in isolation. The grid independency test performed for isolated 30˚ rear slant configuration of 2D Ahmed model is shown in figure 25 (b).

2.3.1.2 Two Models in Tandem

The above procedure is followed for meshing two models in tandem, to study two dimensionally the effects of inter-vehicle spacing and rear slant angle on aerodynamic drag coefficient of vehicles. The study is carried on for two identical models in tandem i.e. both the model possesses identical rear slant angles (30˚) and the only variable for every case is the inter vehicle spacing (x/L), which is varied between 0 and 5L, where L is the length of the Ahmed model (L=1.044m).

The figure 26 (a) shows the grid generation and domain information for two Ahmed models of identical rear slant angles in tandem. Just similar to the isolated model case fine grids were generated around the Ahmed models and the area in between them, for recording the additional information on vortex interaction along with the flow separation and vortex generation at the model's base. The above process is carried on for various inter-vehicle spacing starting form 0.25L – 4L (Where L =1.044, length of the Ahmed model).

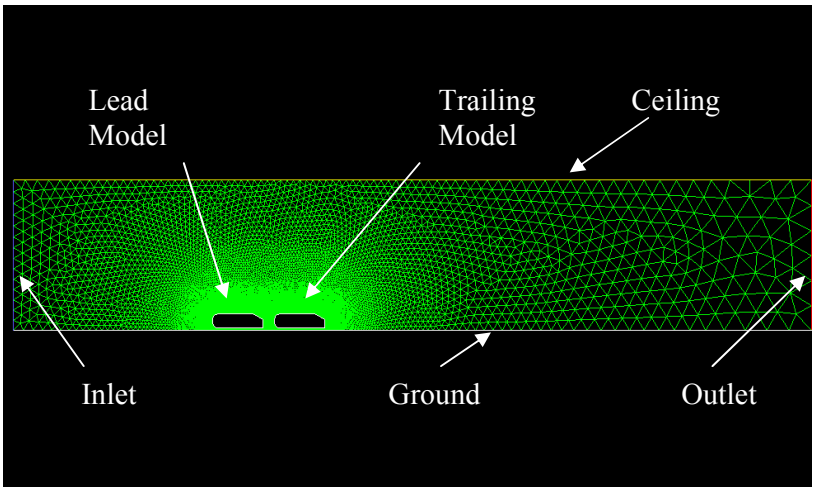

26 (a)

Grid refinement tests were carried on for the above drafting arrangement and it indicated that a grid size of approximately 47,000 cells provide sufficient accuracy and resolution to be adopted as the standard for all future working grids when two models in tandem were analyzed two dimensionally. The grid independency test

performed for the drafting arrangement at an inter-vehicle spacing of x/L=1 is shown in figure 26 (b).

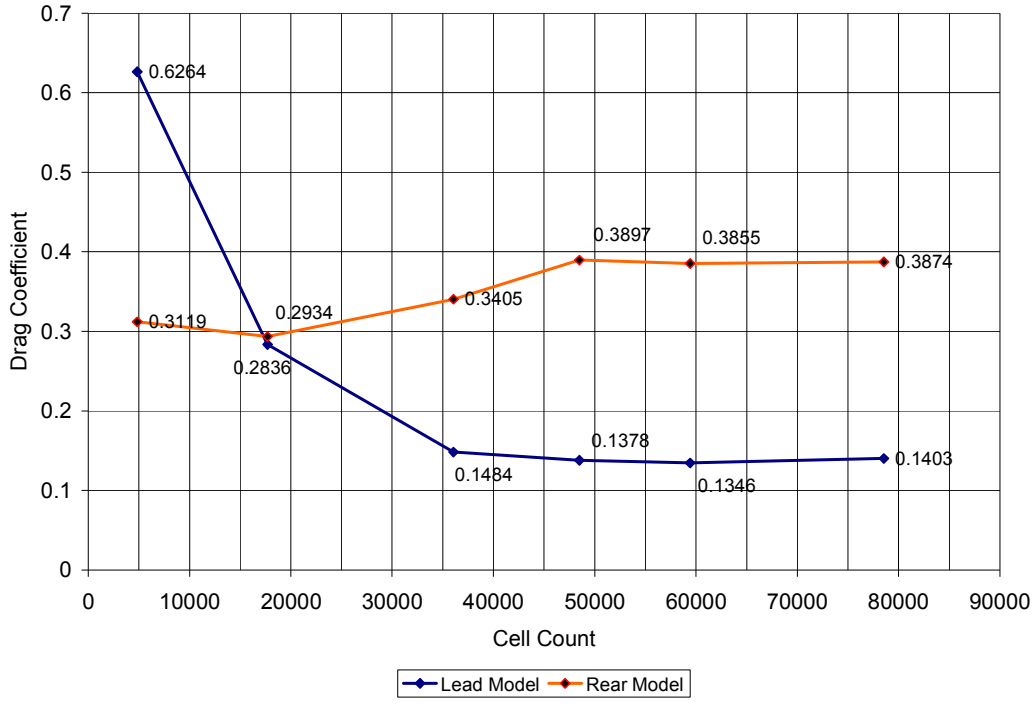

26 (b)

Figure 26(a). *Domain arrangement for 2D analysis of two models in tandem* ***(b).*** *Grid independency test for drafting arrangement for two 30 rear slant configurations of Ahmed models at x/L=1*

2.3.2 Three Dimensional (3D) Model Meshing

As an initial stage the computational results are required to be validated with the available experimental and literature data. In-order to accomplish this task, to study the effects of platooning on vehicle aerodynamics, a systematic procedure for analyzing the aerodynamic behaviour is followed starting from 2D analysis to 3D analysis. Isolated models are validated initially before studying the effects of vehicle platooning. Since, meshing plays a very important role in the final solution, a careful selection of meshing has to be made, before extending the study with the same type of meshing to all the cases (from an isolated case to six models platooning case) Hence, initially isolated models are validated, and once the validation is accomplished the same meshing technique is extended to all other cases.

To mesh a 3D model in gambit, the model can be either created in GAMBIT or can be imported from other CAD packages. For the current study, solid models of Ahmed car model are created using the commercial CAD package, Solid Works 2003. The model is saved as *.IGS files and imported to GAMBIT for meshing. A standard unstructured meshing technique using tetrahedral cells is followed owing to the complex curvilinear geometry at the front of the model and extended to the entire domain using size functions. The same technique is followed for all other cases that are discussed below.

2.3.2.1 Isolated Model

The isolated Ahmed car model is analyzed for its various rear slant angle geometry ranging from (0˚-40˚). A three dimensional view of the Ahmed model with its variable rear slant angle configuration is shown in the figure 27 below.

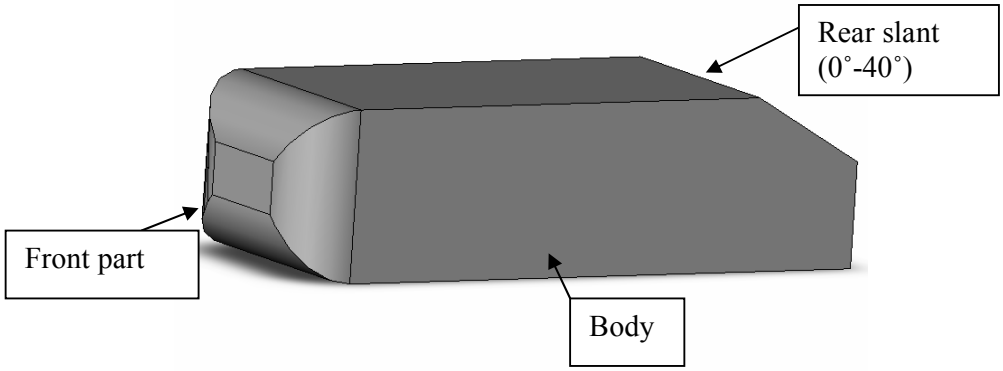

Figure 27. *Ahmed car model with variable rear slant geometry*

The concept of symmetry is applied for performing the CFD simulations for isolated Ahmed models owing to its symmetrical geometry along its length. The figure 28 shows the concept of symmetry and the procedure followed for creating the meshes.

Unstructured meshing technique is followed owing to the complex curvilinear geometry at the front of the model. A four layer triangular boundary layer elements are created to capture the boundary layer resolution and more accurate predictions on the separation of flow at the rear slant angle (especially at a critical angle of 30˚).

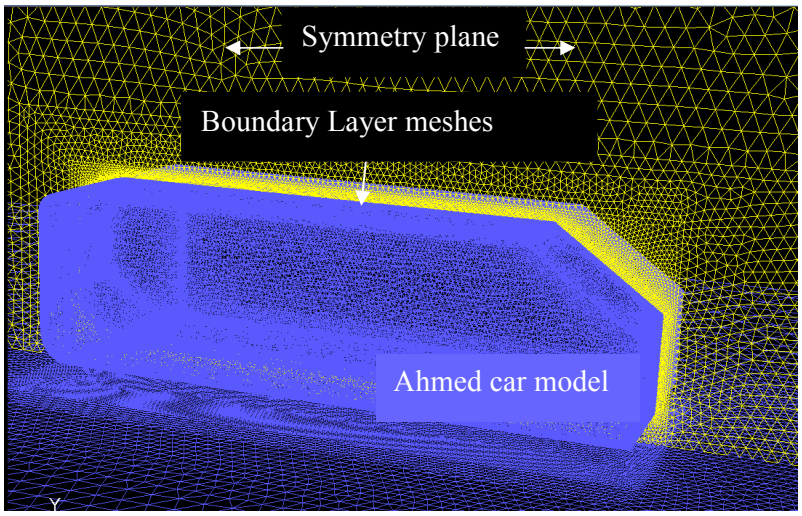

Figure 28. *Concept of symmetry followed for isolated Ahmed car models*

The entire domain encloses nine sub domains enclosing approximately 1.8 million tetrahedral cells. The domain is created in such a way that the inlet, out let, sides and ceiling are placed far away that it does not affect the flow predictions. Two sub domains are created surrounding the Ahmed car model, the smaller domain (Interior 1) just surrounding the model is created to have extremely fine meshes of four layers to record the boundary layer flow behaviour, the separations from the rear slant and also to achieve respectable wall y+ range. The facet averaged y+ value was 54.1706, which is within the limits for Realizable k – ε turbulence model. About half a million cells are enclosed in this domain. The second sub domain which immediately surrounds the smaller domain, (interior 2) have finer tetrahedral elements to record the strong vortices beginning to develop approximately at 12.5˚- 30˚ (High drag regime after Jhonson et.al. (2004)) rear slant angle and to predict the quasi-static two dimensional vortices formed at the base. The outer sub domain 2 contains 4 volumes with approximately half a million tetrahedral cells, and finally the outermost sub domain 3 consists four volumes with approximately 800,000 tetrahedral cells. The increase in mesh sizes from the model to the outermost domain is carried out by using the size function option available in the GAMBIT software [GAMBIT user manual].

2.3.2.2 Two Models in Tandem

The effect on the presence of upstream vehicle is analyzed by having two Ahmed car models in tandem with 30˚ rear slant angle. Two different cases are performed with two model platoon analysis.

i. Two 100% scales of Ahmed model in tandem and
ii. Two different scales of Ahmed model in tandem (lead model - 75% scale model and trailing model - 100% scale model).

The inter vehicle spacing is varied for the above cases between 0.125L to 4L and 0.25L to 2 L respectively, where L is the length of the 100% scale Ahmed model, (L= 1.044m). The reason for using 30˚ rear slant angle model is; experimental results are available for both the cases mentioned above. Also, this validation would enable to further extend the research to analyze the effects on 3 and 6 model platoons computationally.

2.3.2.2.1 Two 100% scale models in tandem

The domain inlet is positioned approximately 5 times the length of the model to ensure that the flow is fully developed before it reaches the model. The outlet is positioned extremely far 15 times the length of the model from the rear of the trailing model, allowing the wake flow to be completely recorded. The sides of the test domain are positioned approximately twice the length of the Ahmed model from each sides of the model, to ensure that it does not disturb the flow around the model and the ceiling is positioned approximately thrice the length of the Ahmed model from its top surface for the same reason. The model is set at 0.05m from the ground, as it is the standard ground clearance recommended, after Ahmed et.al. (1984). The model setup and domain information are indicated in the figure 29.

The mesh generation for the two model platoon is not identical to that of an isolated model, though the same unstructured tetrahedral cells are used for grid generation. The reason is, since in an isolated model the concept of symmetry was able to be used, thereby more mesh concentration were able to be set around the

model. The same concept cannot be extended to the two model platoon owing to the loss of information along the symmetry plane (e.g. vortex interaction between the models would be lost) and more over, if the same concept of meshing is followed the cell counts would be more than 2.6 million since full models are used and the current computational power is not adequate to run such simulations.

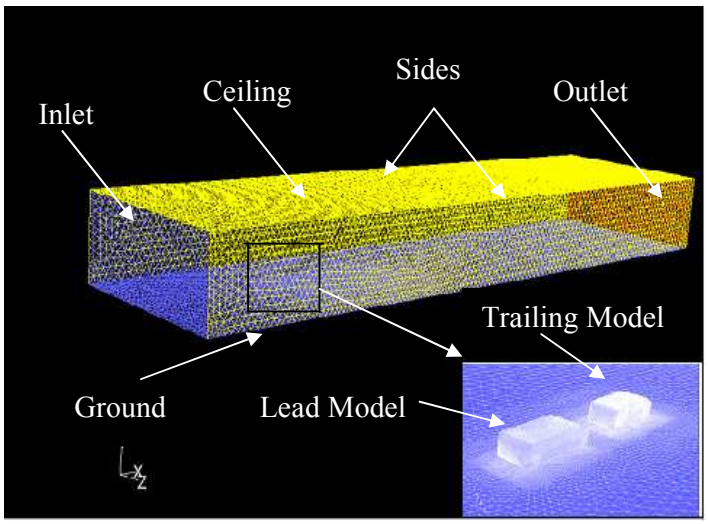

Figure 29. *Domain information for two 100% scale Ahmed models*

Since the forces have to be measured in both the models, fine meshes of unstructured tetrahedral cells are created around the Ahmed models and the region in between both the models for critical spacing lengths, which is in between 0.125L and 1L . The important flow structures to be recorded apart form the 'C' pillar vortices are the vortex interactions between the models, as they are the primary source of increase in drag coefficients of vehicles when traveling in close proximity, the pressure recovery of the lead model at close proximity, the direct reattachment of flow on the trailing model at close proximity and the velocity deficit in the wake of both the lead and the trailing model. Hence, a smaller domain enclosing both the models is created (for 0.125L to 1L inter-vehicle spacing cases) and is meshed using finer tetrahedral cells. The rest of the domain is meshed with coarser grid which is accomplished through the use of size functions. Grid independence was achieved after approximately 1.75 million cells for 0.125L inter-vehicle spacing and the same is extended to other spacing lengths.

2.3.2.2.2 Two different scales of models in tandem

Two different scales of Ahmed models are used to study the effects of two model platooning. The Ahmed models used are of 30˚ rear slant angle models. A 75% scale model is used as the lead model and the 100% scale model is used as the trailing model. The domain arrangement was very much similar to the two 100% scale test but for the ground clearance for the 75% scale model is changed to 0.0375 when compared to 0.05m owing to the scaling effects. The domain arrangement of two different scales of Ahmed model in tandem is shown below in the figure 30.

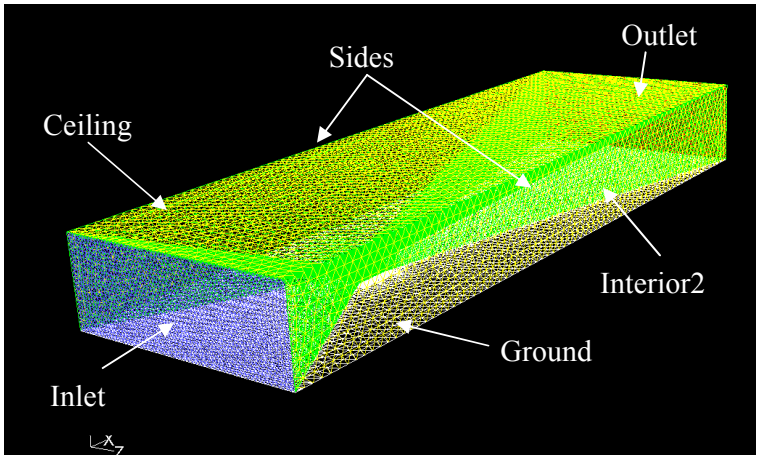

Figure 30. *Domain information of two different scales of Ahmed models*

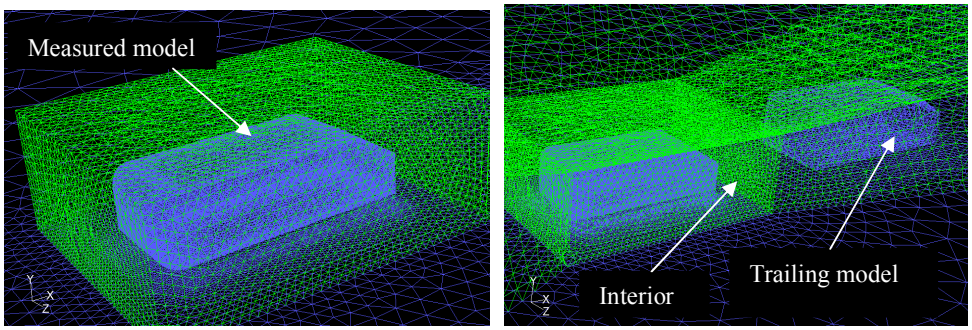

Figure 31. *Interior domains around the measure model*

The meshing strategy followed for the current case on two different scales of Ahmed models is more similar to the above case on 100% scale models. Here the forces are compared only on the lead model (owing to experimental inadequacy).

Therefore, the meshing was concentrated more on the lead model and the area enclosing both the models. As shown in figure 31 a smaller domain is created around the measure (lead model) model and very fine meshing is performed in this smaller domain, to record all the important features that create the coefficient of drag. The same unstructured tetrahedral meshing technique is used to mesh the models and their concentration is varied depending upon the requirement using size functions.

2.3.2.3 Three and Six models in Tandem

2.3.2.3.1 Three models in tandem

As a further analysis, the study is extended computationally to three and six models in tandem to understand the effects of platooning on aerodynamic drag coefficients of the intermediate/ measured model in the platoon. This is performed in order to understand the aerodynamics of longer platoons and, in particular, the aerodynamics of a single model in a long platoon.

Initially the cases are extended to a three model platoon, which is expected to be validated experimentally in order to give a strong understanding for extending the study to a six or an infinite platoon analysis. For the current case (25˚ and 35˚ rear slant angle) the pre critical and post critical rear slant angle configurations of the Ahmed car model are analyzed.

The domain arrangement is more similar to the previous analysis followed on two Ahmed car models, except for the fact that here the models used are 75% scaled models and the measure model in the intermediate model i.e. all the measurement on forces are measured with respect to this model in both CFD and experimental analysis. A smaller domain is created around the measured model and very fine meshing is carried on this domain to record the important features on the effects of vortex interactions from the lead model, rear separation regions and the pressure recovered at the model's base which contributes to its drag coefficient. The drafting arrangement and the measure model setup are shown in figures 32 & 33.

The inter-vehicle spacing is varied between 0.25L to 1L and unstructured tetrahedral meshing method is followed to mesh the entire domain and the area of concentration in varied by the use of size functions.

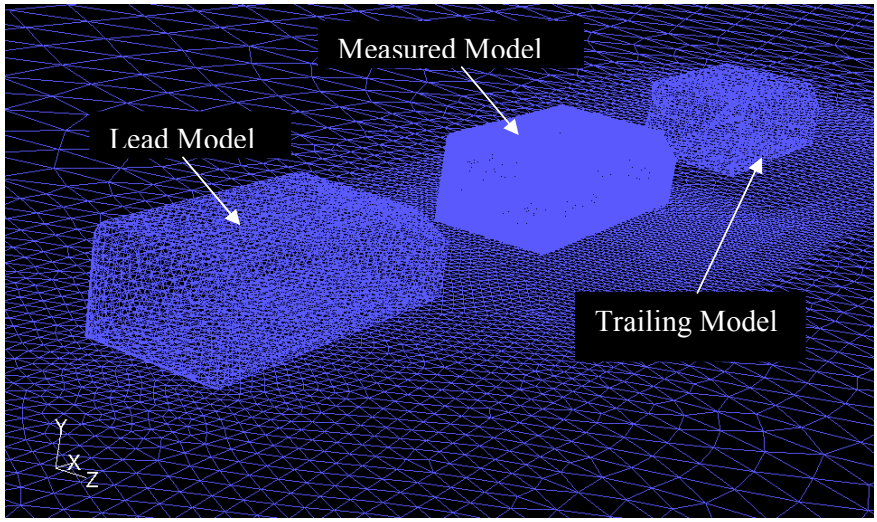

Figure 32. *Drafting arrangement of three models in tandem*

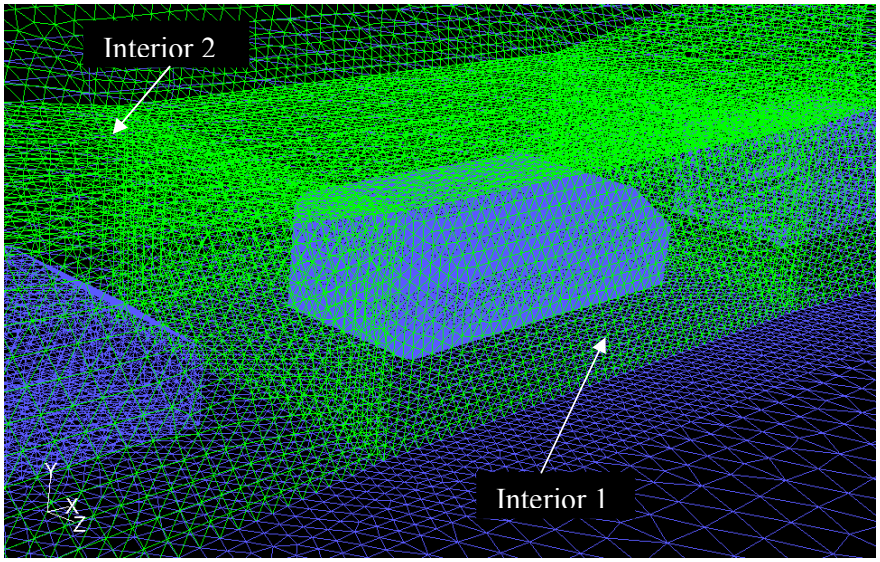

Figure 33. *Meshing around the measure/ intermediate model*

2.3.2.3.2 Six models in tandem

The current case employs six full (100%) scales of Ahmed models and the analysis is performed for rear slant angles between 0˚ and 40˚. Similar to previous cases discussed, six identical models (identical rear slant angles) are used and only the inter-vehicle spacing between the models are varied computationally. The domain information is identical to the previous cases studied except for the fact that the measured model is the 5th model from the domain inlet. The drafting arrangement of six model platoon is indicated below in the figure 34.

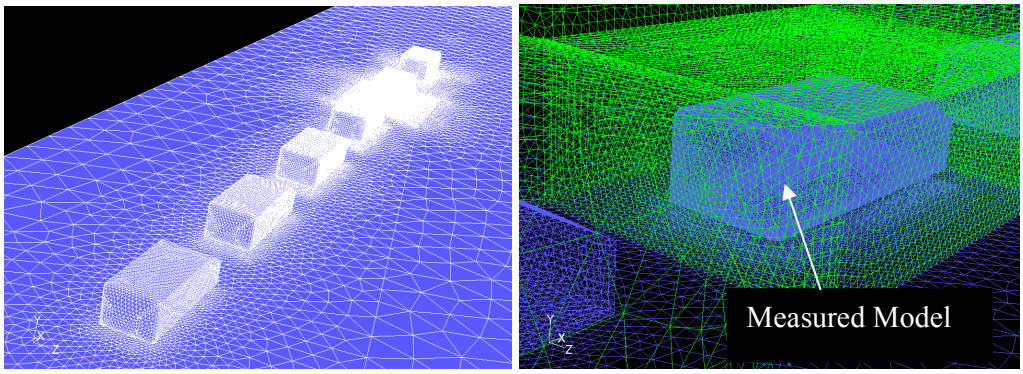

Figure 34. *Drafting arrangement of six model platoon and measure model arrangement*

A smaller domain is created around the 5th model from the inlet and very fine meshing is performed for this domain. The same mesh generation techniques as performed in the previous cases is employed (using tetrahedral cells) to mesh the entire domain, by varying the size functions accordingly to requirement. The cases are performed for an inter-vehicle spacing ranging from 0.25L to 6L and for all rear slant angle configurations ranging between 0˚ and 40˚ with increments of 5˚.

2.3.2.4 Additional study on Pickup Trucks (Ute's)

In order to validate the current meshing technique followed, the study is extended to predict the aerodynamic effects around an isolated pickup truck model computationally, see Appendix B. The main purpose of this study is to record the

critical flow regions and predict the aerodynamic drag values for two different cases shown in figures 35 and 36,

1. Pickup truck with a closed tub
2. Pickup truck with an opened tub

The pick up truck's overall dimension used for the study is a ¼ scaled model of Ford falcon 2004.EX , see Appendix B.

The model is created using Solid Works 2004 and is imported to GAMBIT as an *.IGS file for meshing. Because of the symmetrical shape of the model along its length and since the study is performed for an isolated model, the concept of symmetry (half model) is used for performing the CFD analysis.

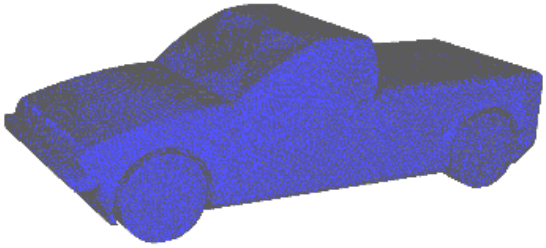

Figure 35. *Overall view of the pickup truck*

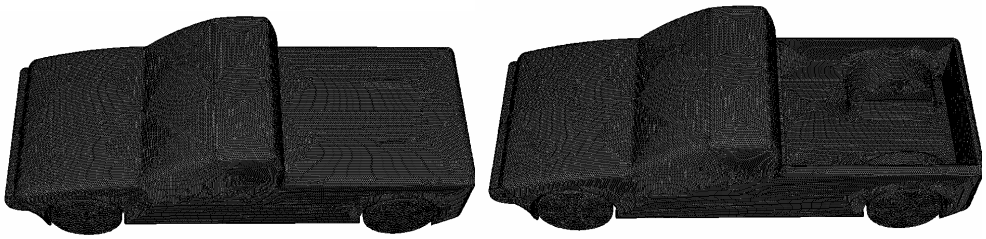

Figure 36. *Pickup truck with and without tonneau covers*

For the current study case the shape of the pickup truck is bluff i.e. it gives the basic flow patterns of a pickup truck, additional accessories like bull bar, rear view mirrors, roof-rails are not included. Also boat tailing is not performed for these models.

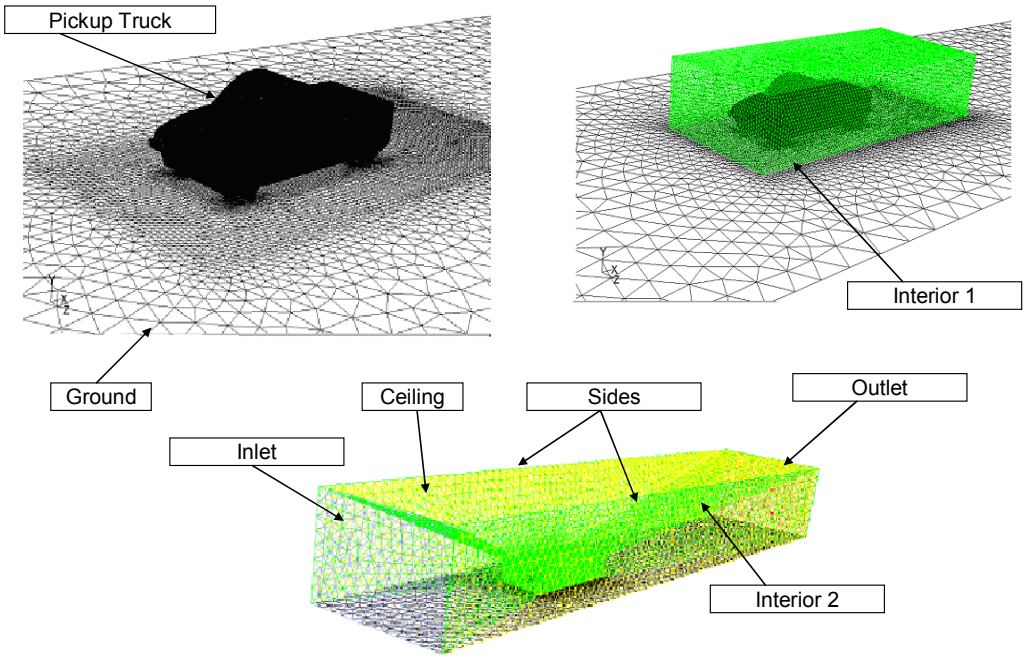

Figure 37. *Domain Information and construction for pickup trucks*

The domain shown in the figure 37 is created such that the inlet is positioned at 6L (L is the length of the model 1.556m) from the leading edge of the model, so that the flow is fully developed before it reaches the model. The outlet is positioned at 16L from the tailgate bumper of the model, in order to record the flow patterns and wake regions. The sides are positioned approximately 1.5L from the side of the model and the roof is positioned at 3L from the top of the cab portion. A small domain is created around the pickup tuck model for recording all the flow features including the critical separation regions. Unstructured tetrahedral cells are used to mesh the entire domain and very fine meshing is carried on in the interior domain which surrounds the pick up truck model as shown in figure 37, gradually the mesh size is increased towards the ends of the domain. The same procedure is followed for both the cases mentioned above.

2.4 CFD Simulations - using FLUENT (6.1.22)

This part of the chapter describes the general theory upon which the FLUENT algorithm is based for this particular numerical model. It includes a discussion about the governing partial differential equations, turbulence models, boundary conditions, and solution techniques.

2.4.1 Introduction

FLUENT is a computer software package developed to model fluid flow in a wide range of applications. Using this CFD package, the governing equations of fluid motion and the given boundary conditions can be discretized and solved for the velocity, temperature and pressure distributions throughout the domain.

FLUENT provides comprehensive modelling capabilities for a wide range of incompressible and compressible, laminar and turbulent fluid flow problems. Steady state or transient analyses can be performed. In FLUENT, a broad range of mathematical models for transport phenomena (like heat transfer and chemical reactions) is combined with the ability to model complex geometries. Examples of FLUENT applications include external aerodynamics study on ground vehicles; conjugate heat transfer in automotive engine components; laminar non-Newtonian flows in process equipment; pulverized coal combustion in utility boilers; flow through compressors, pumps, and fans; and multiphase flows in bubble columns and fluidized beds.

Robust and accurate turbulence models are a vital component of the FLUENT suite of models. The turbulence models provided have a broad range of applicability, and they include the effects of other physical phenomena, such as buoyancy and compressibility. Particular care has been devoted to addressing issues of near-wall accuracy via the use of extended wall functions and zonal models.

2.4.2 Basic Governing Equations

For all flows, **FLUENT** solves conservation equations for mass and momentum. For flows involving heat transfer or compressibility, an additional equation for energy conservation is solved. Additional transport equations are also solved when the flow is turbulent.

The equation for conservation of mass, or continuity equation, can be written as follows:

$$\frac{\partial \rho}{\partial t} + \nabla \cdot (\rho \vec{u}) = S_m \qquad (4.2.1)$$

Equation 4.2.1 is the general form of the mass conservation equation and is valid for incompressible as well as compressible flows. The ρ, t, and u represent the flow density, time, and velocity, respectively. The source S_m is the mass added to the continuous phase from the dispersed second phase (e.g., due to vaporization of liquid droplets) and any user-defined sources. In our application, S_m is zero.

The equation for conservation of momentum can be written as follows:

$$\frac{\partial}{\partial t}(\rho \vec{u}) + \nabla \cdot (\rho \vec{u}\vec{u}) = -\nabla p + \nabla \cdot (\Gamma) + \vec{F} \qquad (4.2.2)$$

where p is the static pressure, Γ is the stress tensor, and $\vec{F}$ is the gravitational body force and external body forces (e.g., that arise from interaction with the dispersed phase), respectively. $\vec{F}$ also contains other model-dependent source terms such as porous-media and user-defined sources.

The stress tensor Γ is given by

$$\Gamma = \mu \left[\left(\nabla \vec{u} + \nabla \vec{u}^{T} \right) - \frac{2}{3} \nabla \cdot \vec{u} I \right] \qquad (4.2.3)$$

where μ is the molecular viscosity, I is the unit tensor, and the second term on the right hand side is the effect of volume dilation.

2.4.3 Turbulence Models

Due to the high mass flow rate and complex flow patterns associated with platoon study, the flow is deemed to be turbulent. The basic governing equations described earlier are only suitable to describe a laminar flow unless DNS is being used. Turbulence can be characterized as a three dimensional, time-dependent, chaotic, random and dissipative flow. In a turbulent flow, there exists an energy cascade corresponding to a wide range of length scales from largest eddies (anisotropic integral length scales) to smallest eddies (isotropic Kolmogorov length scales). By using dimensional analysis, it is known that in order to capture length scales it needs a computational mesh with spatial grids in order of $\boldsymbol{O}$ ($\mathrm{Re}^{9/4}$) and time steps in order of $\boldsymbol{O}$ ($\mathrm{Re}^{3/4}$). Therefore, the direct numerical simulation (DNS) of a turbulent flow with a high Reynolds number to simulate a wide range of platoon combination is practically impossible with today's computer capacity.

Turbulent flows are characterized by fluctuating velocity fields. These fluctuations mix transported quantities such as momentum, energy, and species concentration, and cause the transported quantities to fluctuate as well. Since these fluctuations can be of small scale and high frequency, they are too computationally expensive to simulate directly in practical engineering calculations. Instead, the instantaneous (exact) governing equations can be time-averaged, ensemble-averaged, or otherwise manipulated to remove the small scales, resulting in a modified set of equations that are computationally less expensive to solve. However, the modified equations contain additional unknown variables, and turbulence models are needed to determine these variables in terms of known quantities.

For most engineering applications, the time-averaged or spatial filtered properties of the flow are of interest, thus the time-averaged transport equations, such as the Reynolds-averaged Navier-Stokes (RANS) equations, are established. However, time-averaged equations are unfortunately not closed and thus additional closure methods corresponding to different turbulence models have to be developed.

2.4.3.1 The Standard k- ε Model

The standard *k*- ε model is a semi-empirical model based on model transport equations for the turbulence kinetic energy (*k*) and its dissipation rate (ε). The model transport equation for *k* is derived from the exact equation, while the model transport equation for ε was obtained using physical reasoning and bears little resemblance to its mathematically exact counterpart.

The turbulence kinetic energy, *k*, and its rate of dissipation, ε are obtained from the following transport equations as

$$\frac{\partial}{\partial t}(\rho k) + \frac{\partial}{\partial x_i}\rho k u_i = \frac{\partial}{\partial x_j}\left[\left(\mu + \frac{\mu_t}{\sigma_k}\right)\frac{\partial k}{\partial x_j}\right] + G_k - \rho\varepsilon + S_k \qquad (4.3.1)$$

and

$$\frac{\partial}{\partial t}(\rho\varepsilon) + \frac{\partial}{\partial x_i}(\rho\varepsilon u_i) = \frac{\partial}{\partial x_j}\left[\left(\mu + \frac{\mu_t}{\sigma_\varepsilon}\right)\frac{\partial \varepsilon}{\partial x_j}\right] + C_{1\varepsilon}\frac{\varepsilon}{k}G_k - C_{2\varepsilon}\rho\frac{\varepsilon^2}{k} + S_\varepsilon \qquad (4.3.2)$$

In these equations, G_k represents the generation of turbulence kinetic energy due to the mean velocity gradients. $C_{1\varepsilon}$, $C_{2\varepsilon}$, and $C_{3\varepsilon}$ are constants. σ_k, and σ_ε are the turbulent Prandtl numbers for *k* and ε, respectively. S_k and S_ε are user-defined source terms.

The turbulent (or eddy) viscosity, μ_t, is computed by combining *k* and ε as follows:

$$\mu_t = \rho C_\mu \frac{k^2}{\varepsilon} \qquad (4.3.3)$$

where C_μ is a constant.

The model constants $C_{1\varepsilon}$, $C_{2\varepsilon}$, C_{μ}, σ_{k}, and σ_{ε} have the following default values:

Table 1. Default values of the standard *k*- ε model constants

Model constant	Default values
$C_{1\varepsilon}$	1.44
$C_{2\varepsilon}$	1.92
C_{μ}	0.09
σ_{k}	1.0
σ_{ε}	1.3

These default values have been determined from experiments with air and water for fundamental turbulent shear flows including homogeneous shear flows and decaying isotropic grid turbulence. They have been found to work fairly well for a wide range of wall-bounded and free shear flows.

The boundary conditions for solving the equations of standard *k*- ε model are summarized in Table 2 (Launder and Spalding, 1974).

Table 2. *Boundary conditions of standard k- ε model*

Boundary Types	**Boundary conditions**
Inlet:	Given k and ε
Outlet:	$\partial k / \partial n = 0$ and $\partial \varepsilon / \partial n = 0$
Free stream:	$k = 0$ and $\varepsilon = 0$
Solid walls: • $y^{*}>11.225$	Standard wall functions $u^{*} = \frac{1}{K}\ln(Ey^{*})$ where $u^{*} \equiv \frac{u_P C_{\mu}^{1/4} k_P^{1/2}}{\tau_w / \rho}$ $y^{*} \equiv \frac{\rho C_{\mu}^{1/4} k_P^{1/2} y_P}{\mu}$

	u_P is the mean velocity at point P near the wall $u_\tau = \sqrt{\tau_w / \rho}$ is the friction velocity y_P is the distance from point P to the wall *K* is Von Karman constant (0.42) *E* is the wall roughness k_P is the turbulent kinetic energy at point P $\varepsilon_P = \frac{C_\mu^{3/4} k_P^{3/2}}{K y_P}$
• $y^* < 11.225$ At wall-adjacent cells	$u^* = y^*$

2.4.3.2 The RNG k- ε Model

The RNG-based *k*- ε turbulence model is derived from the instantaneous Navier-Stokes equations, using a mathematical technique called ``renormalization group" (RNG) methods (D.Choudhry, 1993). The analytical derivation results in a model with constants different from those in the standard *k*- ε model, and additional terms and functions in the transport equations for *k* and ε.

The RNG k- ε model has a similar form to the standard k- ε model:

$$\frac{\partial}{\partial t}(\rho k) + \frac{\partial}{\partial x_i}\rho k u_i = \frac{\partial}{\partial x_j}\left[\sigma_k \mu_{eff} \frac{\partial k}{\partial x_j}\right] + G_k - \rho\varepsilon + S_k \qquad (4.3.4)$$

and

$$\frac{\partial}{\partial t}(\rho\varepsilon)+\frac{\partial}{\partial x_i}(\rho\varepsilon u_i)=\frac{\partial}{\partial x_j}\left[\sigma_\varepsilon\mu_{eff}\frac{\partial\varepsilon}{\partial x_j}\right] + C_{1\varepsilon}\frac{\varepsilon}{k}G_k - C_{2\varepsilon}\rho\frac{\varepsilon^2}{k} - R_\varepsilon + S_\varepsilon \tag{4.3.5}$$

In these equations, G_k represents the generation of turbulent kinetic energy due to the mean velocity gradients. The quantities σ_k and σ_ε are the inverse effective Prandtl numbers for k and ε, respectively. S_k and S_ε are user-defined source terms. The main difference between the RNG and standard k- ε models lies in the additional term in the ε equation given by

$$R_\varepsilon=\frac{C_\mu\rho\eta^3(1-\eta/\eta_0)}{1+\beta\eta^3}\frac{\varepsilon^2}{k} \tag{4.3.6}$$

where, $\eta_0=4.38$, $\beta=0.012$ and $\eta\equiv\frac{Sk}{\varepsilon}$.

The scale elimination procedure in RNG theory results in a differential equation for turbulent viscosity:

$$d\left(\frac{\rho^2 k}{\sqrt{\varepsilon\mu_t}}\right)=1.72\frac{\hat{\nu}}{\sqrt{\hat{\nu}^3-1+C_\nu}}d\hat{\nu} \tag{4.3.7}$$

where

$$\hat{\nu}=\mu_{eff}/\mu \qquad \text{and} \qquad C_\nu\approx 100$$

Equation 4.3.7 is integrated to obtain an accurate description of how the effective turbulent transport varies with the effective Reynolds number (or eddy scale), allowing the model to better handle low-Reynolds-number and near-wall flows.

In the high-Reynolds-number limit, Equation 4.3.7 gives

$$\mu_t = \rho C_\mu \frac{k^2}{\varepsilon} \qquad (4.3.8)$$

with C_μ=0.0845, derived using RNG theory. It is interesting to note that this value of C_μ is very close to the empirically determined value of 0.09 used in the standard *k*- ε model.

The model constants $C_{1\varepsilon}$ and $C_{2\varepsilon}$ in Equation 4.3.5 have values derived analytically by the RNG theory. These values are

$$C_{1\varepsilon} = 1.42,\ C_{2\varepsilon} = 1.68$$

2.4.3.3 The Realizable k- ε Model

In addition to the standard and RNG-based k-ε models described above, FLUENT also provides the so-called realizable k-ε model. The term ``realizable" means that the model satisfies certain mathematical constraints on the normal stresses, consistent with the physics of turbulent flows. To understand this, consider combining the Boussinesq relationship and the eddy viscosity definition to obtain the following expression for the normal Reynolds stress in an incompressible strained mean flow (T.H.Shih, et. al. 1995):

$$\overline{u^2} = \frac{2}{3}k - 2\nu_t \frac{\partial U}{\partial x} \qquad (4.3.9)$$

Using Equation 4.3.9 for $\nu_t \equiv \mu_t / \rho$, one obtains the result that the normal stress, $\overline{u^2}$, which by definition is a positive quantity, becomes negative, i.e., ``non-realizable", when the strain is large enough to satisfy.

$$\frac{k}{\varepsilon}\frac{\partial U}{\partial x} > \frac{1}{3C_\mu} \approx 3.7 \qquad (4.3.10)$$

Similarly, it can also be shown that the Schwarz inequality for shear stresses ($\overline{u_\alpha u_\beta}^2 \le \overline{u_\alpha^2 u_\beta^2}$; no summation over α and β) can be violated when the mean strain rate is large. The most straightforward way to ensure the realizability (positivity of normal stresses and Schwarz inequality for shear stresses) is to make C_μ variable by sensitizing it to the mean flow (mean deformation) and the turbulence (k, ε). The notion of variable C_μ is suggested by many modelers including Reynolds, and is well substantiated by experimental evidence. For example, C_μ is found to be around 0.09 in the inertial sub layer of equilibrium boundary layers, and 0.05 in a strong homogeneous shear flow.

Another drawback of the standard *k*- ε model or other traditional *k*- ε models lies with the modeled equation for the dissipation rate (ε). The well-known round-jet anomaly (named based on the finding that the spreading rate in planar jets is predicted reasonably well, but prediction of the spreading rate for axisymmetric jets is unexpectedly poor) is considered to be mainly due to the modeled dissipation equation.

The realizable *k*- ε model was intended to address these deficiencies of traditional *k*- ε models by adopting the following:

- A new eddy-viscosity formula involving a variable C_μ originally proposed by Reynolds;
- A new model equation for dissipation (ε) based on the dynamic equation of the mean-square vorticity fluctuation.

The modeled transport equations for *k* and ε in the realizable *k*- ε model are

$$\frac{\partial}{\partial t}(\rho k) + \frac{\partial}{\partial x_i}(\rho k u_j) = \frac{\partial}{\partial x_i}\left[\left(\mu + \frac{\mu_t}{\sigma_k}\right)\frac{\partial k}{\partial x_j}\right] + G_k + G_b - \rho\varepsilon + S_k \qquad (4.3.11)$$

and

$$\frac{\partial}{\partial t}(\rho\varepsilon)+\frac{\partial}{\partial x_i}(\rho\varepsilon u_j)=\frac{\partial}{\partial x_i}\left[\left(\mu+\frac{\mu_t}{\sigma_\varepsilon}\right)\frac{\partial\varepsilon}{\partial x_j}\right]+\rho C_1 S\varepsilon-\rho C_2\frac{\varepsilon^2}{k+\sqrt{\mu\varepsilon}}+C_{1\varepsilon}\frac{\varepsilon}{k}C_{3\varepsilon}G_b+S_\varepsilon \qquad (4.3.12)$$

where

$$C_1=\max\left[0.43,\frac{\eta}{\eta+5}\right]$$

and

$$\eta=S\frac{k}{\varepsilon}$$

In these equations, G_k represents the generation of turbulence kinetic energy due to the mean velocity gradient. G_b is the generation of turbulence kinetic energy due to buoyancy. $C_{1\varepsilon}$, $C_{2\varepsilon}$ and $C_{3\varepsilon}$ are constants. σ_k and σ_ε are the turbulent Prandtl numbers for k and ε, respectively. S_k and S_ε are user-defined source terms.

Note that the k equation is the same as that in the standard k- ε model and the RNG k- ε model, except for the model constants. However, the form of the ε equation is quite different from those in the standard and RNG-based k- ε models. One of the noteworthy features is that the production term in the ε equation (the second term on the right-hand side of Equation 4.3.12) does not involve the production of k; i.e., it does not contain the same G_k term as the other k- ε models. It is believed that the present form better represents the spectral energy transfer. Another desirable feature is that the destruction term (the next to last term on the right-hand side of Equation 4.3.12) does not have any singularity; i.e., its denominator never vanishes, even if k vanishes or becomes smaller than zero. This feature is contrasted with traditional k- ε models, which have a singularity due to k in the denominator.

This model has been extensively validated for a wide range of flows, including rotating homogeneous shear flows, free flows including jets and mixing

layers, channel and boundary layer flows, and separated flows. For all these cases, the performance of the model has been found to be substantially better than that of the standard *k*- ε model.

As in other *k*- ε models, the eddy viscosity is computed from

$$\mu_t = \rho C_\mu \frac{k^2}{\varepsilon}$$

The difference between the realizable *k*- ε model and the standard and RNG *k*- ε models is that C_μ is no longer constant. It is computed from

$$C_\mu = \frac{1}{A_O + A_S \dfrac{kU^*}{\varepsilon}} \tag{4.3.13}$$

where

$$U^* \equiv \sqrt{S_{ij}S_{ij} + \widetilde{\Omega}_{ij}\widetilde{\Omega}_{ij}} \tag{4.3.14}$$

and

$$\widetilde{\Omega}_{ij} = \Omega_{ij} - 2\varepsilon_{ijk}\omega_k$$

$$\Omega_{ij} = \overline{\Omega_{ij}} - \varepsilon_{ijk}\omega_k$$

where, $\overline{\Omega_{ij}}$ is the mean rate-of-rotation tensor viewed in a rotating reference frame with the angular velocity ω_k. The model constants A_0 and A_s are given by

$$A_O = 4.04, \qquad A_S = \sqrt{6}\cos\phi$$

where

$$\phi = \frac{1}{3}\cos^{-1}(\sqrt{6}W), \qquad W = \frac{S_{ij}S_{jk}S_{ki}}{\widetilde{S}}, \qquad \widetilde{S} = \sqrt{S_{ij}S_{ij}}, \qquad S_{ij} = \frac{1}{2}\left(\frac{\partial u_i}{\partial x_j} + \frac{\partial u_j}{\partial x_i}\right)$$

It can be seen that C_μ is a function of the mean strain and rotation rates, the angular velocity of the system rotation, and the turbulence fields (k and ε). C_μ in Equation 4.3.13 can be shown to recover the standard value of 0.09 for an inertial sublayer in an equilibrium boundary layer.

The model constants C_2, σ_k, and σ_ε have been established to ensure that the model performs well for certain canonical flows. The model constants are listed in table 3.

Table 3. *The default values of the realizable k- ε model constants*

Model constant	Default values
$C_{1\varepsilon}$	1.44
C_2	1.9
$\sigma_{k,}$	1.0
σ_ε	1.2

As a result, in this investigation, the realizable *k*- ε model is selected to be the turbulence model for its prediction of flow separations.

2.4.4 Discretization

FLUENT uses a control-volume-based technique to convert the governing equations to algebraic equations that can be solved numerically. This control volume technique consists of integrating the governing equations about each control volume, yielding discrete equations that conserve each quantity on a control-volume basis.

The finite volume discretisation of the governing equations in time and space is described here. The numerical scheme is fully implicit and can accommodate both structured and unstructured grids with cells of arbitrary topology. The numerical implementation of the initial and the wall boundary conditions is also explained.

The segregated approach is used to solve the resulting set of coupled non-linear algebraic equation systems. This leads to a decoupled set of linear algebraic equations for each dependent variable. These equations are solved by an iterative

conjugate gradient solver, which retains the scarcity of the coefficient matrix, thus achieving the efficient use of computer resources.

2.4.5 Boundary Conditions

2.4.5.1 Velocity Inlet Boundary Condition

Velocity inlet boundary conditions are used to define the flow velocity, along with all relevant scalar properties of the flow, at flow inlets. The total (or stagnation) properties of the flow are not fixed, so they will rise to whatever value is necessary to provide the prescribed velocity distribution.

The values of velocity inlet boundary conditions in FLUENT are given in the table 4 below,

Table 4. *Velocity inlet boundary condition*

Properties	**Default values**	
Velocity Specification Method	Magnitude, Normal to Boundary	
Reference Frame	Absolute	
Velocity Magnitude (m/s)	**30**(or) **35**	Constant
Turbulence Specification Method	K and Epsilon	
Turb. Kinetic Energy (m^2/s^2)	1	Constant
Turb. Dissipation Rate	1	Constant

This boundary condition is intended for incompressible flows, and its use in compressible flows will lead to a nonphysical result because it allows stagnation conditions to float to any level. While assigning the boundary condition for velocity inlet, it should be noted that it is not positioned too close to the model, since this could cause the inflow stagnation properties to become highly non-uniform. Hence for the current case the inlet is positioned well ahead of the model so that the flow is fully developed before it reaches the model and the stagnation properties are not affected.

In the above table, the velocity magnitude is set as 35 m/s (depending on the model length) for analyzing isolated models and the drafting effects for two and six

100% scale Ahmed models in tandem. Also, the velocity magnitude is set as 30 m/s for analyzing the drafting effects on two different scales of Ahmed models and three Ahmed models in tandem.

2.4.5.2 Pressure Outlet Boundary Condition

Pressure outlet boundary conditions require the specification of a static (gauge) pressure at the outlet boundary. The value of static pressure specified is used only while the flow is subsonic. Should the flow become locally supersonic, the specified pressure is no longer used; pressure will be extrapolated from the flow in the interior. All other flow quantities are extrapolated from the interior.

A set of ``backflow'' conditions is also specified to be used if the flow reverses direction at the pressure outlet boundary during the solution process. Convergence difficulties will be minimized if you specify realistic values for the backflow quantities. The default values of pressure outlet boundary conditions in FLUENT are given in the table 5 below,

Table 5. *Pressure outlet boundary conditions*

Properties	**Default values**	
Gauge Pressure (pascal)	0	Constant
Back Flow Direction Specification Method	Normal to Boundary	
Turbulence Specification Method	K and Epsilon	
Backflow Turb. Kinetic Energy (m^2/s^2)	1	Constant
Backflow Turb. Dissipation Rate (m^2/s^2)	1	Constant

The above default values shown are used for the current study. The outlet is positioned sufficiently at a far distance from the model so that the rear wake region information is recorded and moreover the back flow is avoided.

2.4.5.3 Symmetry Boundary Condition

Symmetry boundary conditions are used when the physical geometry of interest, and the expected pattern of the flow/thermal solution, has mirror symmetry. They can also be used to model zero-shear slip walls (boundaries) in viscous flows

(C. Hinterberger et.al, 2004). Since the wall effects should be avoided to record more realistic effects of aerodynamics over vehicles the sides and the ceiling of the test domain is assigned symmetry boundary condition, where no wall effect is present. Also proper care must be taken to assign symmetry boundary conditions at proper locations. Even though the sides and the ceiling are assigned symmetry boundary conditions they are positioned sufficiently far so that the side flow which contributes to the development of 'C' Pillar vortices at the rear of the Ahmed models are recorded properly.

While analyzing an isolated Ahmed model, since the model is symmetrical along its length only half model is used for the CFD analysis. The centre plane which divides the model into two half's, is assigned symmetry boundary condition, since the flow would be symmetrical on both sides under steady state conditions. This saves considerable amount of time for meshing and running the CFD simulations.

2.4.5.4 Wall Boundary Condition

The Ahmed models and ground plane are assigned the no-slip wall boundary conditions. These conditions are used to bound fluid and solid regions. In viscous flows, the no-slip boundary condition is enforced at walls by default. The same is used for the current study on external aerodynamics. No modified effects are used i.e. default values are used and very fine meshes around the model are used to record the viscous effects.

2.4.5.5 Interior Boundary Condition

The Interior boundary conditions are assigned to the domains which surrounds the measure model in the platoon and which splits up the large domain into sub-domains. The faces that split up the larger domain are assigned interior boundary condition. Since the main purpose of splitting the domain is to impart different meshing strategy at different parts of domain and not to affect or obstruct the flow, and these boundary conditions does not affect the flow in any manner. Hence, for the current case the faces that divide the larger domain are assigned interior boundary conditions.

2.4.6 Material

The medium flowing through the system is air. The properties of air for this analysis are taken at an ambient temperature. Having a viscosity of $1.7894e^{-05}$ and density of 1.225 kg/m^3, for all the models involving energy calculations, they are assumed to be constant. Due to the high flow rates through the system and limited range in temperature, buoyancy driven flows due to density differences in the air are not significant. Hence, this assumption will have a minimal effect.

2.4.7 Solution Techniques

2.4.7.1 Under-Relaxation Factors

Because of the nonlinearity of the equation set being solved by FLUENT, it is necessary to control the change of primary variable (ϕ). This is typically achieved by under-relaxation, which reduces the change of ϕ produced during iteration. In a simple form, the new value of the variable ϕ within a cell depends upon the old value, ϕ_{old}, the computed change in ϕ, $\Delta\phi$, and the under-relaxation factor, α, as follows:

$$\phi = \phi_{old} + \alpha\Delta\phi$$

The default values of under-relaxation factors (α) in FLUENT are listed below.

Table 6. *Default values of α in FLUENT*

Properties	**Default values**
Pressure	0.3
Momentum	0.7
Turbulence Kinetic Energy	0.8
Turbulence Dissipation Rate	0.8
Turbulent Viscosity	1

Because the computational domain comprises very small gap between the model and the ground, a high velocity gradient persists at separation regions, it is important to reduce the values of α in order to get the result converged. In this

investigation, the value of α for pressure is reduced to 0.1 and momentum to 0.4. Later it was found that the change did not affect the final result on drag coefficient. Hence, the default values were used for the entire study.

2.4.7.2 Pressure Solution

The pressure interpolation schemes available in the FLUENT are listed:

- Standard
- Presto
- Linear
- Second order
- Body-force-weighted

The linear scheme uses an averaged pressure for the face value of the two adjacent cells. This is the most robust scheme; however, the performance of this scheme drops off when there are large local gradients in pressure. But, for this investigation the linear scheme is used as no large pressure gradients are involved, hence the current model is good enough to predict the pressure drop at the base of the Ahmed car model, which in turn in proportional to the drag coefficient of the model.

2.4.7.3 First order and second order upwind schemes

For the interpolation for all scalar variables except pressure in the governing equations, FLUENT provides a number of different schemes. The two options relevant to this work are first-order upwind and second-order upwind schemes.

When first-order accuracy is desired, quantities at cell faces are determined by assuming that the cell-centre values of any field variable represent a cell-average value and hold throughout the entire cell; the face quantities are identical to the cell quantities. Thus when first-order upwind scheme is selected, the face value ϕ_f is set equal to the cell-centre value of ϕ in the upstream cell.

When second-order accuracy is desired, quantities at cell faces are computed using a multidimensional linear reconstruction approach (T. J. Barth, and D.Jespersen, 1989). In this approach, higher-order accuracy is achieved at cell faces through a

Taylor series expansion of the cell-cantered solution about the cell centroid. Thus when second-order upwind scheme is selected, the face value ϕ_f is computed using the following expression:

$$\phi_f = \phi + \nabla\phi \cdot \Delta\vec{s}$$

where ϕ and $\nabla\phi$ are the cell-centered value and its gradient in the upstream cell, and $\Delta\vec{s}$ is the displacement vector from the upstream cell centroid to the face centroid. This formulation requires the determination of the gradient $\nabla\phi$ in each cell. This gradient is computed using the divergence theorem, which in discrete form is written as

$$\nabla\phi = \frac{1}{V}\sum_{f}^{N_{faces}} \tilde{\phi}_f \vec{A}$$

Here the face values $\tilde{\phi}_f$ are computed by averaging ϕ from the two cells adjacent to the face. Finally, the gradient $\nabla\phi$ is limited so that no new maxima or minima are introduced.

In using these schemes, when the flow regimes are aligned to the grid, the first-order upwind scheme gives comparable results to that of the higher order. However, when the flow is not aligned with the grid, thus increasing numerical discretization errors, the second-order upwind schemes give superior results. Hence, for the current study after few preliminary tests using first order schemes for isolated model, the second order upwind schemes are used more predominantly for the rest of the study on platooning on its superior solving capability.

2.4.7.4 Iteration Residual

The residual convergence value used in this investigation is 10^{-4}. Smaller residual value does not result in any noticeable change of the calculated results but required significantly more computation time.

3. Experimental Analysis

This section provides details of the equipment used in this investigation, along with experimental techniques applied during tests.

3.1 Equipment

3.1.1 RMIT Industrial Wind Tunnel (IWT)

All tests in this investigation were conducted in the RMIT Industrial Wind Tunnel (IWT), (see Figure 38 for schematic representation).

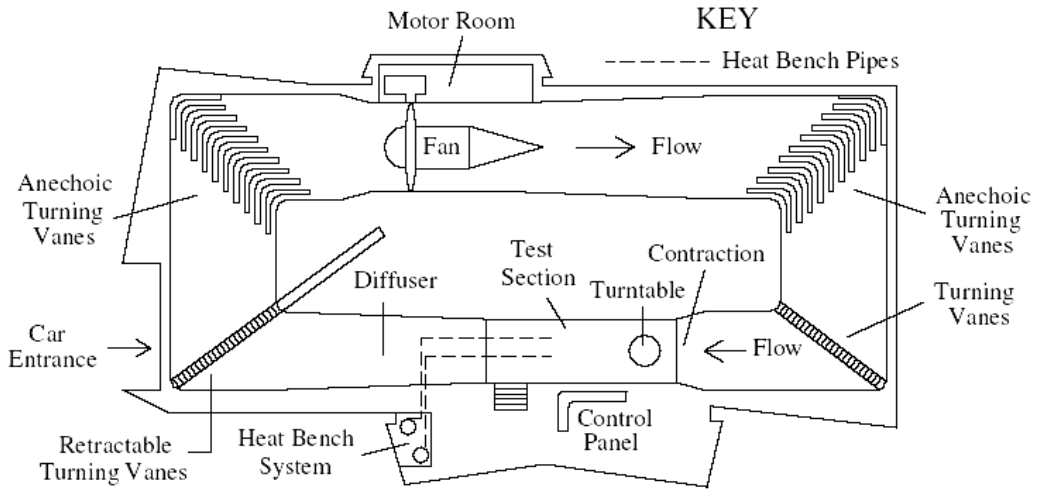

Figure 38. *Industrial Wind Tunnel (IWT) Layout, RMIT University*

The wind tunnel is a closed-jet and fixed-ground type, having a 2m high, 3m wide and 9m long test section. A single 7-blade fan of 5 m diameter drives the airflow through a 2:1 contraction, giving a maximum attainable speed of approximately 50 m/s at the test section inlet.

3.1.2 Test Model

For a detailed description of flow structures generated by the Ahmed model see section 1.3.1. Ahmed et.al. concluded that maximum drag was obtained at a base slant angle (α) of 30˚, before dropping as the backlight angle was further increased. As such, this configuration was termed 'critical'. In this critical arrangement, the model would generate a highly three dimensional wake, including a set of strong contra-rotating three-dimensional trailing vortices. Due to this inherent sensitivity in flow topology at 30˚ backlight angle, the same high drag configuration is used for this experimental investigation. The figure 39 below shows the test model in three-view form.

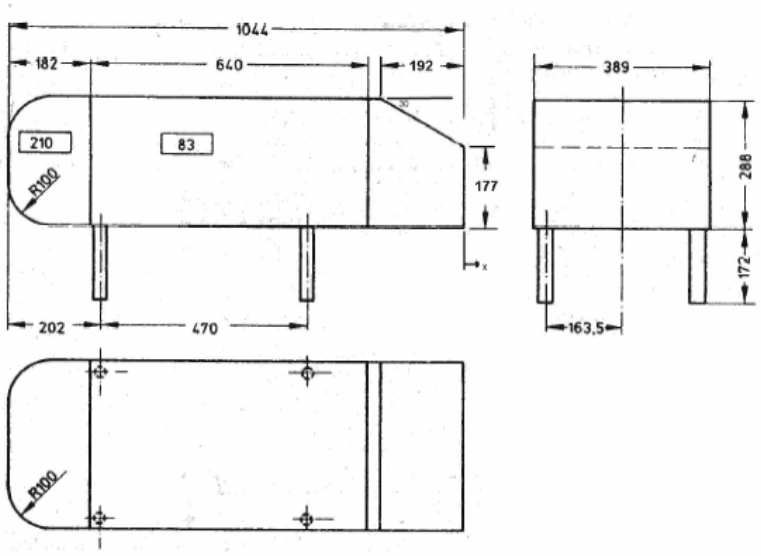

Figure 39. *Ahmed car model dimensional specifications, after Ahmed et.al.(1984)*

As shown in figure 39, the model is simply made up of three sections: the fore-section, which is rounded so that no separation occurs, the middle section, which is a simple rectangular cross-section with sharp edges, and the rear-portion that represents the backlight.

3.1.2.1 Model Positioning

Several studies have been conducted previously to investigate the influence of model position in a test section on the forces acting on the model. This is because of the influences of pressure gradients in the diffuser on a model's flow field and therefore body forces.

Garry et.al.(1994) investigated the influences of drag coefficients of a model when varied with the distance from the diffuser. They conducted tests on three crossed-jet wind tunnels and varied their test section proportions, which includes the aspect ration, area, length, and diffuser angle and contraction ratio. In their investigation they used a wide rage of test models of different sizes and shapes, to improve the generality of the data. They found a significant variation in drag coefficient when the model was positioned very near to the end of the test section.

The above variations in drag coefficients were attributed to the change of base pressures, which in-turn were caused either by the positive pressure gradients near the diffuser or the interference flows from below the raised ground planes with model wakes. Garry et.al.(1994) suggested that the base of the model should be positioned at least four times its cross sectional area from the end of the test section. Thus for the current study, the model was positioned approximately 2m, after the recommendation of Garry et.al.(1994).

3.1.2.2 Blockage

A 3x2m wind tunnel test section results in a solid model blockage ratio of 1.9%, based on maximum projected frontal area of the Ahmed model (100% scale model). This value was deemed insignificant in that relevant flow structures would not be notably affected by the presence of the wind tunnel walls. Hence blockage corrections were not applied for the current experimental analysis.

3.1.3 Force Balance

In order to find a correlation between flow structure and the forces exerted on the trailing model, time-averaged lift and drag measurements were taken at each model position. The force sensor used here was supplied by JR3, Inc. Data acquisition was performed with a DOS-based PC and communication between forces sensor, force receiver and PC was controlled via software written by JR3, Inc. A JR3 DSP-based force sensor receiver processed raw data transmitted from the force sensor. The force sensor and receiver system provided six degree of freedom force and moment measurements, with each channel sampling at a rate of 8 KHz. The raw data measured by the force sensor was passed through a decoupling matrix to avoid sensor cross coupling. The data was then low-pass filtered before the receiver calculated force and moment vector magnitudes.

Since the effects of drafting were of interest in this work, it was necessary to have a mobile model. As such, a force sensor was rigidly mounted inside the test model (lead, 75% scale model) and loads were transferred to the sensor via the supports that were mounted between the tunnel floor and force sensor. figure 40 shows the setup, after Pagliarella et.al (2005).

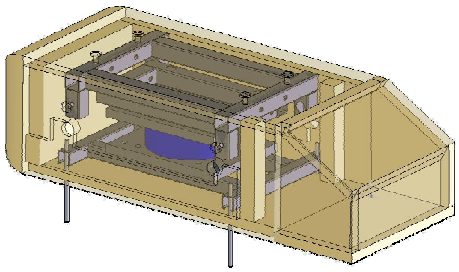

Figure 40. *Measure model setup after Pagliarella et.al.(2005)*

The JR3 force sensor used was supplied fully calibrated. However, a detailed calibration check was performed prior to testing in order to quantify the sensitivities and error ranges of each of the six load components, although emphasis was placed on lift and drag. Once the sensor was integrated with the model and mounted to the

tunnel floor via the supports, known loads were applied on the body, such that drag forces could be isolated. To isolate drag forces, known horizontal loads were applied via hanging masses with the aid of pulleys. figure 41 shown below summarizes the results obtained from the calibration check.

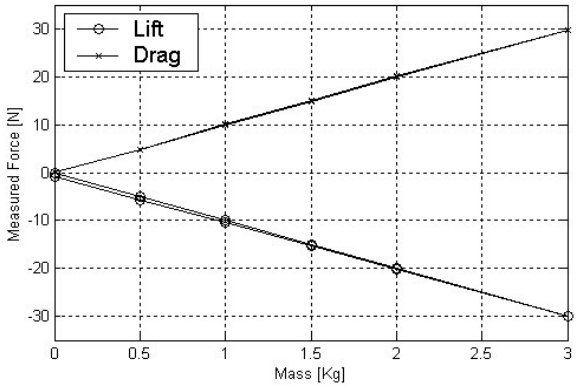

Figure 41. *JR3 force balance calibration check*

Linearity is evident throughout the loading range in both lift and drag. To assess errors associated with hysterysis, masses were gradually increased from zero to 3 kg and then decreased back to zero. The maximum error associated with repeatability and hysterysis was approximately ±2.1%, and occurred corresponds to a calibration load of 10N. However, for loads above 15N, maximum errors were below ±1.2%. Based on preliminary drag measurements of the Ahmed model, drag forces were in excess of 18N above test speeds of 30 m/s. A detailed description of the force balance specifications is given in Appendix A.

3.2 Experimental Setup

Figure 42 shows the experimental setup involving two different scales of Ahmed models in the RMIT - IWT.

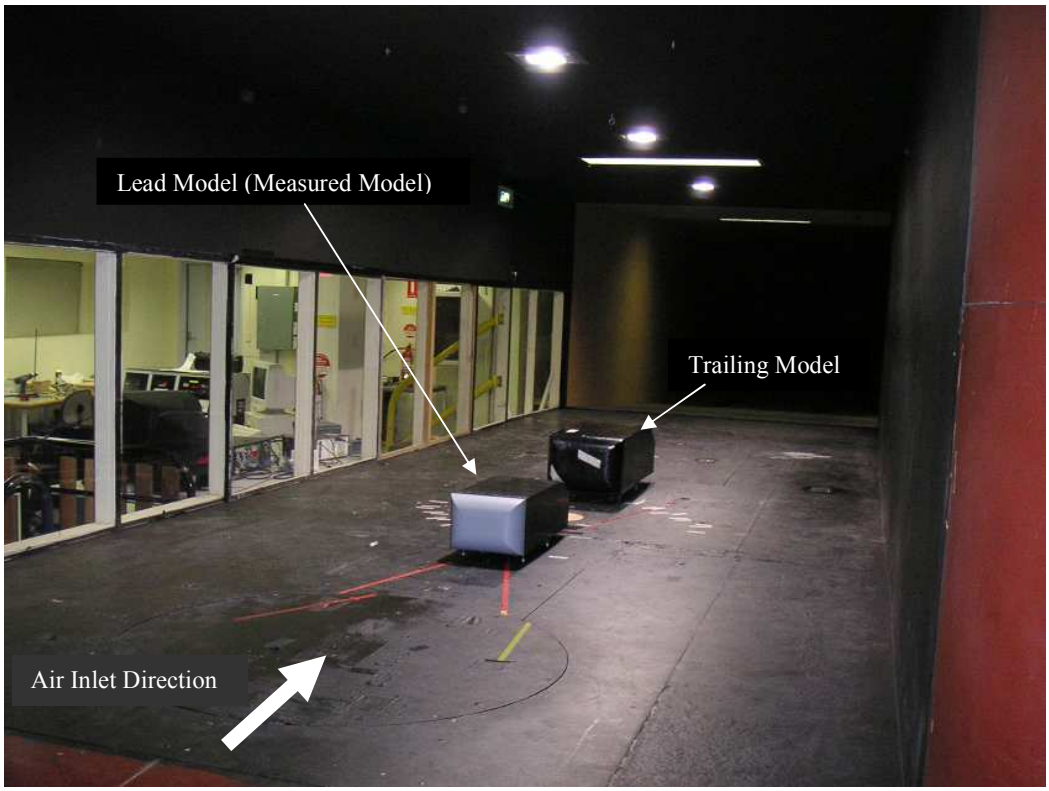

Figure 42. *Experimental setup for two scales of Ahmed models at RMIT Industrial Wind Tunnel (IWT)*

The two Ahmed models, a lead model (75% scale model) and a trailing model (100% scale model) with 30˚ rear slant angles, were positioned at different inter-vehicle spacing, which was varied with respect to the length of the 100% scale model (L= 1.044 m). The inter-vehicle spacing was varied between 0.25 and 2 L. The tests were carried out at the Industrial Wind Tunnel (IWT) in RMIT University and all the aerodynamic coefficients (only drag) are measured on the leading model. The effects of inter-vehicle spacing on drag coefficients are discussed in detail in this chapter.

3.3 Effects of Drafting

The influence of aerodynamic interference was investigated by introducing a second Ahmed model directly behind the test model, such that they assume a convoy or drafting arrangement. The spacing between the models was varied in order to encompass a range of possible on-road driving situations. Additionally these results

will be used to identify key aerodynamic interaction configurations for further investigation through detailed analysis of the flow structures.

After previous experiments performed by Vino and Watkins (2004) on two 100% scale Ahmed model with 30˚ rear slant angles, the current experimental analysis is extended to two different scales of Ahmed models with the same rear slant angles of 30˚. The lead model was a 75% scale Ahmed model and the rear model was a 100% scale Ahmed model. The experiments are carried on at a velocity of 30 m/s which corresponds to a model length-based Reynold's number of 1.55 x 10^6. Figure 43 shows the variation of drag coefficient of the leading Ahmed model with vehicle spacing. All data points were obtained from ensemble averages of several runs.

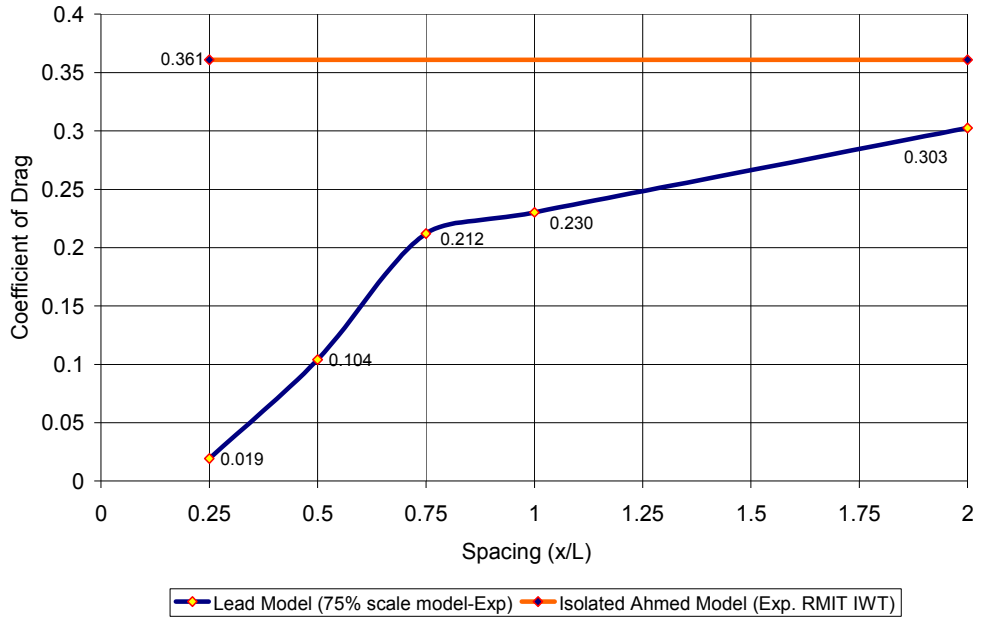

Figure 43. *Effects of drafting on drag coefficients using two different scales of Ahmed models*

3.3.1 Effects on Lead Model

Of the two models, all the forces could only be measured on the lead model. The reason for having the force balance in one model is the software's inadequacy to acquire data from both the models simultaneously i.e. interfacing two force balances, one on each model.

The presence of the rear model is reflected by the decreasing drag coefficient of the lead model with decrease in inter-vehicle spacing as shown in figure 43. At very close vehicle spacing of x/L=0.25, the drag coefficient of the lead model is about 95% less than that of an isolated model. The drag coefficient is 0.212 at x/L=0.75 and seem to become less sensitive to spacing after about x/L=0.75. It then increases gradually to 0.303 at x/L=2.

Within the region $0.25 < x/L < 2$, the drag of the lead model remains significantly lower than the isolated case. The main cause for this phenomenon is attributed to the increase in base pressure of the lead model which in turn is due to the presence of the trailing model in its wake. Horner (1965) found that the drag benefits experienced by the leading body of a cylinder-to-cylinder convoy are due to the presence of the trailing cylinder reducing the high-energy vortex street in the wake of the lead cylinder thus increasing base pressure. This 2-D cylinder arrangement is analogous to the convoy arrangement of the Ahmed models studied here in that both geometries are 'bluff' and will therefore generate some type of high-energy shedding phenomena.

The main source of drag for the Ahmed model geometry of 30° rear slant configuration is the pair of trailing vortices generated at the C-pillars. These vortices retain significant levels of kinetic energy and therefore significantly reduce the model's base pressure. At close inter-vehicle spacing, the strength of these C-pillar vortices of the lead model gets lower as the kinetic energy of these vortices are broken by the presence of the rear model in its wake. This ultimately increases the base pressure of the lead model and reduces its drag coefficient. As the inter-vehicle spacing increases gradually, the strength of these vortices of the lead model starts increasing i.e. these vortices slowly starts gaining their strength with higher kinetic energy levels. This effect reduces the model's base pressures and starts increasing their drag coefficients, which is evident from the increasing drag coefficient trend shown in Figure 43.

The presence of the trailing model is further explained by CFD techniques. A comparison of drag coefficients is made between the experimental and CFD results which can be seen from subsequent chapters.

4. CFD Results and Discussion

Even though the flow is highly three dimensional in the wake of an Ahmed model, 2D analysis is performed to obtain an initial understanding of the flow structures in the wake for different rear slant angles of isolated Ahmed model geometry. Hence, at the beginning of this chapter the results of 2D analysis performed on isolated Ahmed model shapes (in isolation) with rear slant angles ranging between 0˚ and 40˚, with 5˚ increment are discussed. It is then followed with the discussion of results on drafting two Ahmed models of 30˚ rear slant angles in order to understand the effects of drafting on the model's aerodynamic coefficients, which is one of the primary objectives of this research.

The 2D analysis is then followed by 3D analysis in an attempt to replicate more realistic flow structures of an Ahmed model. Similar to the procedure followed in 2D analysis, simulations are performed for isolated Ahmed models of different rear slant configurations ranging from 0˚ to 40˚ with a 5˚ increment. The flow structures and the influence of rear slant angles on drag coefficients of the Ahmed model observed in CFD are compared with the available experimental data after Ahmed et.al. (1984). The study is then extended to analyze the drafting effects on drag coefficients of models using two 100% scale Ahmed models and two different scales of Ahmed models. The 30˚ rear slant configuration is considered for both the cases mentioned above. The computational results are compared with the available experimental results and are discussed in this chapter.

Finally, with the available validations on the current CFD model, an attempt was made to provide useful source of data for the Future Generation Intelligent Transport Systems (FGITS). Thus the study was extended computationally to analyze the influences of inter-vehicle spacing on drag coefficients to a three model platoon and then to a six model platoon, (that was considered to represent the effects observed in an infinitely long platoon) and is discussed here. Also, as an additional study to check the effectiveness of the current CFD model in replicating complicated three dimensional flow structures of a more realistic vehicle shape, the results on the cases

performed over a pickup truck for various configurations and their corresponding influences on drag coefficients are discussed in Appendix B.

4.1 CFD Model Comparison

The accuracy of CFD analysis is driven largely by the quality of the physical models in the software and the ability of the software to closely match the true geometry of the physical item that we wish to model.

FLUENT provides a broad range of models (as discussed in Chapter 2), including:

- Incompressible or compressible flow
- A suite of turbulence models, including high and low Reynolds number

FLUENT features unstructured modeling technique which enables one to build mesh which wraps around curves, inclined planes, and other complex surfaces. It also offers the ability to fine-tune the computational mesh in areas of importance.

Although FLUENT provides reasonable accuracy of the physical flow behaviour, it still needs experimental results for proper validation. Hence the computational results are initially compared with the published experimental and computational data before any further extensions to study the effects of platooning is made. For the current research, the critical rear slant angle of 30˚, after S.R. Ahmed (1984) is used for validating the CFD results both for an isolated model case and the two models in tandem case, after Vino and Watkins (2004).

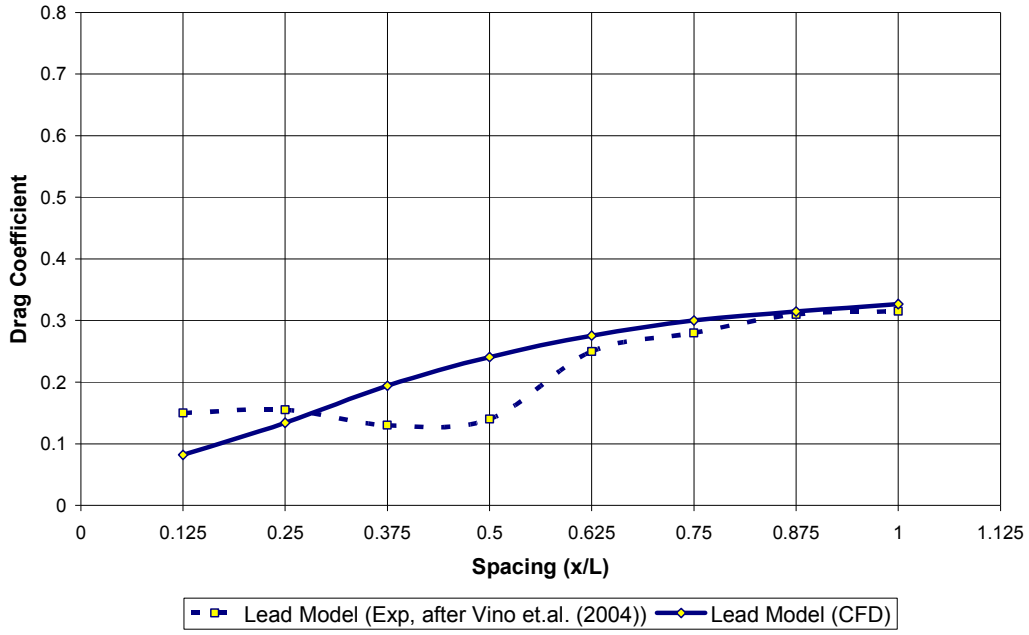

Figure 44. *Effects of inter-vehicle spacing on lead model - CFD & EFD comparison*

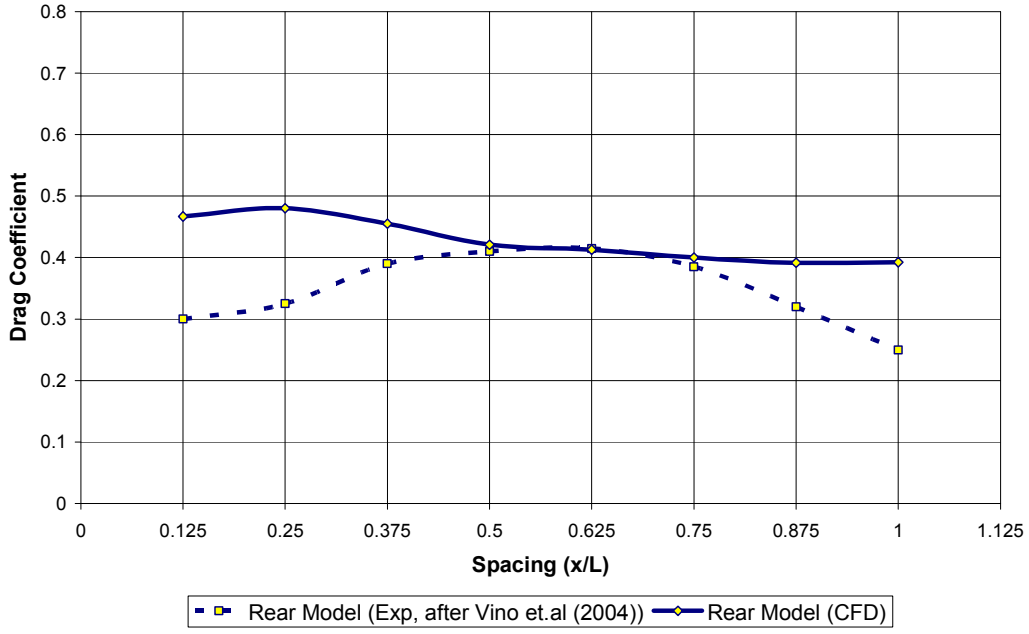

Figure 45. *Effects of inter-vehicle spacing on trailing model - CFD & EFD comparison*

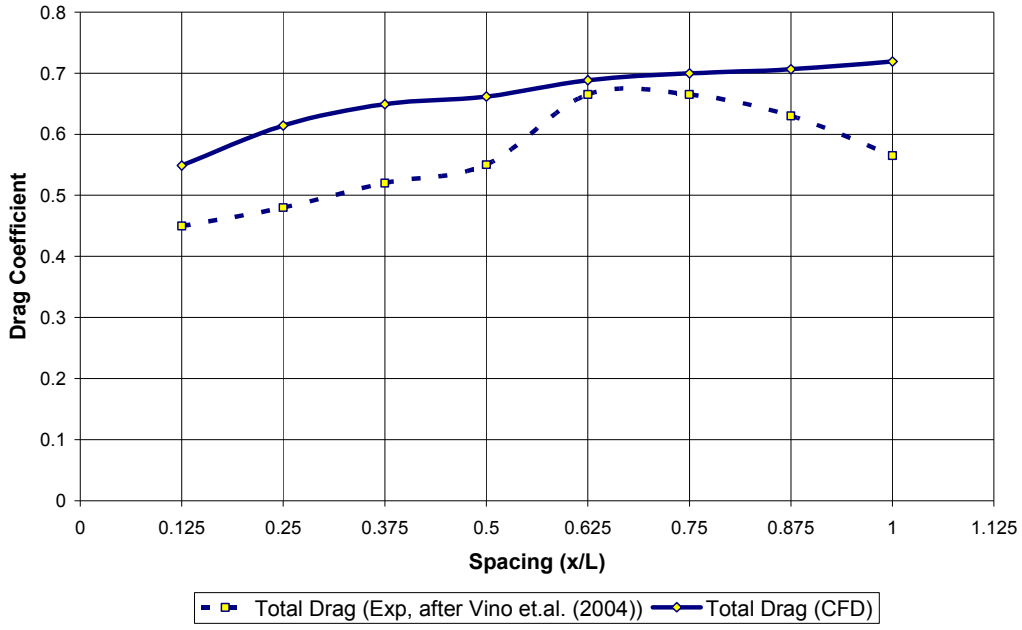

Figure 46. *Effects of inter-vehicle spacing on total drag coefficient - CFD & EFD comparison*

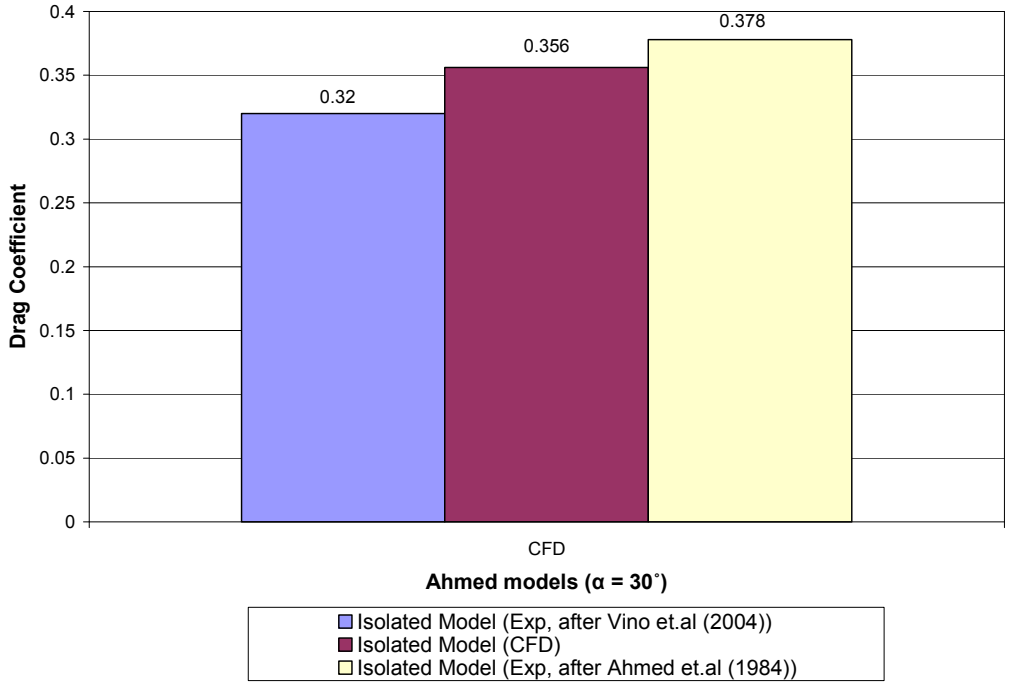

Figure 47. *Drag Coefficient comparison for isolated Ahmed model - CFD & EFD comparison*

The results for the isolated Ahmed model and the effects of drafting on drag coefficient using two models in tandem at close proximity are shown in figures 44 - 47. They shows the prediction of drag coefficient by the current CFD model for isolated Ahmed model geometry is in-between the experiments conducted in IWT at RMIT University and the literature value after Ahmed et.al (1984). The error percentage for the isolated model case (see figure 47) is less than 10%. The predictions of drafting effects on coefficient of drag shows some discrepancies, but the trends predicted are similar to those observed from the experiments, after Vino and Watkins (2004). This study clearly demonstrates that CFD can deliver useful predictions on vehicle's aerodynamics and therefore they can also be used to predict aerodynamic behaviour of vehicles traveling in platoons for FGITS.

4.2 Detailed Flow Behaviour and Forces over Ahmed Models

As mentioned in chapter 2, the Realizable k- ε model was selected in this investigation to be the turbulence model. The boundary conditions at inlet and outlet are velocity inlet and pressure outlet conditions, sides and ceiling are considered symmetry conditions, while the wall function is applied to the Ahmed car models and floor. The flow behaviours, obtained from numerical simulation from both two-dimensional and three-dimensional models, are presented in the sections below.

4.2.1 Two Dimensional (2D) Analysis

4.2.1.1 Isolated Ahmed models

The 2D analysis was initially performed for isolated Ahmed models although the flow structure is highly three dimensional in the real case scenario. This was mainly performed to understand the influence of rear slant angle on flow structures in the wake of an Ahmed model and also their corresponding influence on the model's drag coefficient. Path lines of velocity and pressure contours around the Ahmed

model were created by the post processing options provided in FLUENT version 6.1.22. The analysis was performed for rear slant angles of Ahmed model ranging from 0˚ to 40˚ with 5˚ increment. Critical angles were identified, i.e. the angle that produced significant change in flow structures in the wake and ultimately influenced the drag coefficient values of the models. The effects of these critical angles are discussed in detail below.

The domain and grid information are presented in Chapter 2 (CFD Analysis). The inlet velocity is 35 m/s with a model length base Reynolds number of 2.3×10^6.

The effects of rear slant angle on drag coefficient of 2D- Ahmed model geometry are shown below in figure 48.

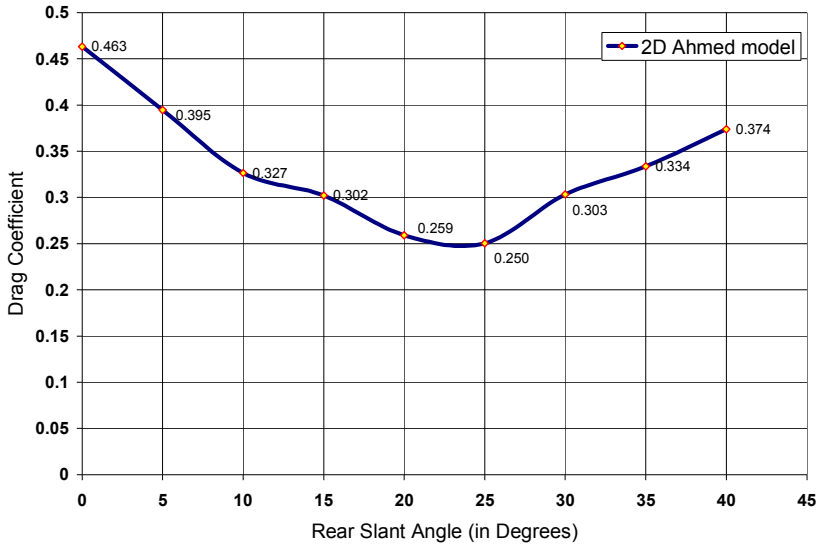

Figure 48. *2D effects of rear slant angle on drag coefficient*

The drag coefficient was found to be the maximum for the 0˚ rear slant configuration and then it gradually decreased to 0.250 for the 25˚ rear slant configuration. The drag coefficient started to increase after 25˚ rear slant angle to 0.374 at 40˚. Critical angles 0˚, 25˚, 30˚ and 40˚ were identified to explain influence of rear slant angle on the current drag coefficient trend.

The 0˚ degree configuration of an Ahmed model is shown in figure 49 (a) & (b). It can be seen that flow after reaching the front part stays attached on the body and separates at the sharp rear end leaving a large recirculation region behind the base, see figure 49 (a). This resulted in the increase of base pressure drop as shown in figure 49 (b), which constitutes the main reason for its highest drag coefficient among various rear slant configurations.

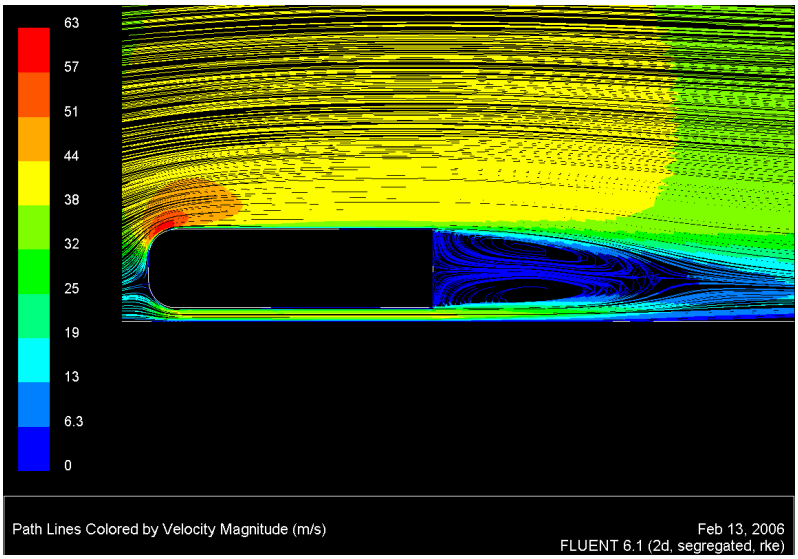

(a)

(b)

Figure 49 (a) & (b): *Velocity flow lines and pressure contours in the wake of 0˚ rear slant angle*

The 5˚ and 10˚ rear slant configurations exhibited more similar flow characteristics to that of the 0˚ rear slant configuration, except for the reduction of drag coefficient. This reduction in drag coefficients was mainly due to the reduced recirculation region, caused by the down wash created by the rear slant region of the Ahmed model.

The 15˚ and the 20˚ rear slant configuration, showed a considerable reduction in the size of the recirculation region. Hence the pressure recovery at the base was expected to be improved, thus ended in the reduction of drag coefficient (see figure. 48).

The 25˚ rear slant configuration exhibited the least drag coefficient of all the rear slant configurations of 2D-Ahmed model geometry. The recirculation region was considerably reduced by the significant down wash produced by the rear slant of the Ahmed model as shown in figure 50 (a).

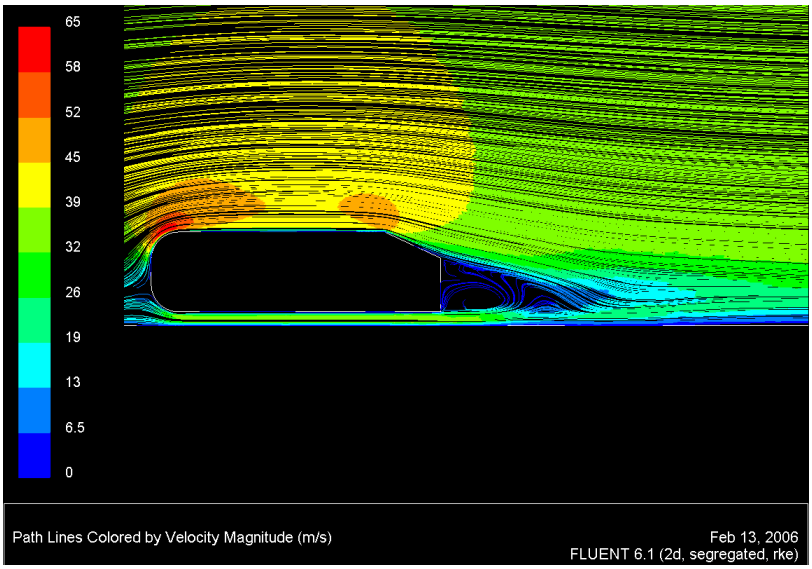

(a)

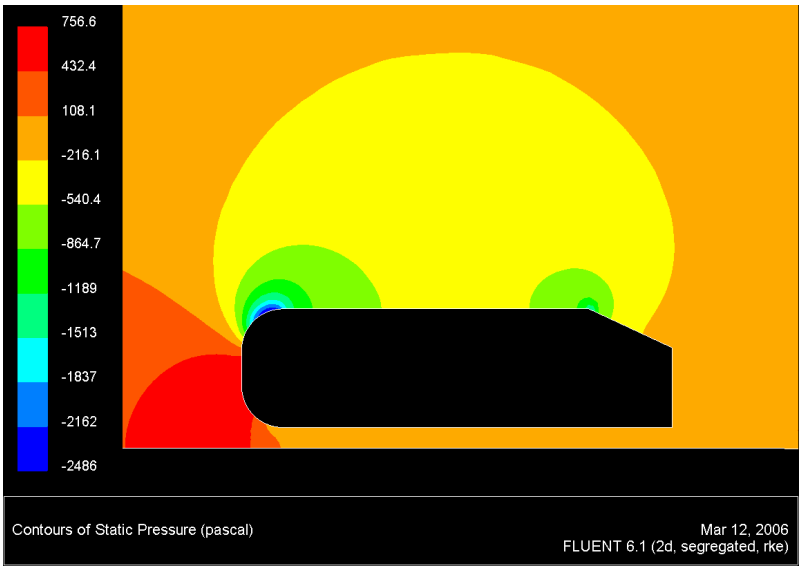

(b)

Figure 50 (a) & (b). *Velocity flow lines and pressure contours in the wake of 25˚ rear slant angle*

Among the two 2D vortices that were clearly visible in the previous cases, the upper vortex did not exist any more and the lower vortex seemed to have more effects on the vertical base. This effect helped to improve the pressure recovery of the model at its vertical base and ultimately reduced their drag coefficient, which can be seen from figure 50 (b).

Also, of all the rear slant configuration of 2D Ahmed models that were analyzed in this study, the pressure recovery was observed to be the highest for the 25˚ rear slant configuration.

The drag coefficient immediately started to increase with an increment or decrement of 5˚ from this critical 25˚ rear slant angle. An increase of angle contributed to the increase of drag coefficient which was observed for the 30˚, 35˚ and 40˚ rear slant configurations. At 30˚ rear slant angle, the drag coefficient increased sharply, by the direct flow separation from the leading edge of the rear slant as shown in figure 51 (a). Thus the recirculation region appears to have increased in size which would be expected to result in a pressure loss as shown in figure 51 (b).

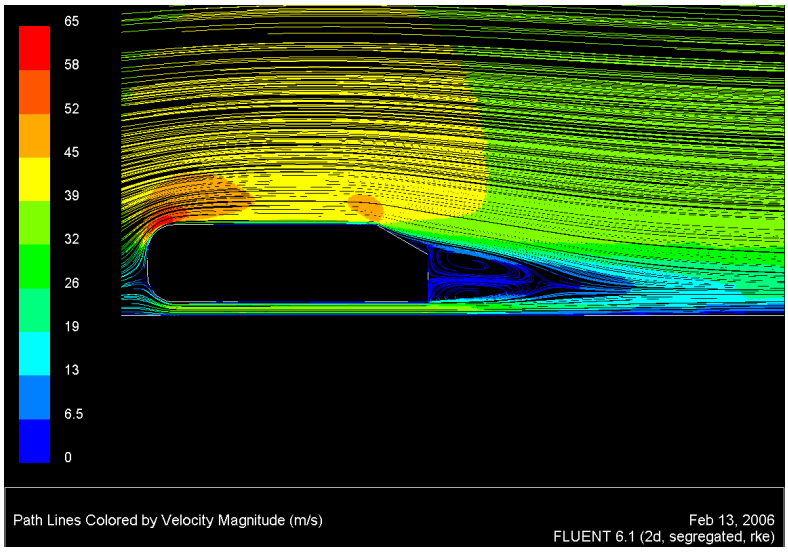

(a)

(b)

Figure 51 (a) & (b). *Velocity flow lines and pressure contours in the wake of 30˚ rear slant angle*

The effects observed on a 40˚ rear slant configuration are shown in figures 52 (a) & (b). The flow structures started to behave like those observed in models with rear slant angles between $0^\circ<\alpha<15^\circ$.

The flow that was attached before for the 25˚ rear slant configuration was not attached anymore and the flow separated directly from the leading edge of the rear slant (similar to 30˚ rear slant configuration). The upper vortex of the two 2D vortices

near the vertical base at the rear started to extend to the rear slant after 25˚. As a result, the recirculation region was increased since the rear slant did not support to have the flow attached to it. Also, this effect resulted in the increase of pressure drop and high drag coefficients as shown in figure 52(b) for the 40˚ rear slant configuration.

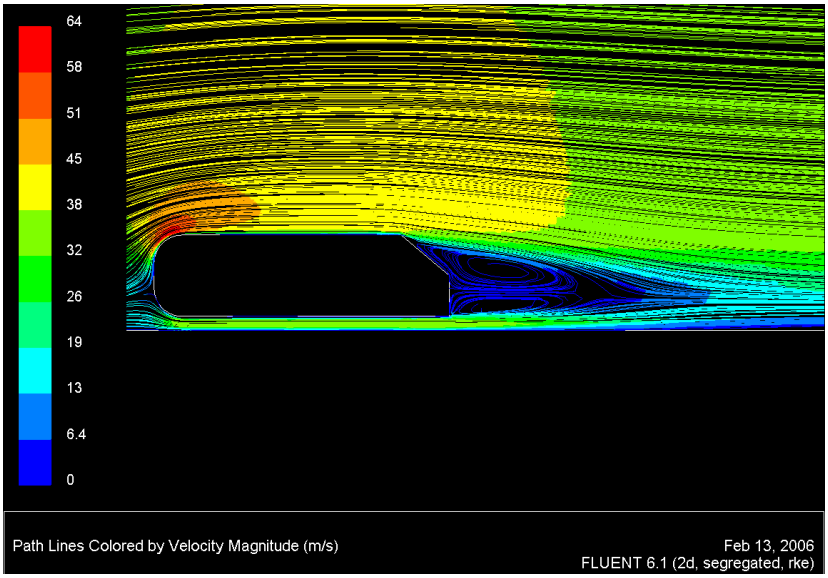

(a)

(b)

Figure 52 (a) & (b). *Velocity flow lines and pressure contours in the wake of 40˚ rear slant angle*

4.2.1.2 Two models in tandem

The previous 2D analysis on isolated models was extended to study the effects of drafting, in-order to have a preliminary understanding on the flow behaviour and the effects of inter-vehicle spacing on drag coefficients. The (3D) critical angle 30˚, after Ahmed et.al (1984) was considered to study these effects of drafting and only two models were used for this study.

Figure 53 shows the effects of vehicle spacing on drag coefficients. Two (2D) 100% scales of Ahmed model's are positioned in tandem one behind the other. The inter-vehicle spacing (x/L) was varied with respect to the length of the Ahmed model, which was 1.044m. For the current study the vehicle spacing was varied between x/L = 0.25 to x/L = 5. The inlet velocity was 35 m/s with a model length-based Reynold's number of 2.3 x 10^6.

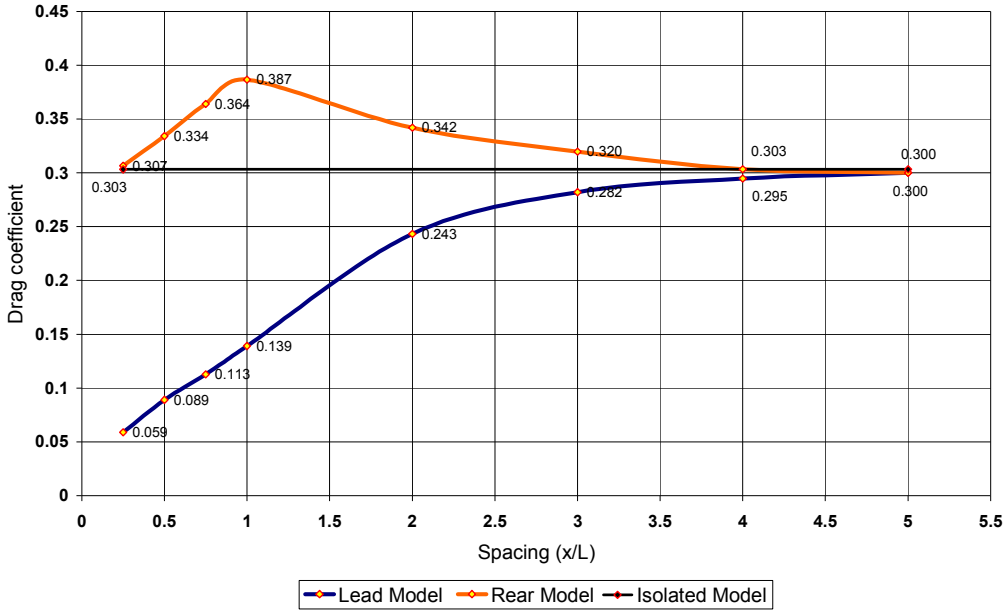

Figure 53. *2D effects of inter-vehicle spacing on drag coefficient*

It can be seen from figure 53 that at very close inter-vehicle spacing, the drag coefficient of the lead model was very much lower when compared to that of the rear model. This effect was mainly due to the presence of another model in its wake. The

presence of this rear model increased the base pressure of the lead model and therefore the lead model experienced less drag, see figure 54.

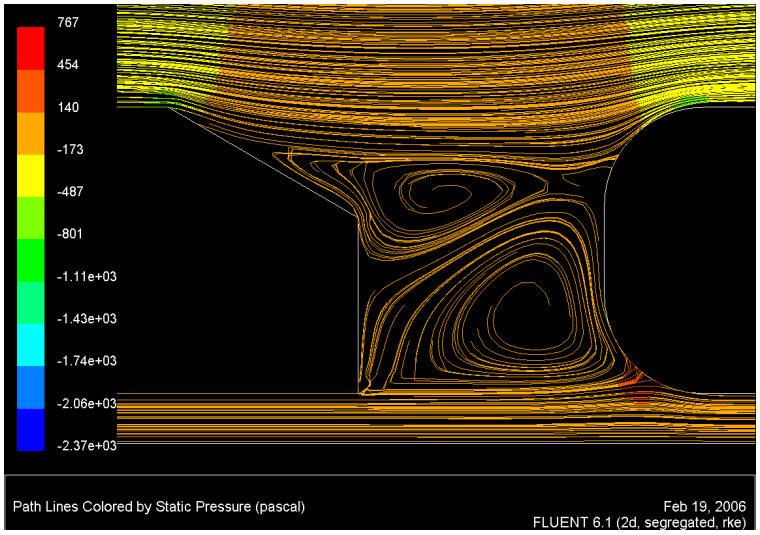

Figure 54. *Pressure path lines at x/L = 0.25*

Also, the flow that separated from the leading edge of the rear slant of the lead model created a flow impingement on the front portion of the rear model. This effect increased the drag coefficient of the rear model, which can be observed from the path lines of pressure in figure 54. Hoerner (1965) conducted experiments using two airfoils and observed similar effects on the trailing airfoil.

The lead model experienced low drag coefficients when compared to the drag coefficient of model in isolation (0.303) up to a vehicle spacing of x/L =5 which was contrary with respect to the trailing model. The major reason could be the pressure recovery percentage, which is expected to be higher for the lead model than the rear model.

At an inter-vehicle spacing of x/L =1 (see figure 55) the rear model's drag coefficient reached its peak value, this increase in drag was due to very high flow impingement. The lead model followed an increasing trend from x/L = 0.25 whereas the trailing model exhibited a varying trend since it followed an increasing trend from x/L = 0.25 to x/L= 1 and a decreasing trend from there onwards.

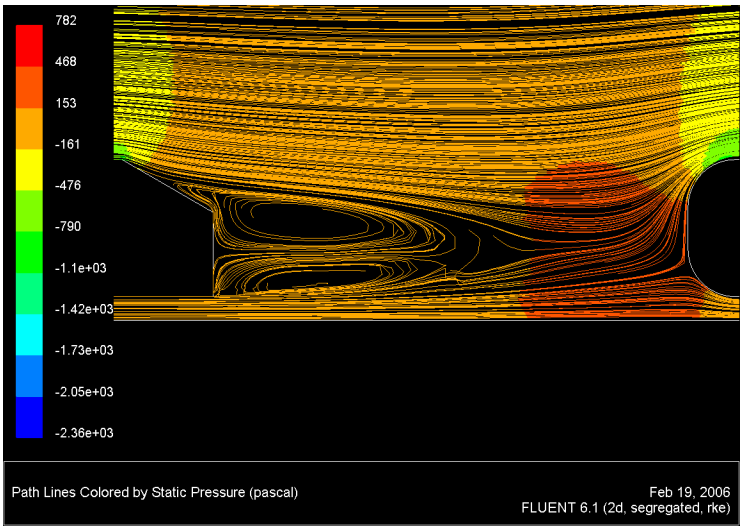

Figure 55. *Pressure path lines at x/L = 1*

As the inter-vehicle spacing increased, after x/L = 2 it was observed that the model started to behave more like a model in isolation, which can be seen from figure 56 at inter-vehicle spacing of x/L = 5. The wake region shown in figure 56 appeared very much similar to that of an isolated model for both the leading and trailing models.

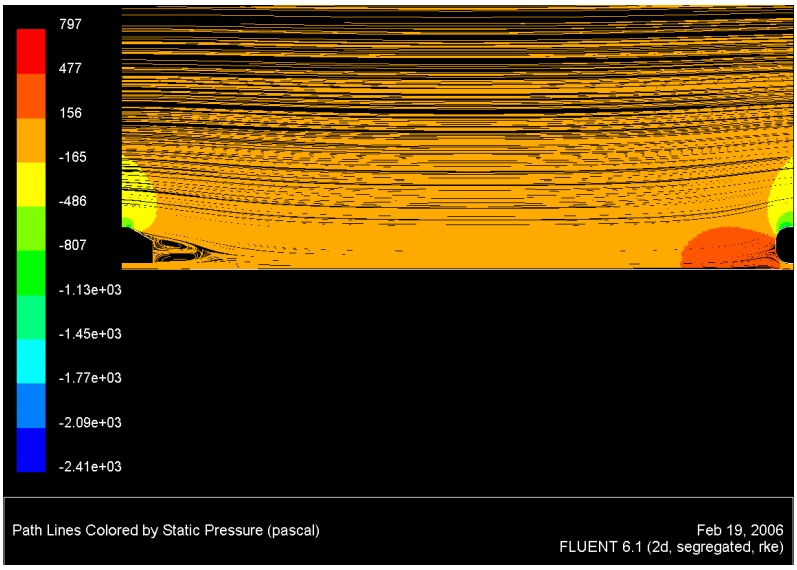

Figure 56. *Pressure path lines at x/L = 5*

4.2.2 Three Dimensional (3D) Analysis

4.2.2.1 Isolated Ahmed car model

3D study was performed to analyse the effects of rear slant angles on drag coefficient of Ahmed car models. After Ahmed et.al. (1984) and Johnson et.al. (2004) the Ahmed model was classified into three different regimes depending upon the flow structures generated at the wake region by their rear slant angles.

The different regimes are,

(i) Attached low drag regime

(ii) High drag regime and

(iii) Separated low drag regime

In the attached low drag regime, the flow is basically attached to the rear slant of the Ahmed model; the drag coefficient was substantially constant in this regime. This regime exists for $\alpha = 0^{\circ}$ to 12.5°, where the flow is attached to the slant with no distinctive C-pillar vortex formations, which can be seen from the figure 57 shown below.

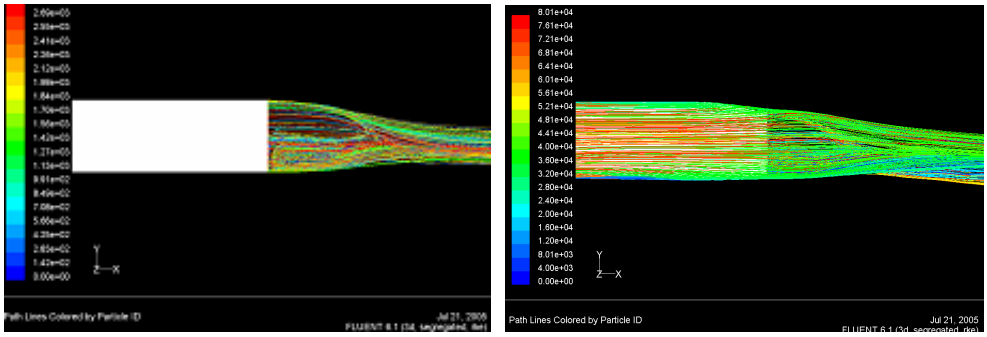

Figure 57. *Flow structures in the wake for 0˚ & 10˚ rear slant angle*

In the high drag regime, there is a sharp increase in drag coefficients, which is mainly characterised with the presence of strong counter rotating C-pillar vortices that are rich in kinetic energy as shown in figure 58 (a) and (b) for critical rear slant angle of 30˚.

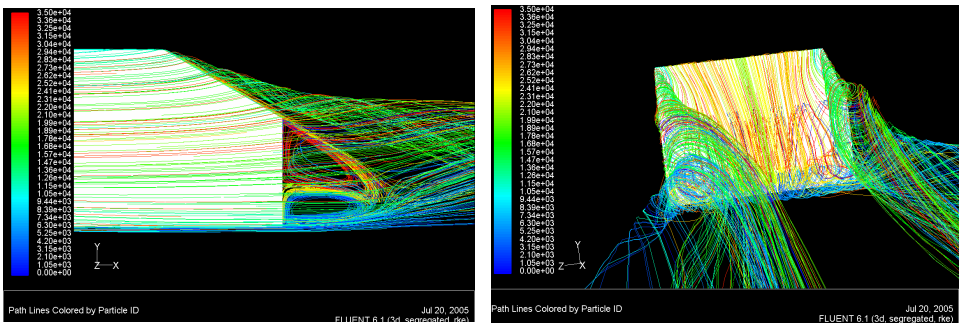

Figure 58 (a) & (b). *High drag configuration- Critical angle 30˚*

These vortices reduce the base pressure, there by increasing the pressure drag and ultimately the drag coefficients. This regime is also characterized by the presence of a separation bubble at its rear slant which could not be viewed computationally with the existing CFD model. The size of this separation bubble grows in size from 12.5˚ to 30˚ after which it breaks down, after Ahmed et.al. (1984).This regime exists for rear slant angles ranging between $12.5^\circ < \alpha < 30^\circ$.

The 30˚ rear slant angle of Ahmed model is often considered as the most critical angle of Ahmed model geometry after Ahmed et.al (1984) since any slight decrease or increase on angle would considerably reduce the drag coefficients. Also the size of the separation bubble reaches its maximum at $\alpha = 30^\circ$ which is one of the primary reasons for its highest drag coefficient. All the important flow features after Ahmed et.al. (1984) are recorded in this current study.

Finally in the separated low drag regime, the separation bubble on the rear slant doest not exist anymore and the flow separates directly from the leading edge of the rear slant and hence the strength of the C-pillar vortices are reduced resulting in a lower drag coefficient values. This regime exists for rear slant angles, $\alpha > 30^\circ$. The effect of rear slant angles on drag coefficient is shown in figure 59.

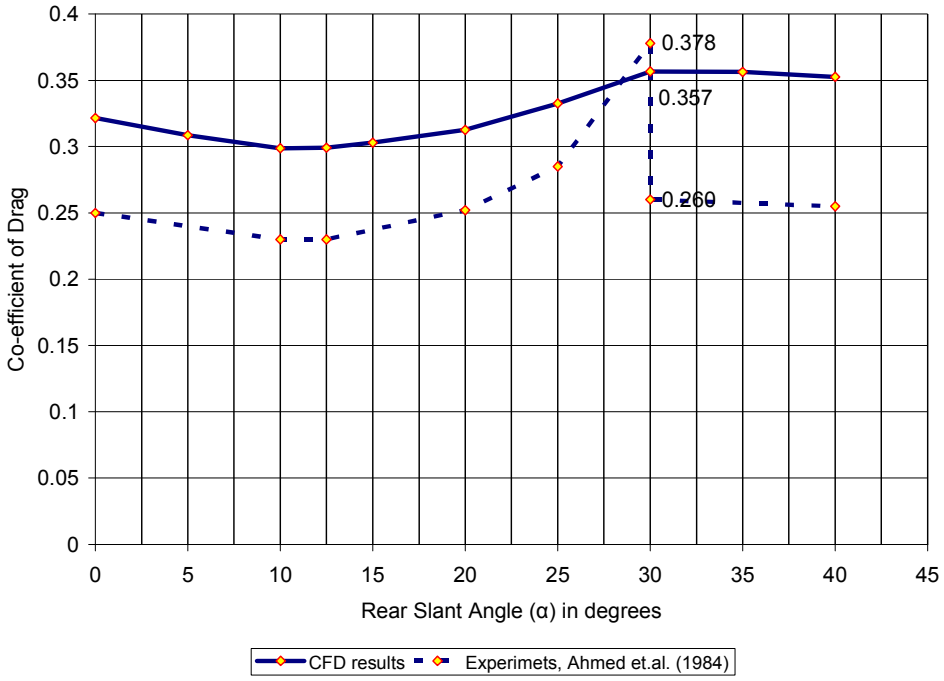

Figure 59. *3D analysis on the effects of rear slant angles on drag coefficients*

The negligible change of drag coefficients experienced in low drag regime, the sharp increase in drag coefficients in the high drag regime and the reduction of drag coefficients in separated low drag regimes can be seen from figure 59.

Although the drag predictions of the current CFD simulations are higher than the experiments, a similar trend is observed when compared to the previous studies after Gillieron and Chometon (1999) (see section 1.6.2, page 24, and figure 19). At the critical rear slant angle of 30˚, the prediction of drag coefficient is more accurate, than for other rear slant angles. The CFD predicted a drag coefficient of 0.356 when compared to experimental value of 0.378 with an error percentage of approximately 6%. However, when the CFD results are compared with the lower value of 0.260 at 30˚ slant angle, there is a significant difference; which could be due to the two dimensionality of the k – ε turbulence model.

4.2.2.1.1 Wake analysis

In order to examine the CFD wake simulation further, limited EFD wake analysis was performed for the precritical rear slant angle configuration of 25˚. The

EFD methods and other results can be found in Pagliarella et.al. (2005).The locations of grid points for measuring the velocity deficit in the wake are shown in the figure 60.

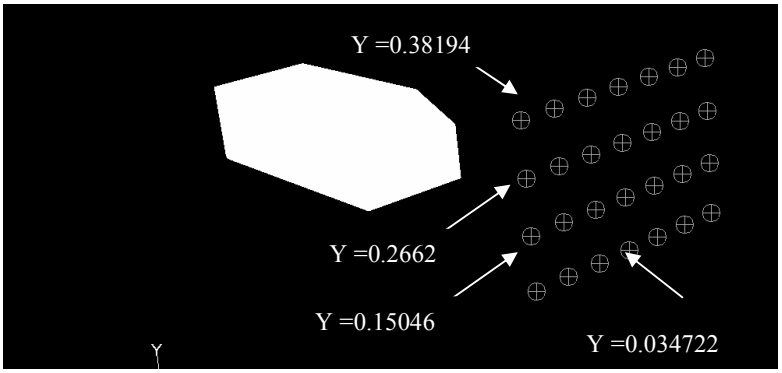

Figure 60. *Grid locations at the wake behind the Ahmed model at x/L =1*

The test velocity for both EFD and CFD simulations was 30m/s with a model length-based Reynold's number of 1.55 x 10^6 and all the measurements are made behind the model in the wake at about one model length as shown in the figure 60.

The experimental and CFD comparison for various values measured at every row of grid points in Y direction are shown in the following figures 61 (a),(b),(c)&(d).

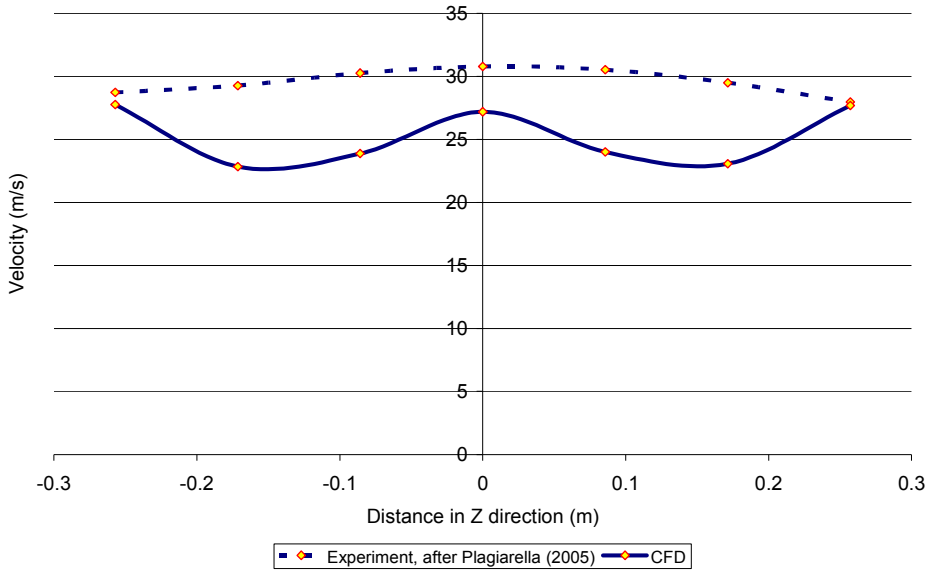

(a)

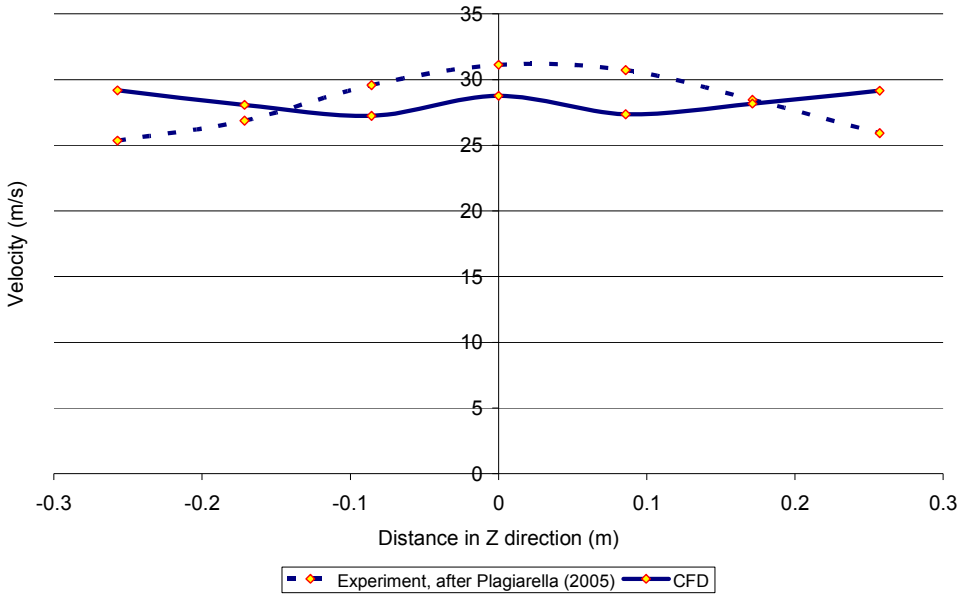
35
30
25
20
15
10
5
0
Velocity (m/s)
-0.3
-0.2
-0.1
0
0.1
0.2
0.3
Distance in Z direction (m)
Experiment, after Plagiarella (2005)
CFD

(b)

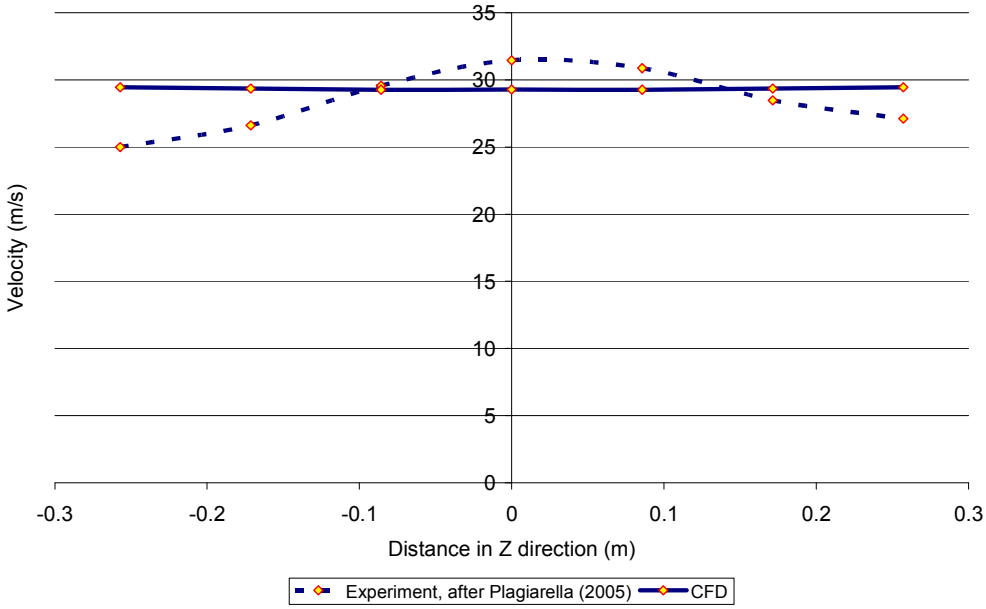
35
30
25
20
15
10
5
0
Velocity (m/s)
-0.3
-0.2
-0.1
0
0.1
0.2
0.3
Distance in Z direction (m)
Experiment, after Plagiarella (2005)
CFD

(c)

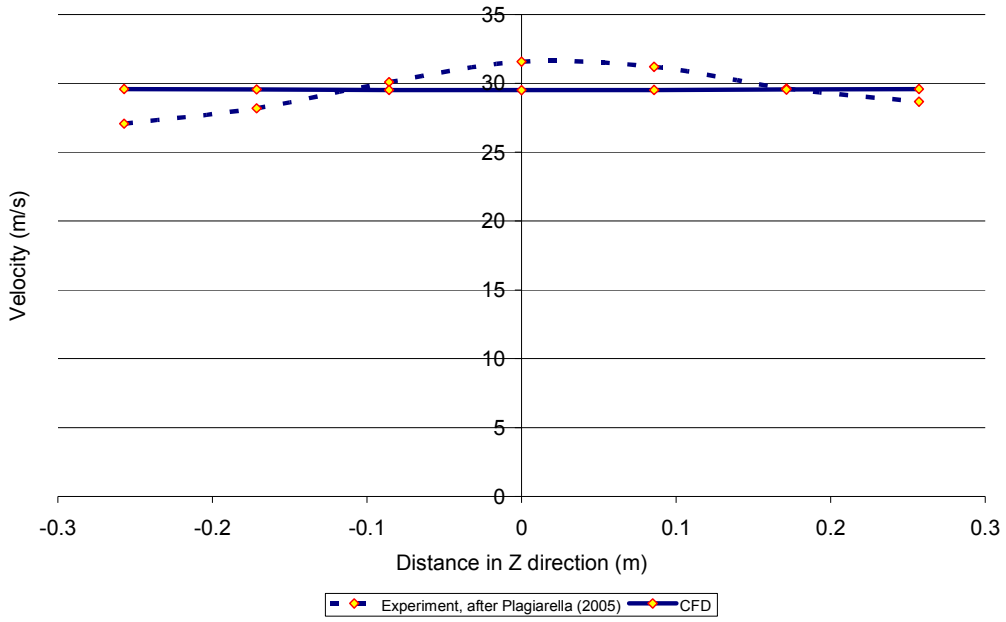

(d)

Figure 61 (a), (b), (c) & (d). *CFD vs. Experimental results at Y = 0.034722, 0.15046, 0.2662, 0.38194*

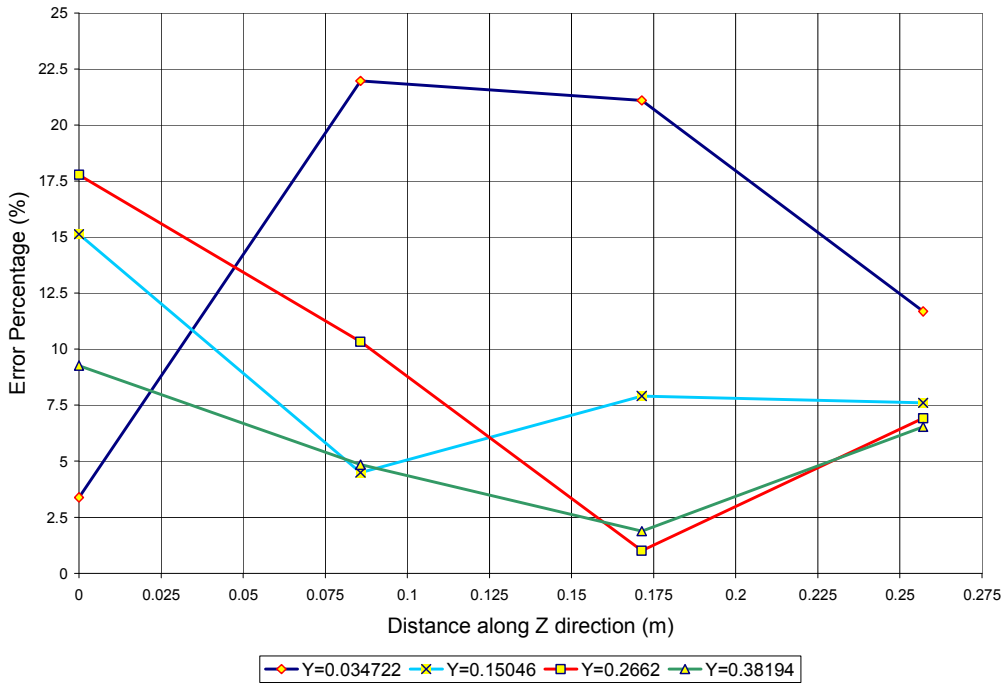

Figure 62. *Error percentage (%) at various grid points*

The above prediction of CFD indicates that the error percentage is more at the symmetry plane and is more in particular when comparing the values near the bottom

line of the Ahmed model (at Y=0.034722) as shown in figure 62. The error percentage is comparatively less between the symmetry plane and the corners of the model. Even though the error percentage is between 1% and 20% when compared to the experiments, moving higher, the current CFD model predicts the velocity to be almost constant which is contrary to the experimental observation.

In the experiments, while measuring the velocity deficit in the wake, the probe was positioned (moved) in increments of 2.5 mm. On the other hand, while performing computational validations the use of tetrahedral elements for meshing after one body length with grid size less than 2.5mm, stretched the total number of cell counts which the computer could not handle. Hence, a compromise was made to increase the cell size to 8mm at one body length. This could be one of the reasons for the discrepancy of values observed when compared to the experiments. The other reason could be the isotropic nature of the k – ε turbulence model. These two factors collectively have lead to this 20% error of CFD results over the experimental values.

Furthermore, these discrepancies added to an average error percentage of 15 % at Y=0.034722, which is the main reason for the current computational model's over prediction of base pressure drop and thereby higher drag coefficient predictions for most of the rear slant angle configurations.

4.2.2.2 Two models in tandem

4.2.2.2.1 Two 100% scale Ahmed car models

The effects of drafting was initially validated computationally and compared with the experiments conducted by Vino and Watkins (2004) at the Industrial Wind Tunnel at RMIT University using two 100% scale models of Ahmed models of 30˚ rear slant angles. The inter-vehicle spacing was varied with respect to the length (L) of the Ahmed model (1.044m) and the spacing was varied between 0.125 to 4 model lengths. The test velocity was 35m/s which correspond to the model length-based Reynolds number of 2.3 x 106. The CFD comparisons for the above experiments are shown in figures 63 and 64.

Lead Model:

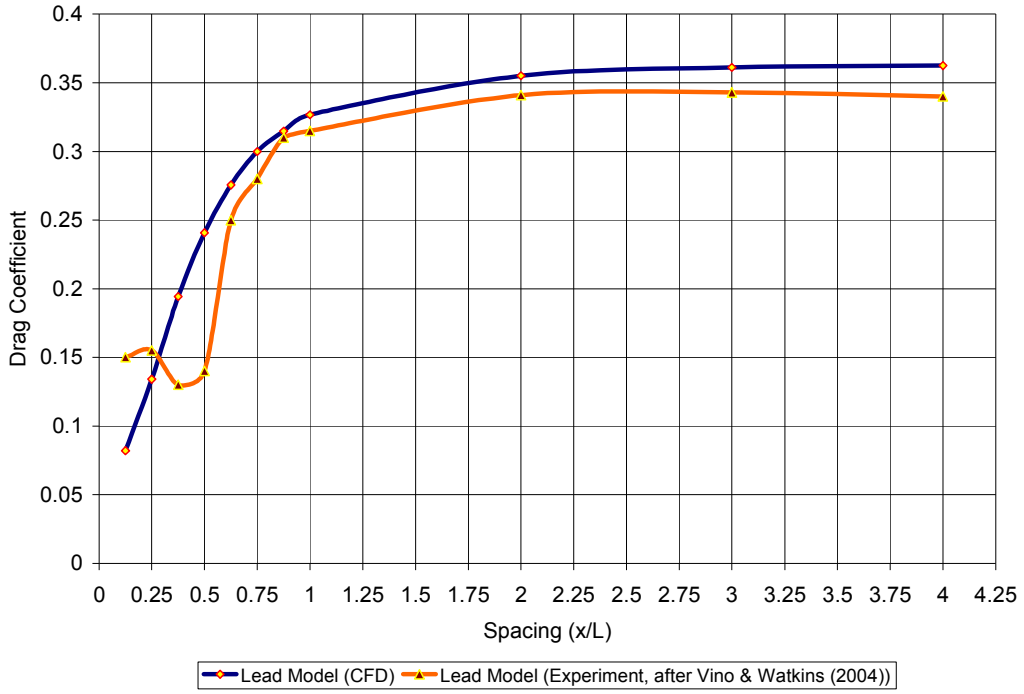

Figure 63. *Effects of inter-vehicle spacing on drag coefficient of lead model*

The trend was observed to be similar for both CFD and EFD; the slight over prediction of the computational values were mainly due to the overestimation of the base pressure drop, which was observed by Gillieron and Chometon (1999). This was also verified after analyzing the velocity deficit past the pre critical angle (25˚) of an Ahmed car model both experimentally and computationally, as shown in section 4.2.2.1.1.

At close proximity between 0.125 and 1 model length, the spacing increment was made for every 0.125 model lengths. It was found that the drag coefficient of the lead model was almost 70% less than that of the model in isolation when analysed computationally, and was around 55% after the experimental analysis of Vino and Watkins (2004).

The main reason for this low drag in the lead model is because, the strong C-pillar vortices generated at the 30˚ slant configuration of an Ahmed model does not exist at this spacing, due to the close presence of another model in its wake. The rear (trailing) model breaks the strong C-pillar vortices of the lead model that are rich in

kinetic energy and increases the base pressures of the lead model. Therefore the pressure lost due to flow separation is recovered by the lead model. The lead model therefore experiences a low drag coefficient till the effects on the presence of another model are felt in its near wake region. From the experiments of Vino and Watkins (2004) these effects on the lead model are experienced for inter-vehicle spacing ranging between $0.125<x/L<1$ and $0.125<x/L<2$ from the current CFD analysis.

The effect on the lead model after this particular spacing length changed gradually, i.e. the drag coefficient of the lead model started to increase with increase in inter-vehicle spacing. These effects were experienced in inter-vehicle spacing ranging between $1<x/L<4$ for the experiments and $2<x/L<4$ when analysed computationally. After an inter-vehicle spacing of $x/L = 1$ in experiments and $x/L = 2$ in CFD, the drag coefficients of the lead model almost became constant (The reason for the late change over in computational analysis was due to the codes over prediction of base pressure drop). The main reason for this behaviour was the pressure drop in the base, caused by flow separation was not recovered; also the rear model was not close enough to increase the lead model's base pressure. Thus, as the inter-vehicle spacing increased the drag coefficients of the lead model increased almost to the isolated model's drag coefficient value i.e. the model started to behave more like a model in isolation, which was observed both from the EFD and also the current CFD study.

Trailing/ Rear Model:

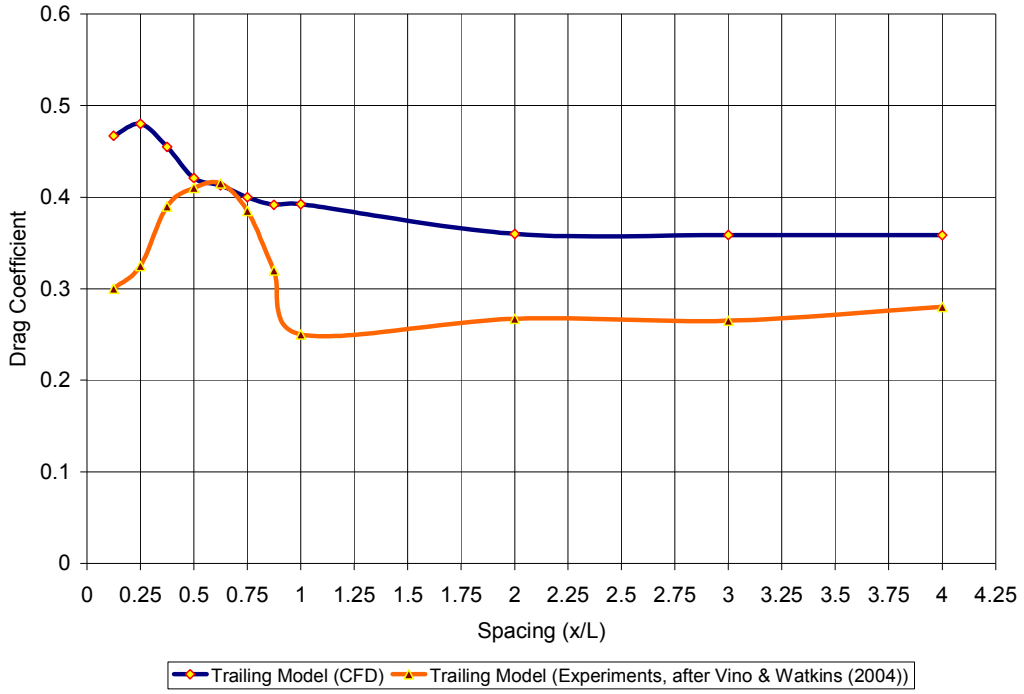

Figure 64. *Effects of inter-vehicle spacing on drag coefficient of trailing model*

At close inter-vehicle spacing, the effects of inter-vehicle spacing on rear (trailing) model was contrary to that of the lead model, since its drag coefficient was higher than that of a model in isolation. The reason for the increase in drag coefficients of the rear model in close proximity was due to the flow impingement from the rear slant of the lead model. This vortex interaction is shown in figures 65 (a) and (b).

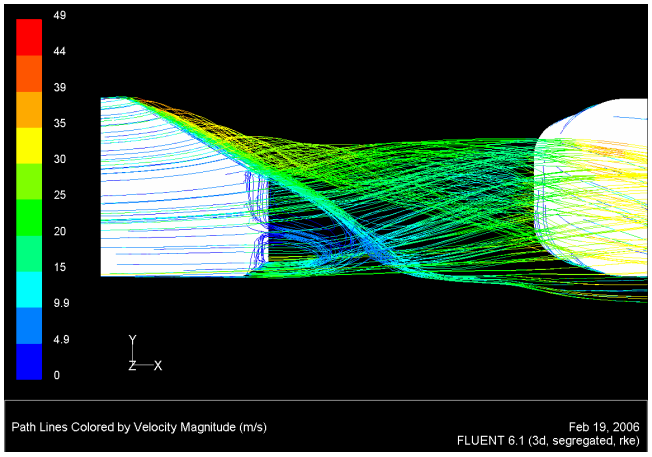

(a)

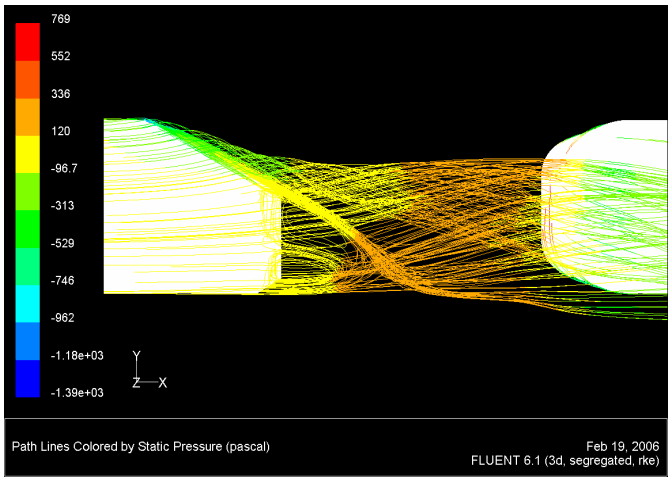

(b)

Figure 65 (a) & (b). *Flow impingement on rear model & pressure recovery of lead model at x/L = 0.25*

For a very small spacing (x/L = 0.125), the drag coefficient of the trailing model is approximately 0.323 experimentally and 0.467 in CFD. These results are somewhat expected and attributed to the presence of the upstream models wake. At such small gaps between the models, it is expected that very little kinetic energy exists in the flow resulting in substantial velocity deficits in between the models.

Surprisingly, an increase in model spacing is accompanied by a sharp increase in drag on the trailing model, which is observed both in the experiments and CFD. In fact, the drag on the model increases beyond that of the reference case (isolated model) and remains above it for the range $0.15 < x/L < 0.9$ in the case of experiments and $0.125 < x/L < 1$ for CFD analysis. The drag coefficient reaches a maximum value of 0.421 at x/L = 0.5 in experiments and 0.480 at x/L = 0.25 in CFD.

The work of Azim and Gawad (2000) suggests that this region of spacing may be associated with a flow mode termed 'vortex (or wake) impingement' whereby the high-energy vortices from the trailing car impinge on the front-end of the lead car, thus increasing the local dynamic pressures in front of the model. However, although Azim and Gawad predicted that while in a flow state of vortex impingement, the drag benefits would not be as great as for the 'low-pressure cavity mode' which occurred for both small and large gaps, drag benefits were nonetheless expected.

For gaps greater than x/L = 0.5 (EFD) and 0.25 (CFD), a significant drop in drag coefficient is observed, with drag reaching a minimum of 0.25 at x/L = 1 in experiments and 0.354 at x/L = 2 in CFD. Within the range 1 < x/L < 4, the drag coefficient remains low and gradually increases towards the reference value for the experiments and fairly constant when analysed using CFD. Trends observed from in figures 63 and 64, shows agreement with the work of Zabat et.al. (1994), who also found that a region existed where the drag of the trailing vehicle was larger than that of the lead model, while experiencing a local drag maximum.

The considerable discrepancies observed between the computational and the experimental value on the trailing model could be due to the errors associated with both the experimental and computational methods. The Ahmed model used in this experiment for measuring the forces was supported on a single strut, which despite producing time averaged results, created a large disturbed flow field around the model (since the measured model is expected to have oscillated during the tests). In addition, errors associated with the computational model such as the over prediction of base pressure drop have resulted in large discrepancies in predicting the drag coefficient of the trailing model.

4.2.2.2.1.1 Effects of Pressure recovery on the Lead and Trailing model

The effects of inter-vehicle spacing on their corresponding base pressure is analysed computationally using CFD. Base pressures are presented at 10 laterally displaced points at 0.05 m above the bottom of the Ahmed model on the vertical base. Three critical inter-vehicle spacings are analysed for the above case, they are

- x/L = 0.125 where the lead model's drag coefficient is minimum and the rear model's drag coefficient is at maximum.
- x/L = 0.25 where the rear model's drag coefficient reaches the maximum value of 0.4802.
- x/L = 1 where the drag coefficient drops significantly for the trailing model.

The reason for analysing close vehicle spacings, is due to the fact that drag coefficients are found to very sensitive to vehicle spacing ranging between $0.125 < x/L < 1$.

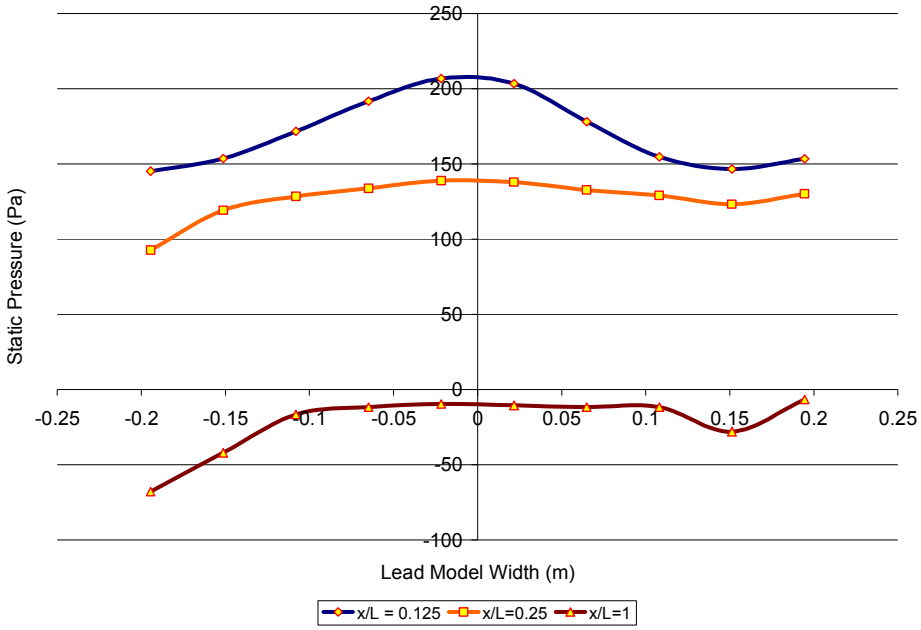

Figure 66. *Pressure recovery of Lead model for various inter-vehicle spacing*

It can be clearly seen from the figure 66, that at $x/L = 0$ the pressure recovered by the lead model is higher than that of tailing model and hence experiences least drag coefficient at that position.

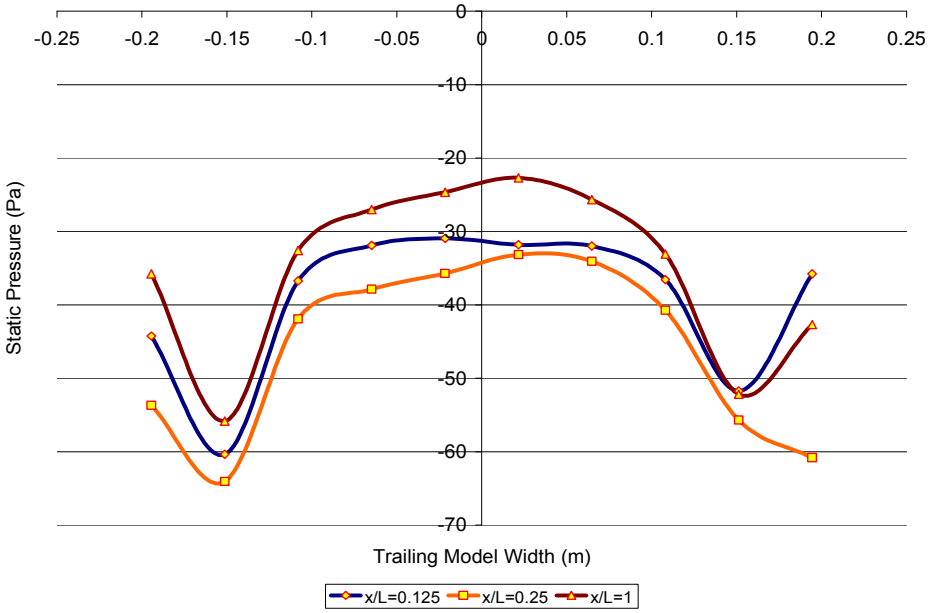

Figure 67. *Pressure recovery rear model for various inter-vehicle spacing*

As the inter-vehicle spacing increased the pressure recovery of the lead model decreased, and hence its drag coefficient increased as shown in figure 66. At x/L =0.25, the trailing model experienced higher pressure loss than it experienced at x/L=0.125 and hence its drag coefficient reached a maximum value at x/L=0.25, see figure 67.

Gradually when the inter-vehicle spacing increased to x/L=1, the drag coefficient of the lead model started to increase and the rear model started to decrease which could be seen from the reduction of pressure recovery in the lead model's base and a comparative increase of pressure recovery in the trailing model's base, as shown in figures 66 and 67.

Additionally, the reason for the lack of symmetry observed in figures 66 and 67 was due to the difference in cell counts and size on either side of the symmetry plane of the Ahmed model, which was due to the use of size functions.

4.2.2.2.2 Two Different Scales of Ahmed models in Tandem

The current research is extended to analyse the effects of inter-vehicle spacing using two different scales of Ahmed models with identical rear slant angles of 30˚. The experimental results on the effects of drag coefficient on the lead model due to spacing that is discussed in the previous chapter 3 is compared computationally with CFD. The effects of inter-vehicle spacing on drag coefficient of lead model are shown in figure 68.

The test velocity was 30 m/s with a model length based Reynolds number of 1.55 x 106 and the inter-vehicle spacing was varied between $0.25 < x/L < 2$. The lead model being the 75% scale model and the trailing model being the 100% scale model, the trend shown in figure 68 was observed to be similar in both CFD and EFD analysis. The drag co-efficient of the isolated Ahmed model from the experiment was 0.361 and 0.356 from CFD, with an error percentage of approximately 1.5%.

In the experiments all the forces are measured only with respect to the lead model owing to practical inadequacies and in CFD, the aerodynamic forces are computed on both the lead and the trailing models, as shown in figure 68.

Lead Model:

The trend observed in both the models are more similar to the two full scale models discussed in the section 4.2.2.2.1 except for the fact that, a linear trend was observed on the lead model's drag coefficient at close proximity, which was observed in both experiments and CFD as shown in figure 68.

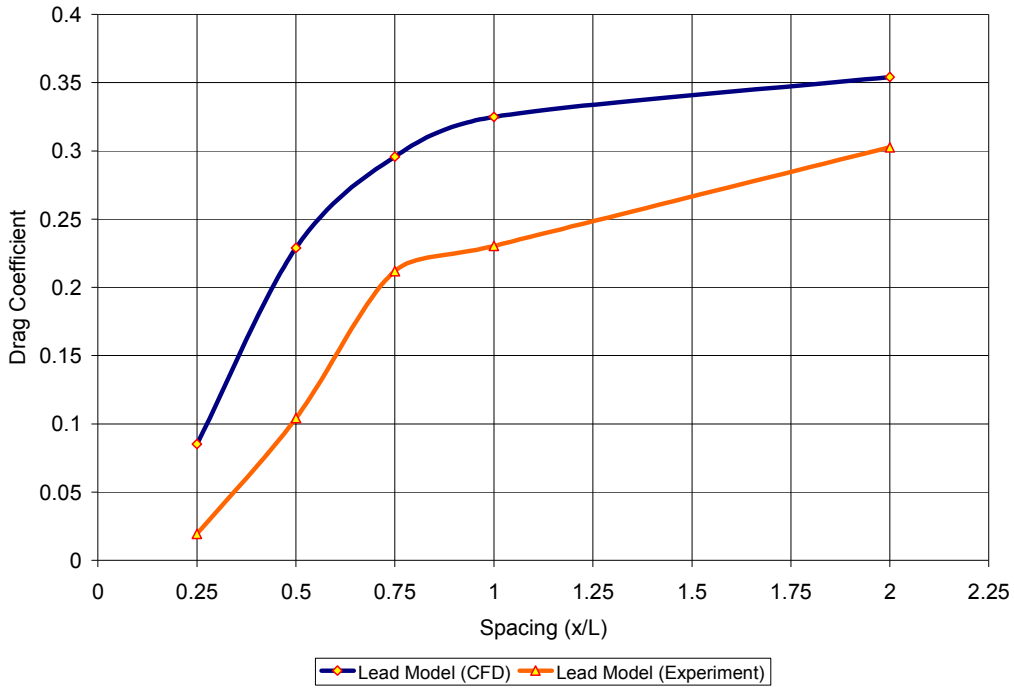

Figure 68. *Effects of inter-spacing on drag coefficient of lead model*

At extremely close proximity the lead model experiences minimal drag of 0.085. The drag co-efficient gradually increased till x/L =2 and slowly approached the isolated model's drag coefficient value. Also, a similar trend was observed in the experiments. The sharp decrease in lead model's drag coefficient that was found in the case of two 100% scale models was not found here, which might be due to the fact that both the models have different ground clearances (the lead model being the

smaller of the two has a lesser ground clearance). Also, the presence of the bigger model in its wake would have helped to have pressure recovery for longer inter-vehicle spacing.

Trailing/ Rear Model (CFD):

The measurements on the trailing model could be made only in CFD owing to software inadequacy encountered during experiments. As shown in figure 69, the drag coefficient reaches a maximum value of 0.501 at x/L = 0.25 which is mainly due to the vortex impingement. As the gap increases the vortex interactions diminishes and the drag co-efficient decreases to a value of 0.435 at x/L=2. Again, the decreasing rate of drag coefficient on the rear model is not faster when compared to the previous case on two 100% Ahmed models. This is because of the presence of a smaller model ahead. Thus, the trailing model experiences direct flow interaction apart from the flow impingement caused by the lead model, and hence it's higher drag coefficients.

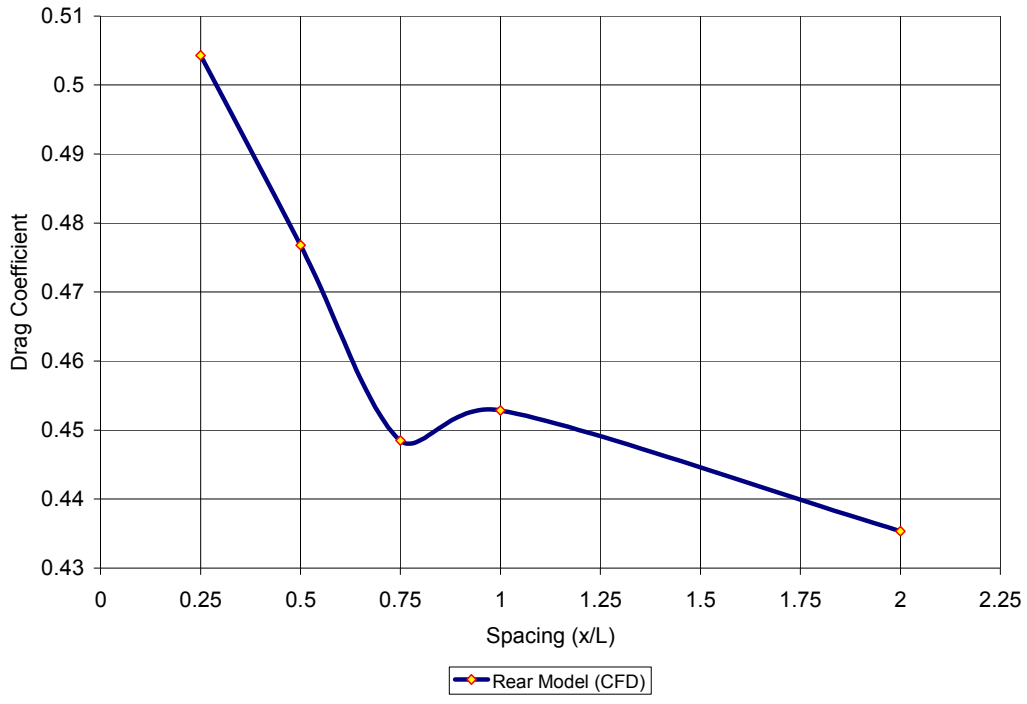

Figure 69. *Effects of inter-spacing on drag coefficient of trailing model using CFD*

4.2.2.3 Computational Analysis of Three & Six Models in Tandem

In order to understand the aerodynamics of longer platoons and, in particular, the aerodynamics of a single model in a long platoon, CFD simulations were made for three and six vehicle platoons. Also, the main reason for performing this study computationally without any experimental comparison was due to the limited test section length of the wind tunnel.

4.2.2.3.1 Three Ahmed models in Tandem

The positioning of models in the CFD domain is shown in figure 70.

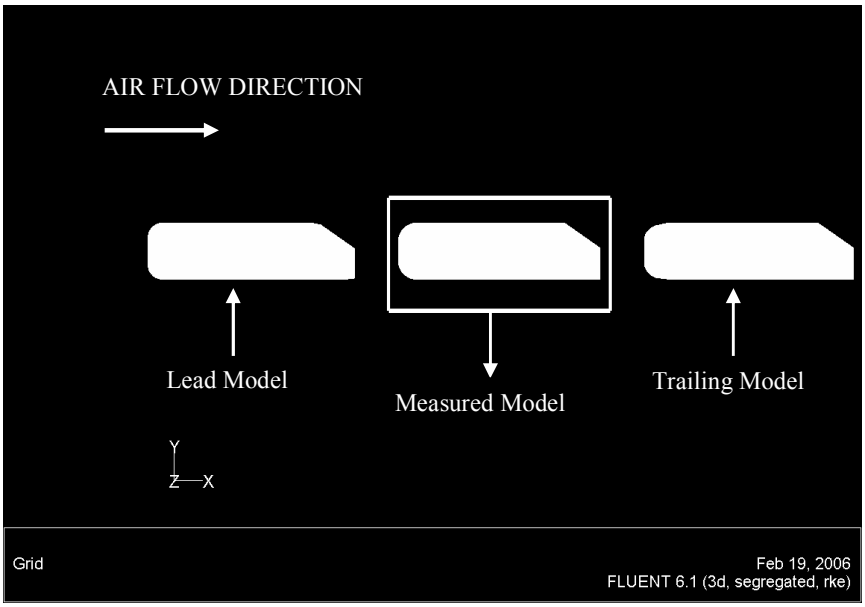

Figure 70. *Measured model positioning, for three models in tandem*

For a platoon of three models in series, the computational analysis was performed for two different rear slant angle configurations of Ahmed model geometry. Due to the large potential test matrix, only two slant angles were examined; these were 25˚ and 35˚.

The model positioning and the boundary conditions used were as discussed in chapter 2. The Inlet velocity was 30 m/s with a model length based Reynolds number

of 1.55 x 106. The inter-vehicle spacing was varied between x/L = 0.25 and 1. The computational results for the 25˚ and 35˚ slant angles are shown in figures 71 & 72.

At close inter-vehicle spacing i.e. at x/L = 0.25 the drag coefficient is minimum and increases linearly with the increase in inter-vehicle spacing to x/L = 1. Thus the value gradually approaches to an isolated Ahmed model's (25˚ rear slant configuration) value of 0.333. The main reason for the reduced drag coefficients is due to the high pressure recovery rate at the model's base, also the flow is attached to the rear slant surface. Again, as shown in the previous cases (see figures 66 & 67), the pressure recovery rate diminishes with increase in inter-vehicle spacing and hence the increasing drag coefficient trend is found till x/L = 1.

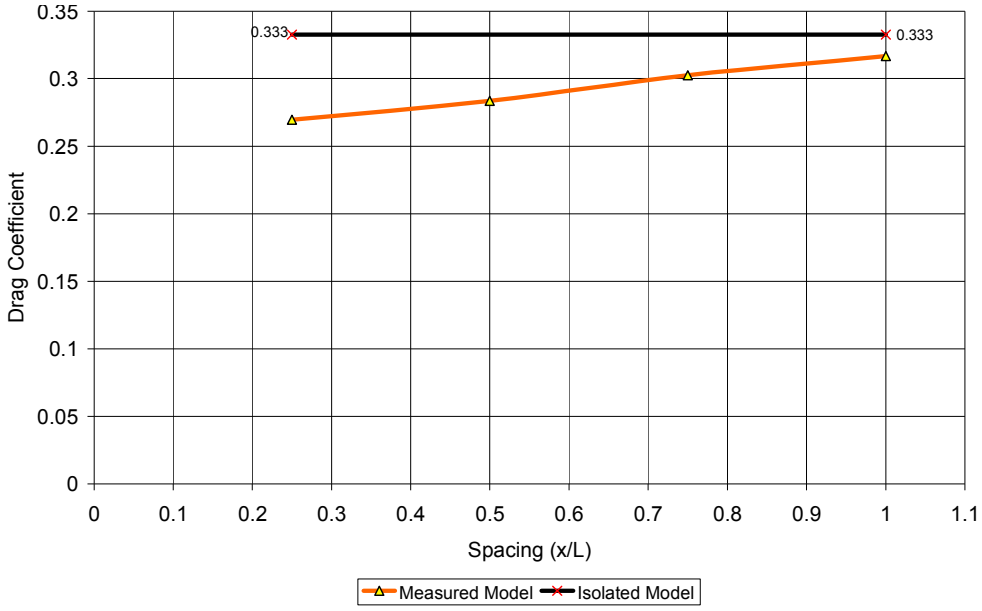

Figure 71. *Effect of spacing on drag coefficient for 25˚ rear slant configuration*

The effects of inter-vehicle spacing for 35˚ rear slant are shown in figure 72. As the C-pillar vortices loses its strength and the separation bubble does not exist for these rear slant configurations of Ahmed models, the flow separates straight away reducing their base pressures even at very close spacings.

At x/L = 0.25, the drag coefficient is 0.377 which is higher when compared to the isolated model's drag coefficient. The drag coefficient then drops to 0.334 at x/L = 0.5. It is the only position where the drag coefficient is lesser than the model in

isolation since thereafter the drag coefficient rises to 0.383 at x/L =1. Again, when the inter-vehicle spacing increases, the drag coefficient approaches the isolated model drag coefficient value, i.e. the model starts behaving more like that in isolation.

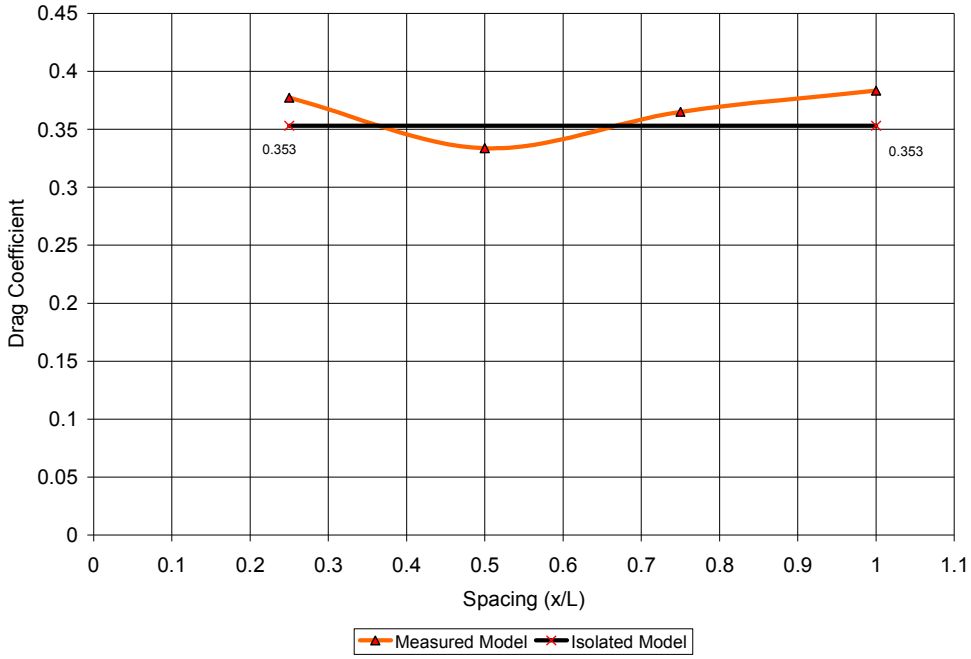

Figure 72. *Effect of spacing on drag coefficient for 35˚ rear slant configuration*

The main reason for this behaviour found in the post critical configuration is at very close spacing of x/L = 0.25, the measured model experiences flow impingement on its front part from the separated flow of the lead model, when the flow reaches, its rear end it separates with minimal pressure recovery. This lost pressure is recovered when the spacing increases to x/L = 0.5, hence minimal drag is experienced by the measured model at this position.

The pressure recovery for the measured model at x/L = 0.5 is mainly because, the weak vortices that leaves the rear slant of the measured model interacts with the front part of the trailing model, which in-turn helps to increase the base pressure of the measured model. Also, the reason for the absence of this pressure recovery at other inter-vehicle spacing is because, the flow that leaves the measured interacts more with the body portion (middle portion of the Ahmed model) of the trailing model. This does not contribute to increase in base pressures for the measured model.

4.2.2.3.1 Six Ahmed models in Tandem

The study is extended to six models in tandem in order to simulate an isolated model in a long platoon. The reason for selecting 6 models to simulate the effects on an infinitely long platoon is after previous analysis performed on 4, 5, 6 and 7 model platoon for the critical 30° rear slant configuration after Ahmed et.al (1984) at inter-vehicle spacing of x/L =1, which is shown in figure 73.

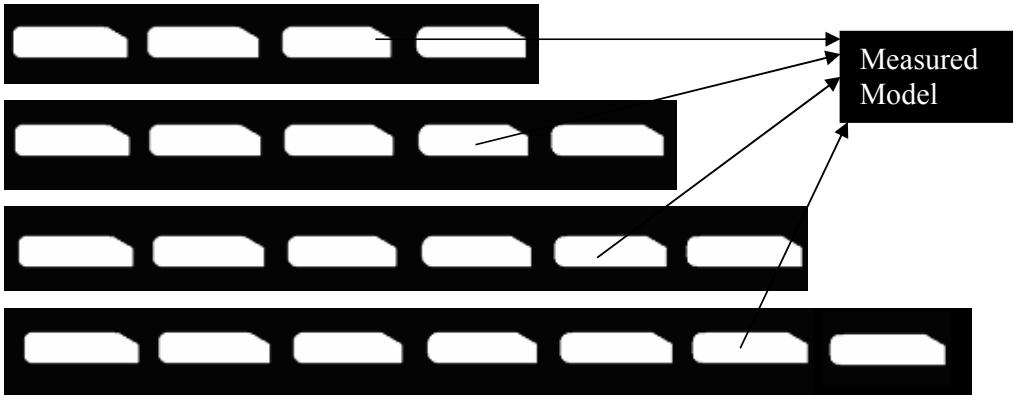

Figure 73. *Cases performed to simulate an infinitely long platoon of vehicles*

In all the above cases mentioned, the measured model is the $(n-1)^{th}$ model (where, n is the total number of platoon members) from the inlet direction (i.e. for a six model platoon, the 5^{th} model is the measured model) and all the aerodynamic forces are measured on this model using CFD for the current study. The effects of drag coefficients for all the above combinations of vehicle platoons at an inter-vehicle spacing of x/L =1 are shown in figure 74.

It can be seen from figure 74 that for a 5, 6 and 7 model platoon, the measured model experiences nearly identical drag coefficients. This consistency led to choosing the 6 model platoon for simulating the effects of an infinite platoon series. Additionally, since the measured model is positioned sufficiently far down the platoon, the model results (drag coefficients) are considered to approach those of a model in an infinitely long platoon.

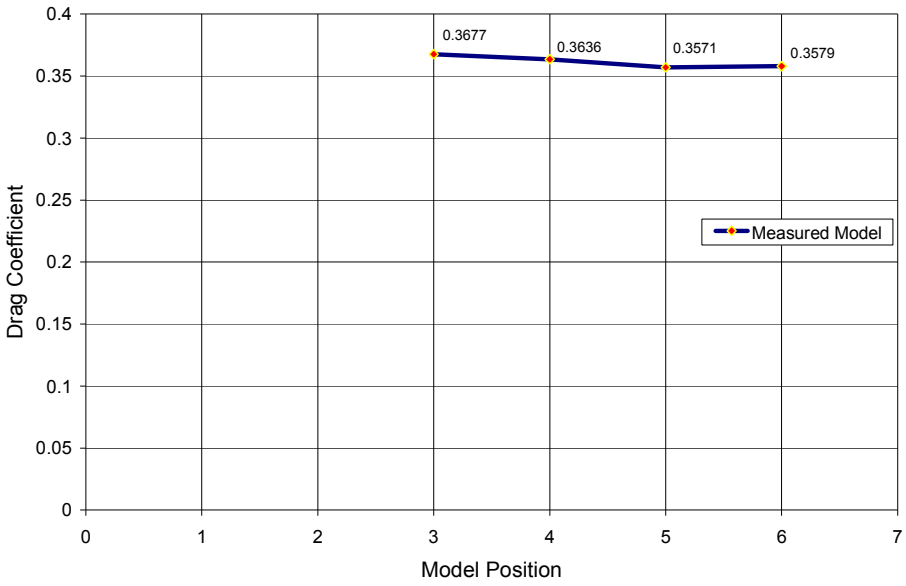

Figure 74. *Effects of model positioning on drag coefficients*

The positioning of models in the CFD domain for a six model platoon, are shown in detail in figure 75.

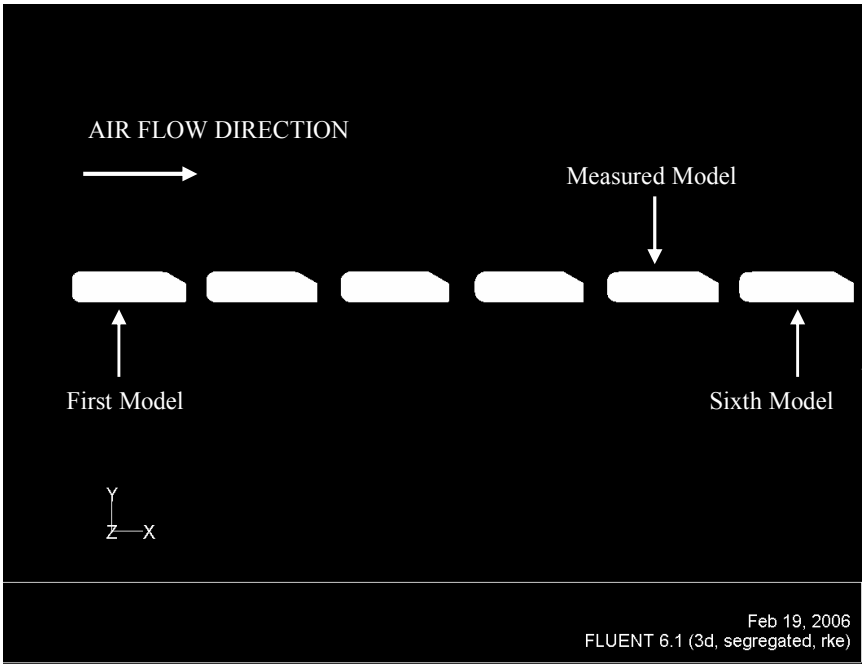

Figure 75. *Measured model positioning, when six models in tandem*

The test velocity was 35m/s with a model length-based Reynolds number of 2.3 x 10^6. The model positioning and the boundary conditions used were discussed in chapter 2. The inter-vehicle spacing was varied between x/L = 0.25 to x/L = 6 (in model lengths). For a platoon of six models in tandem, the computational analysis is performed for all the rear slant angle configurations of the Ahmed model geometry.

The cases performed having six models in tandem are as follows,

i. A platoon of six models all with attached low drag rear end geometries (between 0˚ & 15˚)
ii. A platoon of six models all with high drag rear end geometries (between 15˚ & 30˚)
iii. A platoon of six models all with separated low drag rear end geometries (between 30˚ & 40˚)

The computational results for the above cases are shown in figures 76 - 84.

The 0˚ rear slant configuration shown in figure 76 does not possess any counter rotating longitudinal vortices; the flow separates from the rear end and does not reattach thus causing a wide wake region. Therefore, when models are stacked up to form a platoon, the drag coefficients of the measured model will always stay below than that of a model in isolation. This is because the pressure drag is always less because of the presence of lead models and a trailing model, which affects the wake region. The drag coefficient drops down to a minimal value of 0.114 at x/L = 0.5 and then increases gradually to 0.236 at x/L = 6, thus approaching the isolated model's drag coefficient value.

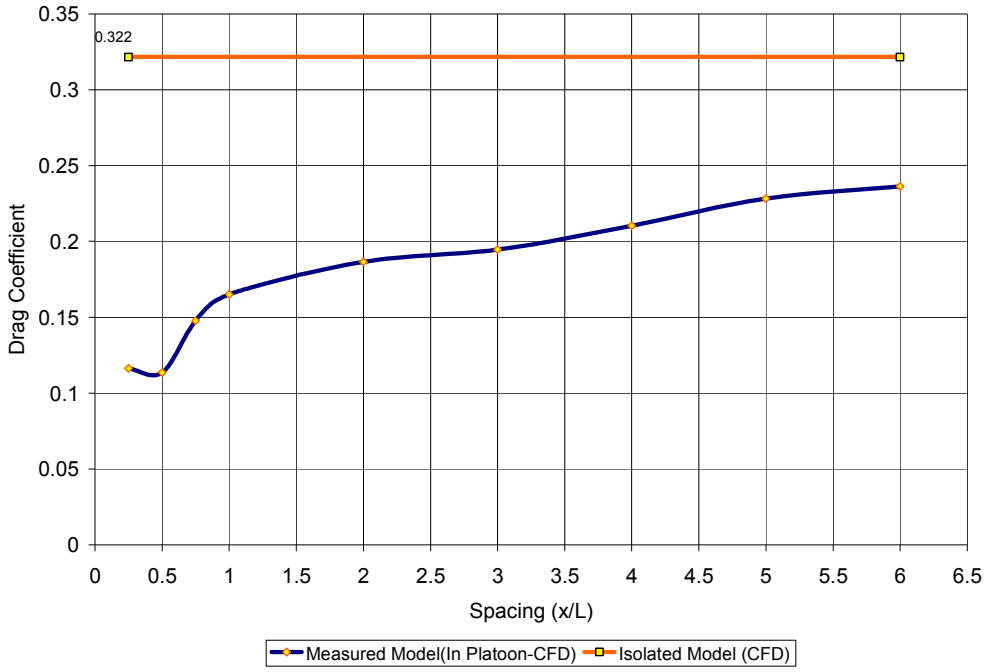

Figure 76. *Effect of vehicle spacing on CD of measure model with 0˚ rear slant angle*

The 5˚ rear slant configuration, shown in figure 77 behaves in a similar manner to the 0˚ rear slant configuration. For the 5˚ rear slant configuration in isolation, the wake region is smaller when compared to the 0˚ configuration. Similar to the 0˚ configuration the drag coefficient drops to a minimum at x/L = 0.5. The distinctive drop of drag coefficient at x/L = 0.5 is mainly due to the pressure recovery at the measure model's base. The drag coefficient then increases gradually till at x/L = 4. There is a significant increase to x/L = 5 and it remains fairly constant from there onwards.

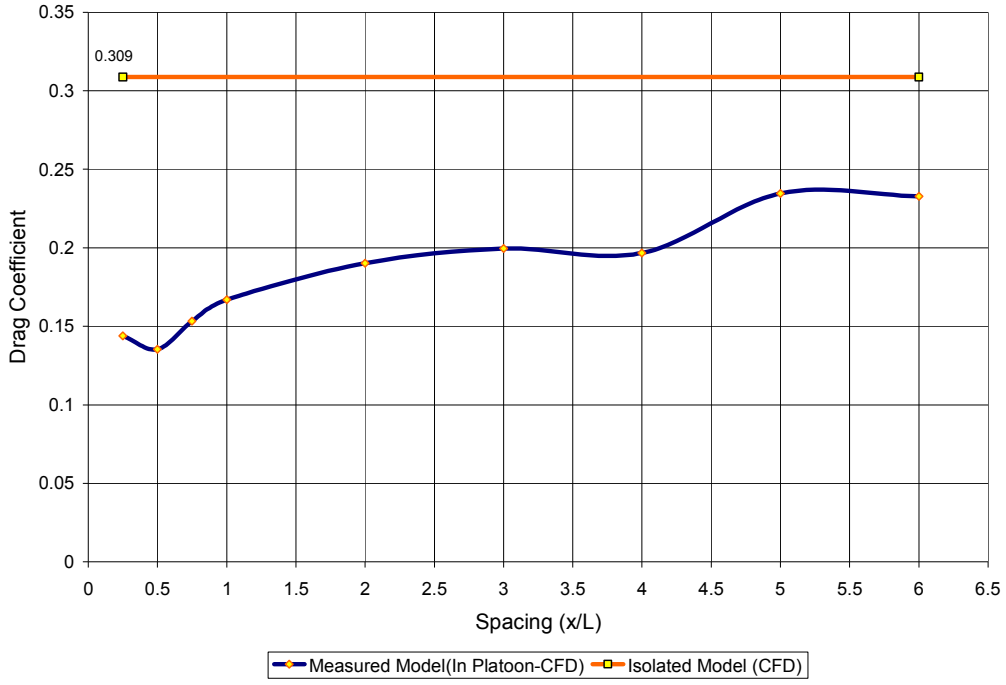

Figure 77. *Effect of vehicle spacing on C_D of measure model with 5˚ rear slant angle*

Results for the 10˚ rear slant angle are shown in figure 78. At this stage these vortices possesses less kinetic energy and are attached to the rear slant of the Ahmed model. The drag value is 0.147 and is least at x/L = 0.25. The drag co-efficient increases to 0.192 at x/L = 0.5 followed by an increase to 0.220 at x/L =1. After an inter-vehicle spacing of x/L = 1 the drag co-efficient is maintained fairly constant and varying within the limits of ± 3%.

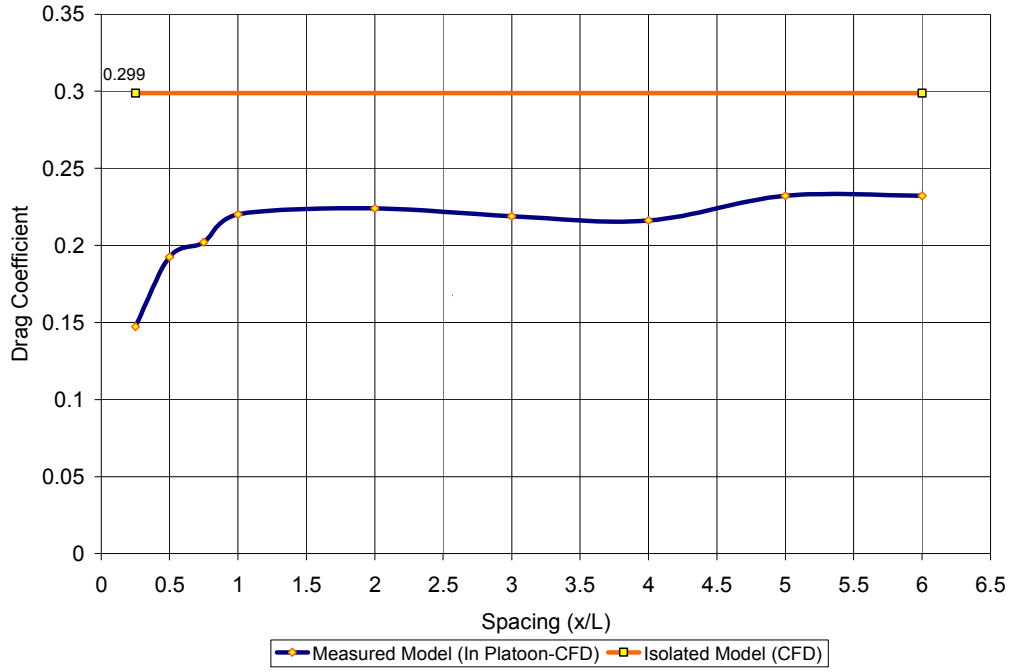

Figure 78. *Effect of vehicle spacing on CD of measure model with 10˚ rear slant angle*

The formation of C-pillar vortices and flow impingement on the front face of the measured model with increase in inter-vehicle spacing are the main reasons for the increase in drag coefficient. The reason for constant drag coefficient after one model length i.e. after x/L = 1 is thought due to the fact that the flow impingement rate on the measure model and the pressure recovery rate by the measure model becomes almost constant.

As can be seen in figures 79 and 80 the regime between models having 15˚ and 30˚ rear slant angle is called the high drag regime. The 15˚ configuration shown in figure 79 comes under this high drag regime which is characterized with the development of stronger C – pillar vortices. From a minimum of 0.181 at x/L = 0.25, the drag coefficient increased to 0.253 at x/L = 1. The trend is gradually decreasing from there on up to x/L = 4 where the drag coefficient is 0.236. The drag coefficient then gradually increases to 0.248 at x/L = 6, thus tending to approach the isolated model's drag coefficient value. Also, the decreasing trend at 1< x/L < 4 is thought mainly due to the decrease in the intensity of vortex interactions between the measured model and adjacent models.

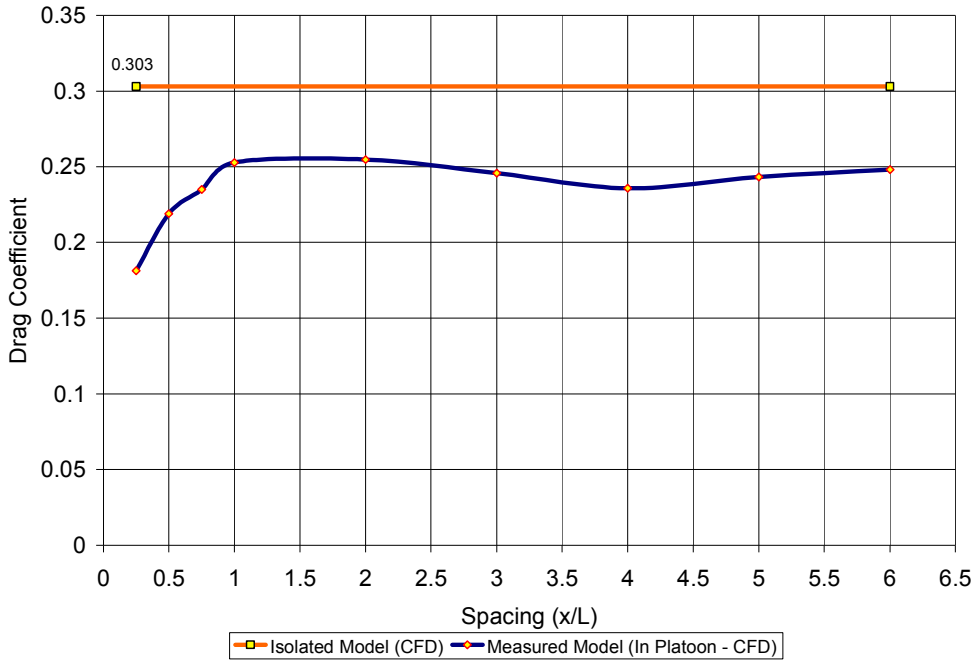

Figure 79. *Effect of vehicle spacing on C_D of measure model with 15˚ rear slant angle*

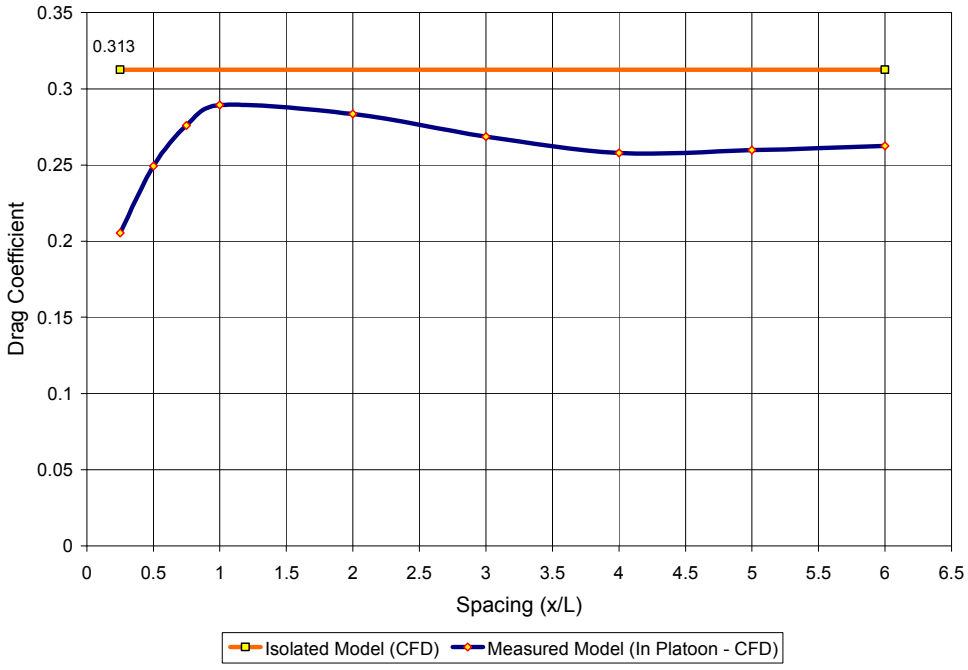

Figure 80. *Effect of vehicle spacing on C_D of measure model with 20˚ rear slant angle*

The 20˚ rear slant angle configuration exhibits similar trends of 15˚ rear slant configuration (see figure 80). The drag coefficient increases sharply from a minimum

of 0.205 at x/L = 0.25 to 0.289 at x/L = 1. This sharp increase is followed by a gradual decrease to 0.258 at x/L = 4 and the trend remains fairly constant from there onwards.

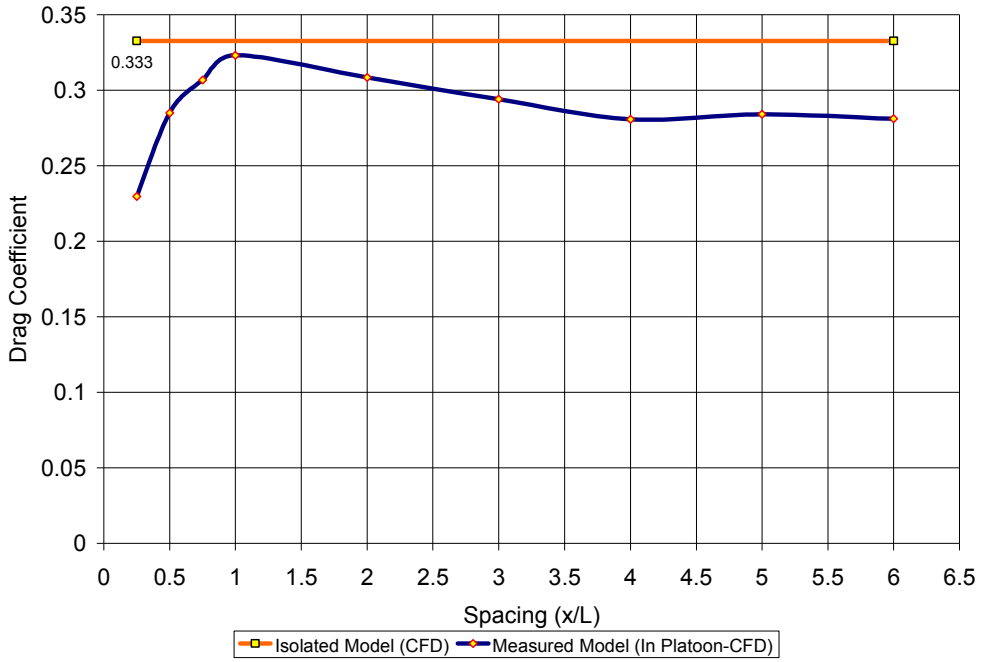

Figure 81. *Effect of vehicle spacing on CD of measure model with 25˚ rear slant angle*

The trend exhibited by 25˚ & 30˚ rear slant configurations is more similar to the 20˚ rear slant configuration which is shown in figure 81 and 82. The drag coefficients for both the cases almost approaches the isolated model's drag coefficient value at an inter-vehicle spacing of x/L =1. In the case of 30˚ (critical angle) configuration, the drag coefficient has even slightly exceeded the isolated model's drag coefficient of 0.356 to 0.357 as shown in figure 82.

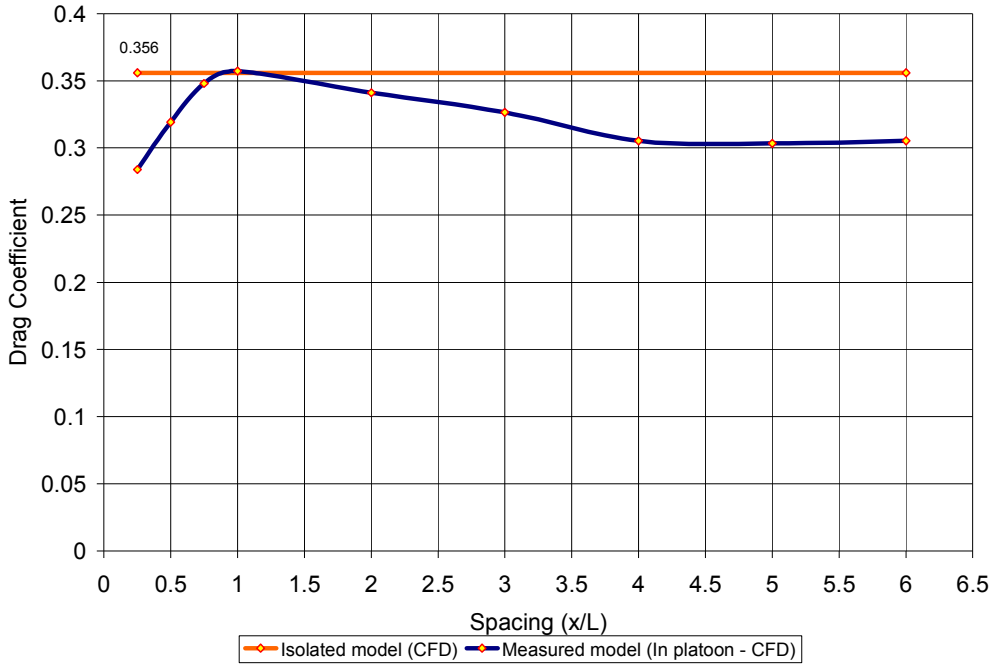

Figure 82. *Effect of vehicle spacing on CD of measure model with 30˚ rear slant angle*

The regime of rear slant angles greater than 30˚ is called the separated low drag regime. The strength of the C-pillar vortices in this regime is broken as the separation bubble on the rear slant no longer exists. Thus the vortices possess very little kinetic energy. This makes the flow not even partially attached to the rear slant of the Ahmed model.

For the 35˚ rear slant configuration (see figure 83), the drag coefficient sharply increases from 0.343 at x/L = 0.25 to 0.391 at x/L = 1, which exceeds the model's isolated drag coefficient value of 0.356. From an inter-vehicle spacing of x/L = 1, the drag coefficient gradually decreases to 0.323 at x/L = 6. Though, the drag value decreases after x/L =1, when compared to the isolated model's drag coefficient their value remains high till an inter vehicle spacing of x/L = 3 after which a change over takes place and the drag value starts decreasing below the isolated model's drag coefficient.

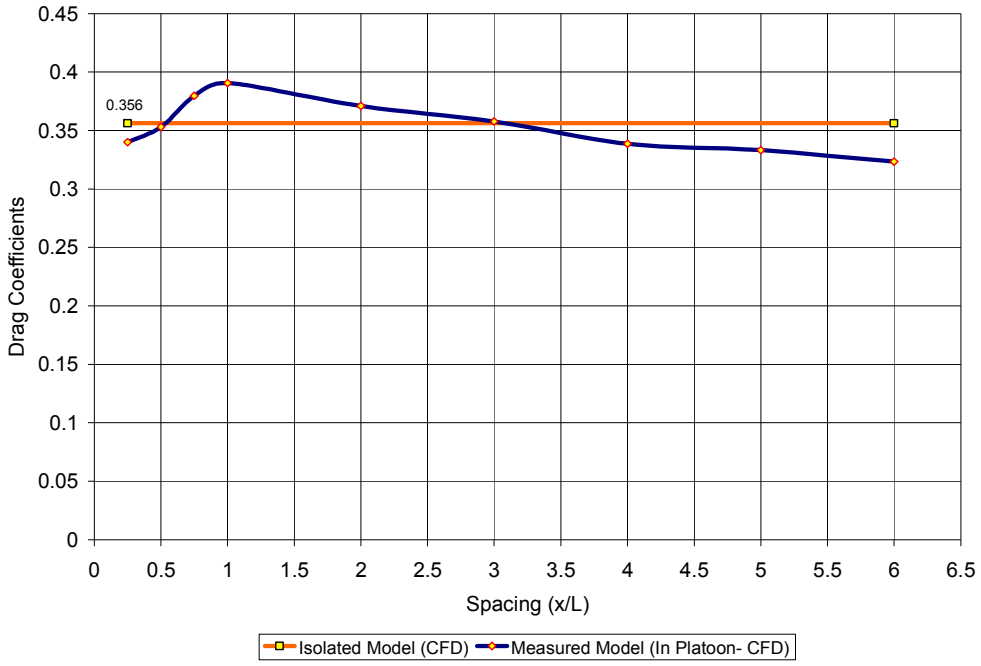

Figure 83. *Effect of vehicle spacing on C_D of measure model with 35˚ rear slant angle*

The 40˚ rear slant configuration shown in figure 84, exhibits a more similar trend to the 35˚ configuration, as both of them comes under the separated low drag regime.

At very close inter-vehicle spacing gaps of $0.25<x/L<0.75$ the drag coefficient is highly dependent upon spacing. The drag coefficient drops from 0.340 at x/L = 0.25 to 0.334 at x/L = 0.5, a trend observed in the attached low drag regime (for 0˚ and 5˚ rear slant configurations). The drag coefficient increases beyond the isolated model's drag coefficient (0.353) to 0.374 and 0.389 at x/L = 0.75 and 1 respectively. From x/L = 1 the trend is more similar to the 35˚ rear slant configuration i.e. a decreasing trend, except for the fact that the drag coefficients remains higher till an inter-vehicle spacing of x/L = 3.5, after which the drag value starts decreasing below the isolated model's drag coefficient. Hence the 40˚ configuration exhibits a mixed trend found in the attached and separated low drag regimes.

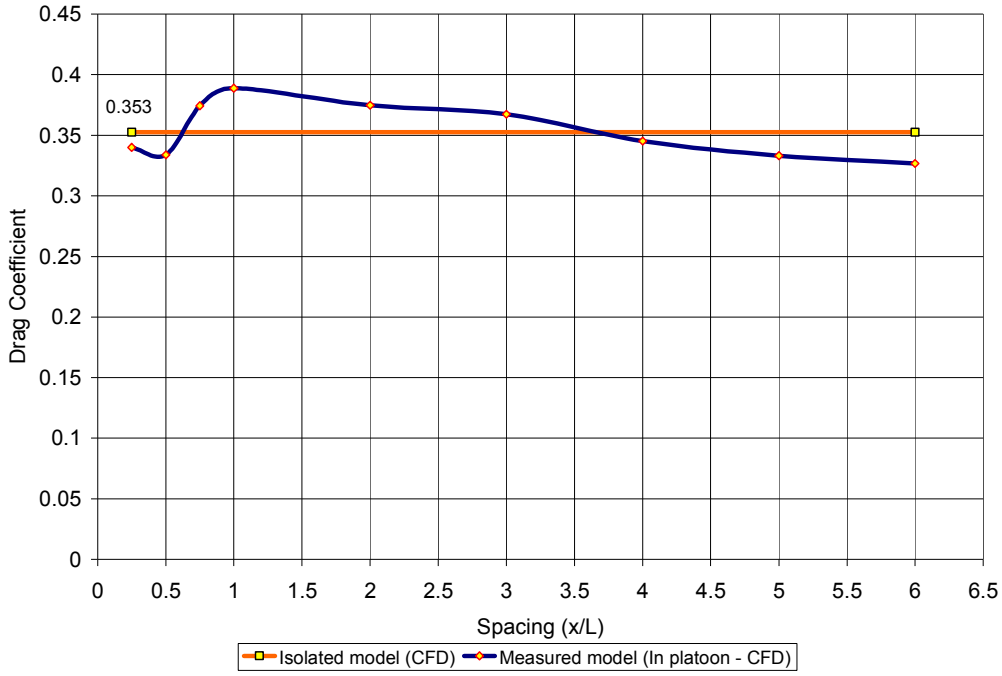

Figure 84. *Effect of vehicle spacing on CD of measure model with 40˚ rear slant angle*

4.2.2.3.1.1 Percentage of Drag Savings at Critical Gaps

Three critical gaps were identified where drag coefficient measured on the measured model in a six model platoon seem to vary. They are at x/L=0.25, 1 and 6. The percentage of drag savings when compared to the isolated model of respective rear slant angles were concluded from this study from the above vehicle-spacing locations (see figure 85). The critical gaps of x/L = 0.25 is considered for attached low drag regimes since the drag coefficient reaches a minimum and x/L =1 for the other regimes where the drag coefficient reaches a maximum.

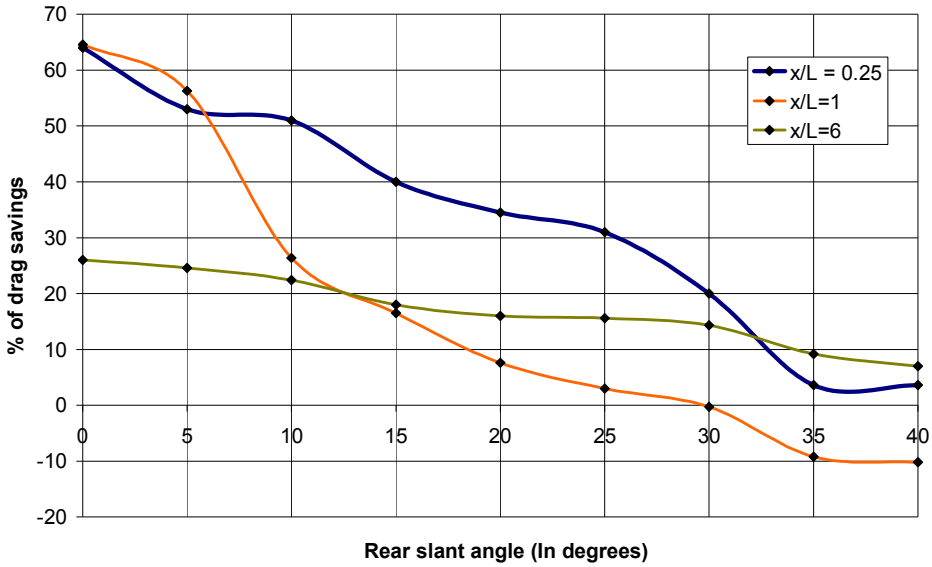

Figure 85. *Percentage of drag savings of measure model for various rear slant angles*

At x/L =1 which is a transition stage where the vortex interaction between the models are high, the drag saving drops down steadily for all the rear slant configurations except for the 0˚ & 5˚ configuration which is due to no significant development of the C-pillar vortices. The drag savings has even become negative (more drag) for models with rear slant angles of separated low drag regime (≥ 30˚).

As the inter-vehicle spacing increases the percentage of drag savings reduces, At x/L =6, the models starts behaving more like a model in isolation and the percentage of drag savings reduces gradually with increase in rear slant angles starting from 0˚.

5. Conclusions and Recommendations

5.1 Conclusions

The main objectives of this research were,

a. Determining the effects of aerodynamic forces and flow structures over isolated 2D and 3D Ahmed car model and also determining the effects of drafting on drag coefficients for the same.
b. Preliminary validation of CFD for selected 3D cases by using the experimental results of Vino and Watkins (2004) for two 100% scale Ahmed models with 30˚ rear slant angle.
c. Determining the effects of inter-vehicle spacing on drag coefficient using two different scales of Ahmed models of 30˚ rear slant configuration.
d. Determining the effects of inter-vehicle spacing and rear slant angles on drag coefficient using Ahmed car models for multiple model platoons.

The work conducted in this research to satisfy these objectives has resulted in the following conclusions:

5.1.1 Two Dimensional (2D) Analysis

1. The 2D analysis for isolated model showed that the wake structure influences the drag coefficient of the model which is dominated by rear slant angles. Significant drag reduction was observed for 25˚ resulting from the reduced recirculation region behind the model.
2. The 2D analysis on drafting with two Ahmed models with 30˚ rear slant angle, showed that the lead model always experiences a lower drag coefficient than the trailing model and the isolated model (2D model's drag coefficient) up to an inter vehicle spacing of (x/L) = 5. This seems unlikely and the reason for this behaviour is thought to be due to the two dimensional behaviour of flow, which is one of the limitations of 2D analysis in performing aerodynamic studies to analyze the effects of drafting.

3. The critical rear slant angle was found to be 25˚ from the 2D analysis, since any increase or decrease of rear slant angle resulted in an increase of drag coefficient.

5.1.2 Three Dimensional (3D) Analysis

5.1.2.1 Isolated Ahmed models

1. The current CFD model (Realizable k-ε turbulence model) overestimated the drag coefficients for all most all the rear slant configurations of the Ahmed model, measured after Ahmed et.al (1984). The error percentage was least with 6% for the critical rear slant angle 30˚ (after Ahmed et.al. (1984)).
2. The over-prediction of drag coefficients were due to the over prediction of base pressure drop by the current CFD model (as shown in section 4.2.2.1.1) and its inability to accurately capture the separation bubble flow characteristics on the model's rear slant.

5.1.2.2 Two 100% scale models

** The study is compared with the experiments conducted on two 100% scale Ahmed models, after Vino and Watkins (2004).*

1. The CFD exhibited an overall error percentage of less than +15% for both the lead and trailing models. The reason for the overestimation of drag coefficients was the code's tendency of over estimating the base pressure drop as shown in section 4.2.2.1.1 Apart from the error; the trends observed on the inter-vehicle spacing effects on drag coefficients were very similar in both CFD and EFD.
2. As observed in experiments, the CFD simulation predicted effectively the decreasing drag coefficient values of the lead model and the increasing drag coefficient of the trailing model at close spacing upto an inter-vehicle spacing of (x/L) = 1.5. The reason for drag reduction on the lead model was due to the increase of base pressures for the lead model by the presence of another model in its wake. Also the increase of drag for the trailing model was due to the significant flow impingement on to its front portion by the flow leaving the

lead model's rear slant, which in turn increased the pressure drag of the trailing model.

3. After a particular spacing between x/L= 1 and x/L=2, the trend changed and both the models maintained constant drag coefficient. This was mainly because the models started to behave like an isolated model, since both the models did not interact strongly.

5.1.2.3 Two different scale models

**Lead Model is 75% scale Ahmed model and Rear model is 100% scale Ahmed model*

**The study is compared with the previous study on two 100% scale Ahmed models*

1. The error percentage between CFD and EFD was +17% for the measured model (lead model), i.e. the CFD over predicted the experimental value. In-spite of the error, identical trends on drag coefficients were observed in both CFD and EFD.
2. The study revealed that the lead model experiences minimal drag coefficient for longer inter-vehicle spacing (compared to the study on two 100% scale models), which was due to the presence of the bigger trailing model in its wake. The trailing model helped to increase the base pressure of the lead model and this effect was observed in both EFD & CFD.
3. The flow leaving the lead model's rear slant impinges on the front part of the trailing model. Because of the smaller frontal area of the lead model, the trailing model experienced direct flow interaction, which kept its drag coefficient higher for longer vehicle spacing (compared to the study on two 100% scale models).

5.1.2.4 Second model in a three model platoon

1. The pre-critical model (25˚ rear slant) clearly exhibited a linear trend of drag increase with an increase in vehicle spacing. The coefficient of drag always remained less than the isolated model's drag coefficient, which was due to greater pressure recovery rate of the model and also the attached flow phenomena over its rear slant surface.

2. The post-critical model (35˚ rear slant) exhibited drag coefficients that could be higher or lower than the isolated model, depending upon spacing.

5.1.2.5 Fifth model in a six model platoon

1. The drag coefficient trends obtained from CFD for the attached the detached low drag configurations showed that even at large inter-vehicle separations (upto x/L=6), the drag coefficients remained well below the isolated case. This might be attributed to the isotropic nature of the k-epsilon turbulence models and its nature of over estimating the base pressure drop.
2. The measured models experienced lower drag than the isolated case at close proximity irrespective of the slant angle. The savings were more for models with rear slant angles of the attached low drag regime. The savings dropped and remained roughly constant for rear slant angles of high drag regime and the savings were found to be negligible for models with rear slant angles of the separated low drag regime.
3. For FGITS, where vehicles are expected to travel in long platoons, the rear slant angles of the attached low drag regime are well suited for platooning for its reduced drag coefficients. Additionally, when a vehicle has to travel in isolation, for example 0˚ rear slant angle, the separations are large and so is the drag penalty.
4. In the case of vehicles with slant angles between the high drag and the separated low drag regimes ($12.5^\circ < \alpha < 40^\circ$), close inter-vehicle spacing is recommended for drag savings.

5.2 Recommendations for further work

Based on the results obtained during this investigation, the author suggests the following recommendations should be considered in future work.

5.2.1 Geometrical Effects

The concept for the Ahmed model geometry was derived from a need to generate some of the essential ‘wake’ flow features of a typical passenger car. However, its shape is considerably different to any existing passenger car. Therefore,

investigating the effects of varying the fore body geometry and analyzing the effects of boat tailing computationally is considered useful. In addition, extending the research to include other forms of simplified passenger cars, such as notchbacks, vans etc would provide some perspective on the generality of conclusions made in this study.

5.2.2 Combination of Rear Slant Angles

Since in the real case scenario combinations of vehicles of various slant angles and sizes are expected to travel in platoons, an analysis can be performed by having various rear slant configuration of Ahmed models of various scales and changing their inter-vehicle spacing accordingly using CFD to understand the wake effects of different rear slant configuration on models in the platoon. Additionally experiments can be conducted for proper validation of the turbulence model and estimate the ability of CFD to replicate this complex combination of vehicle wakes.

5.2.3 Turbulence Model

The turbulence model plays a very important role regarding the final output. For the current study the Realizable k-ε turbulence model is used. The reason for using this turbulence model is that it is reliable in predicting flow structures, mainly the flow separations. There are other turbulence models such as the Reynolds Stress turbulence model and the Large Eddy Simulations (LES). The reason for not using these turbulence models to analyze the effects of drafting is because of the combination of a large test matrix and the required computer resource and time. Therefore, investigating the effects on aerodynamic coefficients of models in drafting arrangement, using these turbulence models can be a useful study provided adequate computer resources are available.

5.2.4 Moving Ground Simulation

In the real case situation, there is a relative velocity that exists between the vehicle and the ground. A study can be performed to analyze the effects of moving ground on the aerodynamic coefficients of vehicles. This can be carried out for isolated Ahmed models and up to several models in tandem. Since a moving ground plane system in a wind tunnel is very expensive, this process can be performed using CFD and comparison plots on aerodynamic coefficients of vehicles can be made with and without moving ground effects at a lower running cost.

6. Appendix - A

JR-3 Force Balance Specifications

JR3 Sensor Model: 160M50A-I100 200N31.5S
Material : Aluminium
Nominal Diameter: 160 mm
Nominal Height: 50mm
Nominal Weight: 20 NM

Figure 86. *"JR-3" 6 components force balance*

7. Appendix - B

CFD Study on Pickup Trucks (Utilities)

As an additional study, the effects of flow structures over pickup trucks are studied for various configurations. This study is carried on only using CFD and is mainly performed to check the effectiveness of the current CFD model in replicating complicated flow structures past more realistic vehicle geometries. The results of this study are compared with previous work done by Sandeep Solvani et.al (2003) and Kevin Cooper (2003), with more emphasis on the flow structures.

7.1 Test Model

The model is a 25% scaled model of Ford Falcon EXT 2003 model. The domain information for the current study is indicated in chapter 2 *(CFD Information)*. The model is considered to be a bluff model that just produces the basic flow structures of a pick up truck. Information on side rear view mirrors, bull bars, engine components and under body information is not included. The test velocity is 40 m/s with a model length based Reynold's number of 3.3×10^6. The model dimensions are given in figure 87.

Model Information

Length (L) = 1.2 m
Height (H) = 0.1L
Width (W) = 0.36L
Ground Clearance (h) = 0.050L

Figure 87. *Pickup truck model information*

7.2 Effects of Different Configurations on Drag Coefficient

The effects of different configurations of Ute's on drag coefficients are analyzed. The different cases that are performed to analyze theses effects are mentioned below,

1. Pickup trucks with sharp corners closed rear tub (i.e. with tonneau covers)
2. Pickup trucks with rounded corners closed rear tub (i.e. with tonneau covers)
3. Pickup trucks with rounded corners opened rear tub (i.e. no tonneau covers)

The influences of all the corresponding configurations that are mentioned above on drag coefficients are shown below in figure 88.

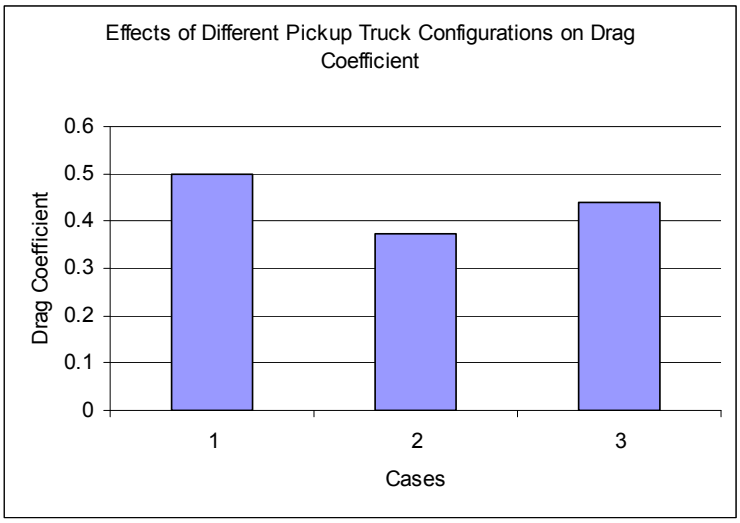

Figure 88. *Effects of coefficient of drag for different pickup truck configurations*

7.2.1 Pickup Truck with Sharp Corners

Initially for preliminary study, the pickup truck with sharp corners is studied, to analyse the effects of flow structures on drag coefficient. This case is performed having the rear tub closed.

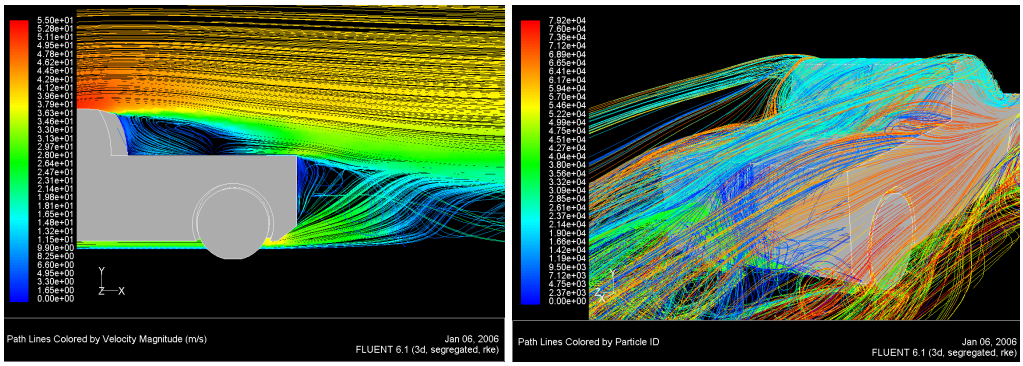

Figure 89. *Recirculation regions and vortices generated by sharp cornered pickup truck*

The presence of sharp edges created major flow separations at the trailing edges of the cab and the tub. Thus, the pressure drop between the cab - tub region and behind the tail gate door region is increased which can be seen by the recirculation regions as shown in figure 89. Also seen are the vortices separating from the A-pillar region along with vortices arising from the rear diffuser, wheels and wheel housings.

7.2.2 Pickup Truck with Rounded Corners

All the sharp edges are rounded and the effects on drag coefficient is analysed. The drag coefficient dropped from 0.5 of sharp cornered to 0.38 which can be seen in figure 88.

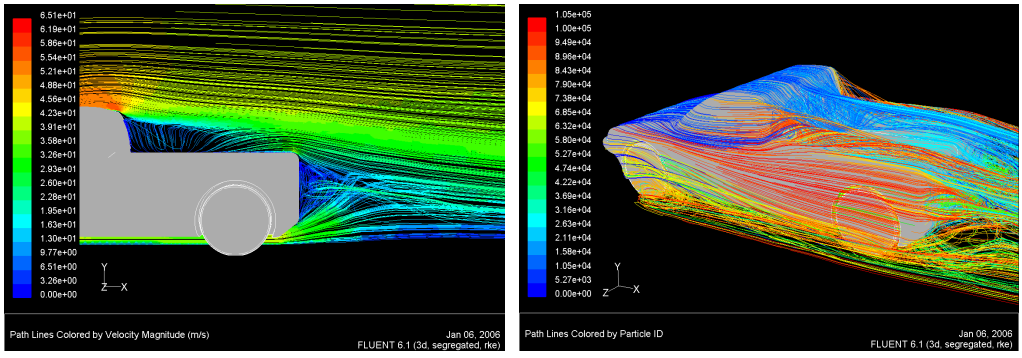

Figure 90. *Recirculation regions and vortices generated by round cornered pickup truck*

The sharp separations seen in the figure 89 are more streamlined here and pressure drop is comparatively reduced, hence the reduction of drag coefficients. The

separation region above the tub and behind the tail gate along with vortex generation behind the model is shown as path lines in figure 90.

7.2.3 Pickup Truck with Rounded Corners and Opened Tub

The effects on drag coefficient is analysed by extending the previous case by making a slight alteration. The rear tub which was closed in the previous case is left opened for the current case. The slight modification caused an immediate increase of drag coefficient from 0.38 to 0.44 which can be seen in figure 88. The main reason was the formation of the large recirculation region behind the cab. The change of flow structures can be clearly seen in the sectioned view which is made along the symmetry plane as shown below in the figure 91. The pressure drop was comparatively high at the cab–tub region, since the corners are rounded the flow was more attached and smooth, hence the drag coefficient remained lower than that observed in sharp cornered model with closed rear tub.

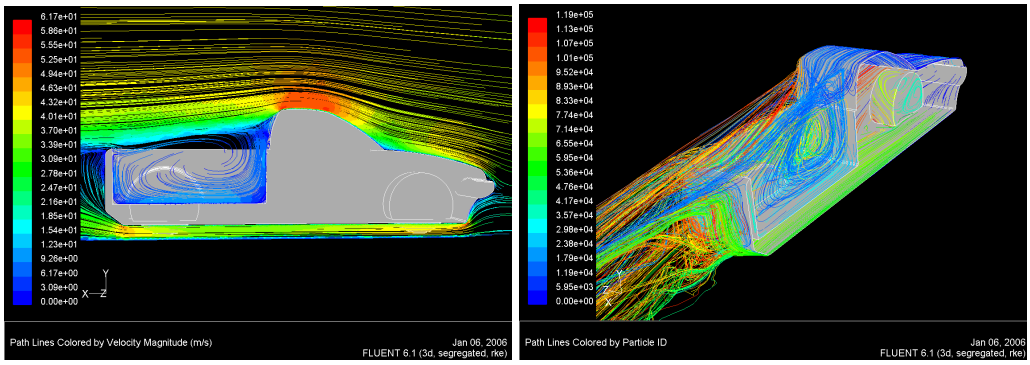

Figure 91. *Recirculation region of open tub configuration of pickup truck*

7.3 Effects of Rear Tub Height on Drag Coefficients

The rear tub of the pickup truck above which a huge recirculation region is created, plays a very important role regarding the effects on the drag coefficients. In order to analyse these effects, the rear tub height is changed considering the rear tub

to be in a closed condition. This study is performed mainly to analyse the effects on the recirculation region and the drag coefficients. The different configurations studied are shown below in figure 92.

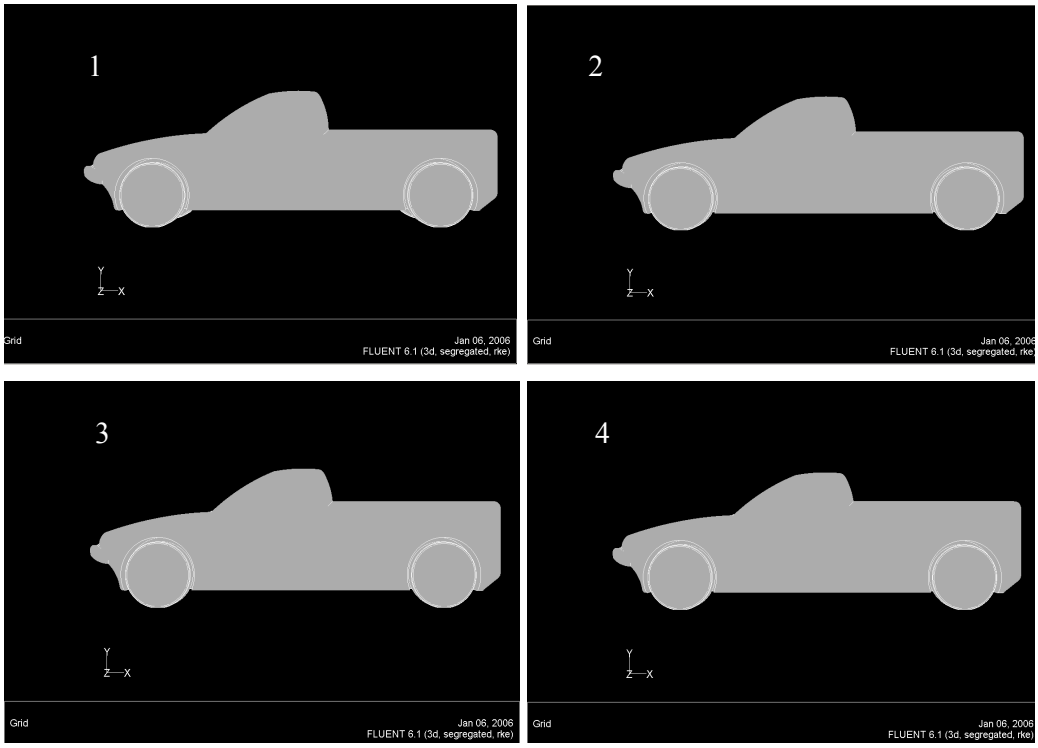

Figure 92. *Different tub height configurations*

The cases that are performed with respect to the configurations shown above to analyse the effects of the rear tub height on drag coefficients are mentioned below,

1. Standard tub height + 0.05 L
2. Standard tub height + 0.1 L
3. Standard tub height + 0.15 L
4. Standard tub height + 0.2 L

The tub height (h) was varied with respect to the length of the pickup truck (L), which is 1.2 m. The maximum tub height was approximately the height which was considered as a safe viewing height for the driver to view the objects behind through the internally positioned rear view mirror. The effects of rear tub height on

the recirculation zone above the tub and behind the tail gate door are shown as velocity path lines measured on the symmetry plane as shown in the figure 93.

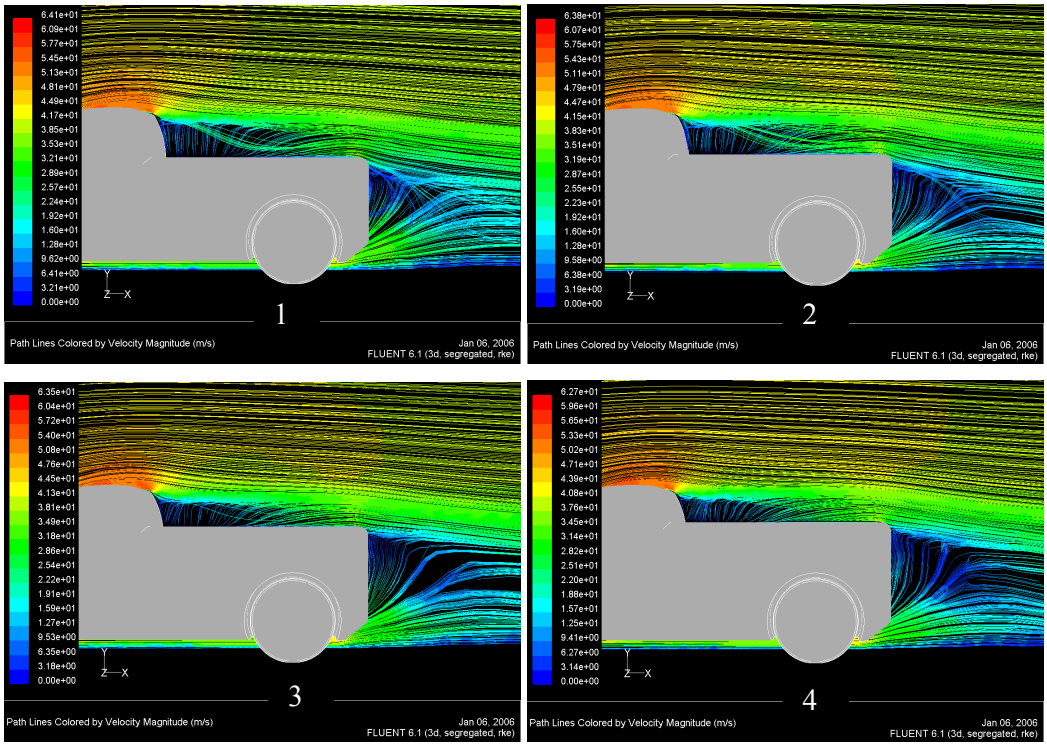

Figure 93. *Effects of tub height on recirculation zones*

The results from the figure 94 clearly reveal that the drag coefficient of a pickup truck can be reduced when the recirculation zone between the cab-tub interface is reduced which in-turn is achieved by increasing the tub height. The effects of rear tub height on drag coefficients are shown below in figure 94.

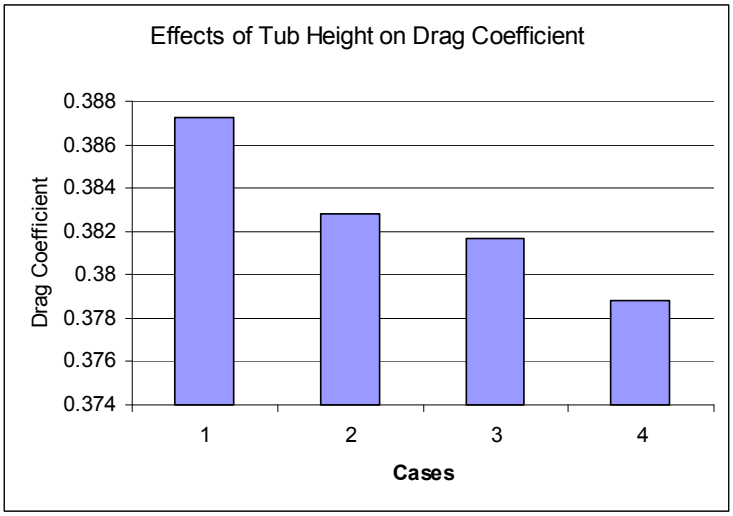

Figure 94. *Effects of tub height on drag coefficients of pick up truck*

The flow structures are identical to the experiments even though a slightly different model is used in the experiments, the vortices and the recirculation region for the open tub configuration resemble to that observed in the literatures (Lokhande et.al, 2003).

From all the above cases discussed, the vortices induced by the wheels and housings are more and they definitely hold a major part on influencing the vehicle's drag coefficient. Hence as a further recommendation, a study can be performed on wheel housings to analyse their contribution to drag and measures for minimising them for achieving better overall performance.

8. Appendix - C

List of Publications

1. Rajamani, G.K, Mavuri, S, Pagliarella, R.M., Tu, J and Watkins, S., "Effect of Flow Structures and Vehicle performance with Spacing Two Different Scales of Ahmed models – A CFD and EFD comparison", Paper submitted for 7th Biennial Engineering Mathematics and Applications Conference, Melbourne, 25-28 September 2005, for the conference proceeding within ANZIAM journal.
2. Rajamani, G.K., Watkins, S., Pagliarella, R.M and Tu, J., "Effect of vehicle spacing, ground clearance on flow structures and drag coefficients having two different scales of Ahmed car models in tandem- A CFD and EFD comparison", Abstract accepted for FISITA 2006, World Automotive Congress, Yokohama, 22 – 27 October 2006.

9. References

Abdel Azim, A.F., "An Experimental Study of Aerodynamic Interference Between Road Vehicles", SAE Paper 940422, 1994.

Abdel Azim, A.F. and Abdel Gawad, A.F., "A Flow Visualisation Study of the Aerodynamic Interference between Passenger Cars", SAE Paper 2000-01-0355, 2000.

Ahmed, S.R., "Influence of Base Slant on the Wake Structure and Drag of Road Vehicles", Transactions of the ASME, Journal of fluids engineering, Vol. 105, pp 429-434, 1984.

Ahmed, S.R., Ramm, G. and Faltin, G., "Some Salient Features of the Time-Averaged Ground Vehicle Wake", SAE Paper 840300, 1984.

Al-Garni, A., Bernal, L. and Khanlighi, B., "Experimental Investigation of the Flow Around a Generic SUV", SAE 2004-01-0228, 2004.

Barnard, R.H., "Aerodynamics of Road Vehicles", Fourth Edition, Society of Automotive Engineers, Warrendale Pa, 1998.

Barth, T. J. and Jespersen, D., "The Design and Application of Upwind Schemes on Unstructured Meshes", Technical Report AIAA-89-0366, AIAA 27th Aerospace Sciences Meeting, Reno, Nevada1989.

Choudhury, D., "Introduction to the Renormalization Group Method and Turbulence Modeling", Fluent Inc. Technical Memorandum TM-107, 1993.

Cogotti, A., "Generation of a Controlled Level of Turbulence in the Pininfarina Wind Tunnel for the Measurement of Unsteady Aerodynamics and Aaero-acoustics", SAE Paper 2003-01- 0430, 2003.

FLUENT Inc., “FLUENT 6.0 User’s Guide”, 2001.

Francis, T.M. and Sung-Eun, K., “Advances in External-aero Simulation of Ground Vehicles using the Steady RANS Equations”, SAE Paper 2000-01-0484, 2000.

Garry, K. P., Wallis, S. B., Cooper, K. R., Fediw, A. and Wilsden, D. J, “The Effect of Aerodynamic Drag of the Longitudinal Position of a Road Vehicle in a Wind Tunnel Test Section”, SAE 940414, 1994.

Gillieron, P. and Chometon, F., “Modelling of Stationary Three-Dimensional Separated Air Flows Around an Ahmed Reference Model”. In ESAIM proc., volume 7, pages 173-182, 1999.

Gotz, K.G., 1983. “Bewegungssehen and FlugsteuerungŽ.bei der Fliege Drosophila”. In: Nachtigall, W. Ed. ,BIONA report 2. Fischer Stuttgart, pp. 21-34.

Hall, R., Thakker, V., Horan, T., Glazer, J., Hoene, C., “Automated Highway System Field Operational Tests for the State of California: Potential Sites, Configurations and Characteristics”, California PATH Research Report UCB-ITS-PRR-97-45, 1997

Hinterberger, Garcia-Villalba, M. and Rodi, W., “Large Eddy Simulation of flow around the Ahmed body”. In “Lecture Notes in Applied and Computational Mechanics / The Aerodynamics of Heavy Vehicles: Trucks, Buses, and Trains”, R. McCallen, F. Browand, J. Ross (Eds.), Springer Verlag, ISBN: 3-540-22088-7, 2004.

Hoerner, S.F., “Fluid-Dynamic Drag”, 1965.

Horowitz, R., “Automated Vehicle and Highway Systems”,1996
Available at :
http://canaima.me.berkeley.edu/~horowitz/research/path/node1.html#SECTION00010000000000000000

Houghton, E.L. and Carpenter, P.W., "Aerodynamics for Engineering Students", Fourth ed., Edward Arnold, London, 1993.

Hucho, W.H., Janssen, L. J. and Schwarz, G., "The wind tunnel's ground plane boundary layer – Its interference with the flow underneath cars", SAE 750066, 1975.

Hucho, W.H., "Road Vehicle Aerodynamic Design", An Introduction, Addison Wesley Longmann Limited, Edinburgh, Harlow, 1996.

Hucho, W.H., "Aerodynamics of Road Vehicles", Fourth Edition, Published by SAE Int. Warrendale Pa, 1998.

Johnson, S.A., Hourigan, K. and Thompson, M.C., "Effect of Aspect ratio on the Wake Structures of Simplified Automotive Geometries", FLAIR, Department of Mechanical Engineering, Monash University, Australia, 2004.

Kapadia S., Roy S. and Wurtzler K., "Detached Eddy Simulation over a Reference Ahmed Car Model", AIAA paper no. 2003-0857, 2003.

Cooper, K.R., "Pickup Truck Aerodynamics – Keep Your Tailgate Up", SAE Paper 2004-01-1146, 2004.

Krajnovic, S. and Davidson, L., "Large Eddy Simulation of the Flow Around a Simplified Car Model", SAE Paper 2004-01-0227, 2004.

Launder B.E., Spalding D.B., "The Numerical Computation of Turbulent Flows", Computer Methods in Applied Mechanics and Engineering, Vol. 3, pp. 269-289, 1974.

Le Good, G. and Garry, K. P., "On the use of Reference Models in Automotive Aerodynamics", SAE Paper 2004-01-1308, 2004.

Lienhart,H., Stoots,C., and Becker,S., “Flow and Turbulence Structures in the Wake of a Simplified Car Model (Ahmed Model)”, DGLR Fach Symp. der AG STAB, Stuttgart University, 15-17 Nov, 2000.

Lienhart, H. and Becker, S., “Flow and Turbulence Structure in the Wake of a Simplified Car Model”, SAE Paper 2003-01-0656, 2003.

Lokhande B., Sovani S., and Khalighi B., “Transient Simulation of the Flow Field Around a Generic Pickup Truck”, SAE paper 2003-01-1313, 2003.

Morel, T., “Aerodynamic drag of bluff body shape characteristics of hatch back cars”, SAE Paper 780267, 1978.

Nouzawa, T, Haruna, S, Hiasa, K, Nakamura, T. and Sato, H, “Analysis of Wake Pattern for Reducing Aerodynamic Drag of Notchback Model”, SAE Paper 900318, 1990.

Nouzawa, T., Hiasa, K., Yoshimoto, M. and Haruna, S., “Influence of Geometry of Rear Part on the Aerodynamic Drag and Wake Structure of a Vehicle”, Mazda Motor Corp, Technical Report, 1992.

Pagliarella, R. M., Watkins, S., Vino, G., “A Preliminary Study in the Ahmed Body Far Wake: Bridging the Gap to FGITS”, Vehicle Aerodynamics Group, School of Mechanical, Manufacturing and Aerospace Engineering, RMIT University, Melbourne, Australia, Presented at 10th EAEC European Automotive Congress, Belgrade, Serbia, 2005.

Romberg, G. H. 1971, Chianese, F. and Lajoie, R. G., “Aerodynamics of Race Cars in Drafting and Passing Situations”, SAE Paper 710213, 1971.

Schlicting H., “Boundary Layer Theory”, McGraw Hill Book Company, 1960.

Shih T.H., Liou W.W., Habbir A., and Zhu J., "A New *k*- ε Eddy-Viscosity Model for High Reynolds Number Turbulent Flows - Model Development and Validation", Computers Fluids, 24(3): 227-238, 1995.

Sims-Williams, D.B. and Dominy, R.G., "Experimental Investigation into Unsteadiness and Instability in Passenger car Aerodynamics", SAE Paper 980391, 1998.

Sims-Williams, D. B., "Self-Excited Aerodynamic Unsteadiness Associated with Passenger Cars, PhD Thesis", University of Durham, 2001.

Sims-Williams, D.B., Dominy, R.G. and Howell, J.P., "An Investigation into Large Scale Unsteady Structures in the Wake of Real and Idealized Hatchback Car Models", SAE Paper 2001-01-1041, 2001.

Sims-Williams, D.B. and Duncan, B.D., "The Ahmed Model Unsteady Wake: Experimental and Computational Analyses", SAE Paper 2002-01-1315,2002.

Spohn, A. and Gillieron, P., "Flow Separations Generated by a Simplified Geometry of an Automotive Vehicle", IUTAM Symposium, 2002.

Strachan R.K., Knowles K., and Lawson N.J., "CFD and Experimental Study of an Ahmed Reference Model", SAE Paper 2004-01-0442, 2004.

Tsuei, L. and Savas, O., "Transient Aerodynamics of Vehicle Platoons during In-line Oscillations", Journal of Wind Engineering and Industrial Aerodynamics, Vol. 89, pp. 1085-1111, 2001.

Vino, G., "An Experimental Investigation into Time-Averaged and Unsteady Aerodynamics of road Vehicles in Isolation and in Convoys", RMIT University, 2005.

Vino, G., Watkins, S., Mousley, P., Watmuff, J., Prasad, S., "The Unsteady Near-Wake of a Simplified Passenger Car", 15th Australasian Fluid Mechanics Conference, Sydney, 2004.

Watkins, S. and Vino, G., "On Vehicle Spacing and its Effect on Drag and Lift", Proceedings, Fifth International Colloquium of Bluff Body Aerodynamics & Applications (BBAA5), Ottawa, Canada, July 2004.

Wang, Q., Barman, P.W. and Harvey, J.K., "A Study of Instantaneous Flow Structure Behind a Car by Particle Image Velocimetry", Proceeding of IMechE Conference on Opticak Methods and Data Processing in Heat and Fluid Flow, 18-19 April 1996, City University, London, 1996, pp. 179-188, 1996.

Yunlong L., Alfred M., "Numerical Modeling of Airflow Over the Ahmed Body", Proceedings of CFD2003, Canada, V2,P507-512,2003.

Zabat, M., Frascaroli, S., and Browand, F.K., "Drag Measurements on 2,3 and 4 Car Platoons", SAE Paper 940421, 1994.

Zabat, M., Stabile, N., Frascaroli, S. and Browand, F., "The Aerodynamic Performance of Vehicle Platoons: Final Report", California PATH, 1995.